Eulerian-Eulerian Modeling of Fluidized Beds

by

Santhip Krishnan Kanholy

Dissertation submitted to the faculty of Virginia Polytechnic Institute and State University in partial fulfillment of the requirements for the degree of

Doctor of Philosophy

in

Mechanical Engineering

Francine Battaglia, Chair

Foster Agblevor

Srinath Ekkad

Brian Lattimer

Danesh K Tafti

September 24, 2014

Blacksburg, Virginia

Keywords: Computational Fluid Dynamics, Two-Phase Flow, Eulerian-Eulerian modeling, Fluidized Bed, Distributor plate Modeling, Biomass

Eulerian-Eulerian Modeling of Fluidized Beds

Santhip Krishnan Kanholy

Abstract

Fluidized bed reactor technology has been widely adopted within the industry as vital component for numerous manufacturing, power generation and gasification processes due to its enhanced mixing characteristics. Computational modeling of fluidized bed hydrodynamics is a significant challenge that has to be tackled for increasing predictive accuracy.

The distributor plate of a fluidized bed is typically modeled using a uniform inlet condition, when in reality the inlet is non-uniform inlet. The regions of bed mass that do not fluidize because of the non-uniform inlet conditions form deadzones and remain static between the jets. A new model based on the mass that contributes to the pressure drop is proposed to model a fluidized bed, and has been investigated for a cylindrical reactor for glass beads, ceramic single solids particles, and glass-ceramic, and ceramic-ceramic binary mixtures. The adjusted mass model was shown to accurately predict fluidization characteristics such as pressure drop and minimum fluidization velocity.

The effectiveness of the adjusted mass model was further illustrated by applying it to fluidized beds containing coal, switchgrass, poplar wood, and cornstover biomass particles and coal-biomass binary mixtures. The adjusted mass model was further analyzed for bed expansion heights of different mixtures, and for solids distribution by analyzing the solids volume fraction. The effect of increasing the percent biomass in the mixture was also investigated.

To further model the non-uniform inlet condition, two different distributor configurations with 5 and 9 jets was considered for a quasi-2D bed, and simulations were performed in both 2D and 3D. Fluidization characteristics and mixing of the bed were analyzed for the simulation. Furthermore, the deadzones formed due to multiple jet configurations of the distributor are quantified and their distributions over the plate were analyzed.

Acknowledgments

I would like to take this opportunity to thank the people who have made my research and dissertation possible directly or indirectly.

First and foremost, I would like to acknowledge my advisor Dr. Francine Battaglia for giving me the opportunity to be her doctoral student. She is an amazing mentor who taught me how to think and work efficiently, to present my research professionally in oral and written fashion. I wouldn't have been able to complete my research if it wasn't for her clear guidance and support. She ensured financial support when I needed it the most, so that I could succeed as a doctoral student. Her integrity in research, her compassion, and her leadership qualities has inspired me during my years with her and continues to inspire me in my life. She is a wonderful role model with the qualities I hope to emulate in my life. The debt of gratitude I have for her is beyond words.

I would also like to thank my committee members, Dr. Foster Agblevor, Dr. Brian Lattimer, Dr. Srinath Ekkad, and Dr. Danesh Tafti, for their contributions, recommendations, and for their willingness to be a member of my committee.

I would like to thank the agencies that funded my work. I am grateful to Institute of Critical Technology and Science (ICTAS) for funding the research on quasi-2d fluidized bed. I would like to thank the Department of Energy (grant DE-FE-0005476) for their financial support with the Coal-biomass hydrodynamics research. I would also like to thank the Graduate School for providing me the financial support for my final semester, specifically Dean Karen DePauw, Ms. Monika Gibson, and Mr. Jeremy Sippel. I would also like to thank the technical support provided by the Advanced Research Computing (ARC) at Virginia Tech. Thank you to Ms. Jillian Chodak, Mr. Gaurav Agarwal of Virginia Tech, and Mr. Che Guevara Nyendu of Dr. Agblevor's group for providing the experimental data used in this research. Also, thank you to Surya Deb for the

valuable discussions on different aspects of this research.

Finally, I would like to acknowledge my friends and family. I would also like to thank for current and former members of the Computational Research Energy Systems Transport Lab (CREST) for the discussions and support I have had throughout my degree. I would also like to thank Dr. Ed Hampton, Dr. Laura Clark, Ms. Mikhelle Taylor and Mr. Lee Worley for their kindness and encouragement. Thank you to Dr. Jose Prakash, my undergraduate advisor who motivated me to pursue a PhD. I would also like to acknowledge Ms. Ganga Karmokar, who has been an important mentor in guiding me towards maturity in life. I would also like to thank my friends whom I have met during my stay here at Virginia Tech, who helped me have a life outside the lab. Thank you to my sister for her moral support. I would also like to thank my parents, who sacrificed a lot to ensure my education, for their love and compassion in raising me, and for making me believe in myself to pursue my own dreams.

Table of Contents

List of Figures

List of Tables

Nomenclature

A	Cross-sectional area of the bed
D	strain tensor
d_p	Particle diameter
dwf	Downwind factor
e	Coefficient of restitution
F	Drag force
g	Gravitational acceleration
h	Bed height
$\mathbf{I}$	Interphase momentum transfer
k	Turbulent kinetic energy
M_w	Molecular gas weight
m	Initial bed mass
P	Pressure
Q	Volumetric flow rate
$\mathbf{q}$	Diffusive flux of granular energy
R	Universal gas constant
S	Mean strain rate tensor
T	Temperature
t	Time
U_{mf}	Fluidization velocity
$\mathbf{u}$	Velocity vector
V	Volume occupied by the bed
X	Mass fraction
X	Horizontal width
Y	Vertical height
Z	Height above the distributor

Greek Letters

ϵ	Volume fraction, turbulent dissipation
ξ	Convection weighting factor

Φ	Scalar at cell faces
ϕ	Transfer of granular energy between phases
φ	Blending function
γ	Granular energy dissipation due to inelastic collisions
μ	Dynamic Viscosity
Π	Turbulence interaction term
κ	Granular conductivity
θ	Granular temperature
ρ	Density
σ	Stress tensor
τ	Reynold's stress tensor
ψ	Particle sphericity
ω	Under relaxation factor

Superscripts/Subscripts

*	critical solids pressure
b	bulk
exp	experimental
E	east face
f	friction
g	gas phase
i	individual solid phase component
l	*l*th solid phase
m	mth solid phase
mf	minimum fluidization
mix	mixture
p	particle
pl	plastic regime
s	solid phase
t	turbulent parameters
total	corresponds to the entire bed

v	viscous regime
0	initial condition

Chapter 1. Introduction

1.1. Background

Fluidization is the process in which granular material is converted from a static solid state to a dynamic fluid state by passing a gas at sufficient velocity through the granular material [1]. The velocity at which the fluidization process occurs is called the minimum fluidization velocity [2]. The size, shape and location of the voids formed between the particles constantly change within the fluidized bed. Further increasing the gas velocity results in different fluidization regimes such as bubbling, slugging, turbulent and fast fluidization. The bubbling regime exhibits dynamic movement of particles, and small bubbles coalescence. In the slugging flow regime, the bubbles grow as large as the bed diameter and breakup in the turbulent regime, where bubbles rapidly coalesce and split. In the fast fluidization regime, significant particle entrainment occurs, and the upper surface of the bed is not clearly defined. Depending upon the process design, different fluidization regimes are employed accordingly.

Fluidized beds are widely used in many modern technologies for efficient implementation of various physical and chemical processes. The nearly isothermal conditions due to the rapid mixing of particles, high heat and mass transfer rates, resistance to sudden changes in operating conditions, etc., are different advantages for using fluidized beds. Gasification is an important process for converting fuels into useful gaseous products. The technology has a variety of applications from waste treatment, power production, nuclear and chemical industries. There is immense value in improving the capabilities of gasification technology and both experiments and computational modeling are used to better understand the physics of fluidization in industrial scale gasifiers.

Computational fluid dynamics (CFD) can be a powerful design and development tool for modeling industrial gasifiers and is more cost effective rather than building pilot scale facilities. CFD can model detailed aspects of the phenomena encountered in fluidized beds and capture the complex behavior of the multiphase reacting flows. Two-fluid model (TFM) and discrete particle model (DPM) approaches have been used in CFD studies of gasification problems. For TFM, both solid and gas phases are treated as interpenetrating continua, with each phase having the corresponding governing equations for continuity, momentum and energy. Interactions between the two phases are accounted through the drag model, and closures obtained using kinetic theory of granular flows (KTGF) or experimental correlations. The simulation time required for the DPM

approach is very long compared to TFM approach since the individual particles are tracked and modeled using Newton's laws of motion. TFM is more commonly used over DPM in designing industrial gasifiers because of the significantly reduced computational expense involved.

Typically experiments are used to design fluidized beds using lab-scale reactors to validate the models developed using CFD. Different boundary conditions are used to represent the conditions of the reactors being modeled. The efficiency of the distributor plate being used in the fluidized bed is very important to ensure a full fluidization of a media. Thus it is necessary to capture the effects of the distributor plate accurately in the computational models. CFD can be used in assisting the design of reactors through parametric studies, and understanding of the flow features.

An application of fluidized bed technology is coal gasification, which has been extensively used to meet the power needs of various industries [3]. The presence of vast coal reserves ensures the availability of the coal for a considerable amount of time in the future. Hence efficient use of coal is required in order to reduce the harmful emissions caused by gasifying coal. Biomass is currently being considered as an attractive alternative fuel for gasification to reduce the pollution and greenhouse gases such as SO_2, NO_X created by coal [4]. Biomass gasification can thus be considered to be a source of clean power thereby reducing CO_2. Biomass can include items such as wheat straw, corn stover, switchgrass, mixed hardwood, pine seed shells, dried grains and even algae [5]. Biomass gasification is often used to produce synthesis gas (i.e., syngas), which has great flexibility in its application, and has great potential in meeting increasing energy needs of the world. Prior to accurately modeling gasification, it is necessary to model the hydrodynamics of biomass particles. However biomass particles are peculiar in shape, with non-uniform density making it difficult to fluidize. Segregation, particle agglomeration, defluidization, etc., are commonly associated problems with biomass.

Coal and biomass blends as fuel for gasification are also being investigated [6]. Using biomass which is a carbon neutral fuel along with coal can reduce pollutant emissions. There are few published studies that focus exclusively on hydrodynamics, since the majority of the literature is in the area of combustion and gasification. Modeling the hydrodynamics of coal-biomass mixtures are a challenge in itself, considering fluidization problems associated with biomass. There are different uncertainties and challenges that have to be faced, especially in determining the optimum percentages of various blends of coal and biomass, which are yet to be fully investigated and understood.

1.2. Research Objectives and Approaches

The goal of this research is to computationally model fluidized beds using the open source CFD software Multiphase Flow with Interphase eXchanges (MFIX) [7]. Whenever possible, simulation predictions will be validated with experimental measurements. Modeling efforts will also be directed towards improving the reactor design by considering the distributor plate, which can create non-uniform inlet conditions. The distributor plate is the bottom part of the fluidized bed through which pressurized gases pass through small holes and flow into the reactor and through the granular media. Some amount of solid particulates remains trapped between the inlet jets formed by the holes, and the regions are called deadzones and do not contribute to the fluidization. Typically, when modeling the fluidized bed, the entire mass present in the bed is modeled, which would also include the deadzone mass.

For the first objective of the study, non-uniform conditions will be modeled by making use of the fluidizing mass determined from the experimental pressure drop measurements by adjusting the initial bed mass. The efficacy of the adjusted modeling approach will be demonstrated first for a single solids phase of either glass beads or ceramic particles of different diameter ranges. The modeling approach will then be extended to glass-ceramic binary mixtures of the same average particle diameter and ceramic-ceramic binary mixtures with different particle diameters. The predictions for pressure drop and minimum fluidization velocity will be compared with experimental measurements obtained from Chodak [8].

The second objective of the study involves modeling the distributor plate by studying the hydrodynamics of different distributor plate configurations for a quasi-2D bed [9]. The hydrodynamics of multiple jet interactions will be analyzed for a 9-holed distributor plate and 5-holed distributor, and the effects of grid resolution on the flow field will be investigated for the 9-holed distributor. The fluidization characteristics, solids volume fractions, and solids velocities will be analyzed and compared with experimental observations. Deadzones being formed due to different distributor configurations will also be analyzed.

The third objective of the study is to model coal and biomass gasification with a focus on predicting their corresponding fluidization characteristics. The adjusted mass model developed in the first objective, will be investigated for its efficacy in predicting coal, biomass and coal-biomass mixture fluidizations. Simulation predictions will be used to identify the most optimum mixture ratio, and the corresponding biomass material for the coal-biomass mixture.

1.3. Outline of the Dissertation

In chapter 2, a general survey of literature relevant to Eulerian-Eulerian modeling, quasi-2D bed modeling, and coal-biomass hydrodynamics in a fluidized bed is presented. Chapter 3 presents the hydrodynamics of multi-fluid modeling and the numerical formulation implemented in MFIX. Chapter 4 describes the work related to modeling the non-uniform conditions using the different models for a single solids phase and binary mixture fluidized beds using experimental parameters to determine initial conditions for the model. Chapter 5 presents studies of a quasi-2D fluidized bed with 9-hole and 5-hole distributor inlet configurations. Two-dimensional and three-dimensional simulations are compared with the experimental measurements of pressure drop, solids volume fraction, and solids velocity, along with investigation of deadzone characteristics for the bed. Chapter 6 investigates predictions of fluidization characteristics for coal and coal-biomass blends using the models developed in Chapter 4. Chapter 7 summarizes the main conclusions from the research work in this dissertation. Possible extensions to the dissertation work are discussed.

Chapter 2. Literature Review

2.1. Introduction

Fluidized beds have a very wide range of industrial applications such as fuel production, mineral and powder processing, biochemical, agricultural, and pharmaceutical industries. Rapid mixing of solids and high heat and mass transfer rates are some of the advantages with using fluidized beds [10]. However the hydrodynamics are complicated and make it difficult to maximum the efficiency of the fluidization process. In an effort to support the design and optimization of reactors, computational fluid dynamics (CFD) can be an effective modeling tool to predict the hydrodynamics of fluidized beds. Different modeling approaches have improved the accuracy of CFD predictions, and further improvement in this regard is a necessity for progress in understanding fluidized bed operation.

2.2. Eulerian-Eulerian modeling

There are two main approaches in CFD modeling of gas-solids flows: the Lagrangian-Eulerian model [11,12] and the Eulerian-Eulerian model [13,14]. Studies have also been performed using a hybrid approach which couples both Eulerian-Eulerian and Lagrangian modeling through the interphase momentum transfer terms [15]. In the Lagrangian-Eulerian model, individual particles are tracked by solving the equations of motion with the gas being accounted for within an Eulerian framework. The approach is computationally very expensive for large systems of particles. However, in a fluidized bed upon the state of incipient fluidization, the solids phase behaves like a fluid and can also be computationally treated as such. In Eulerian-Eulerian modeling, both solids and gas phases are treated as interpenetrating continua. An advantage is that the computational time can be reduced. Hence the Eulerian-Eulerian modeling approach for gas-solids fluidized beds is the more widely used CFD model to predict the hydrodynamic behavior.

Different models have been used to improve the Eulerian-Eulerian modeling of bubbling fluidized beds [16]. Esmaili et al. [17] adjusted the drag coefficient correlations for the Di Felice model and performed 3D simulations of a bubbling fluidized bed to determine improvements in hydrodynamic predictions. Pie et al. [18] investigated the effect of the interphase drag coefficient by comparing different drag models for a fluidized bed with a single jet as an inlet and concluded that no single model could give accurate predictions completely. Deza et al. [19] compared two-dimensional and three-dimensional simulations of biomass particles with experimental

measurements of void fraction obtained using X-ray computed tomography and determined that the Gidaspow drag model provided a good approximation for gas-solid interactions. They also found that coefficient of restitution did not affect the predictions as much when compared to sphericity. Hosseini et al. [20] also analyzed the effects of different drag models for a bubbling gas-fluidized bed and concluded that the Gidaspow drag model had better agreement with experiment data. Gavi et al. [21] used the idea of "effective density" based on the solids packing limit of glass beads to use a new density value for biomass materials to improve the hydrodynamic predictions of void fraction profiles and bed-expansion height. They also confirmed the results for coefficient of restitution and sphericity presented by Deza et al. [19].

Binary mixtures have also been modeled using the Eulerian-Eulerian approach. Van Wachem et al. [22] modeled a binary mixture using CFD and predicted similar results for bed expansion height and minimum fluidization velocity to that of experiments. Zhang et al. [23] investigated a jetting fluidized bed with a binary mixture and determined that the effect of the increasing mass fraction of the lighter component in the binary system increased the jet penetration height. Gao et al. [24] studied the mixing/segregation behavior of disparately-sized binary mixtures of small and large particles in a turbulent fluidized bed with both experiments and CFD and found that the segregation efficiency increased with increasing gas velocity. Coroneo et al. [25] investigated the influence of numerical parameters such as temporal and spatial resolutions on predicting bed segregation for binary mixtures using the commercial software Fluent $6.3^{T.M}$ and found that the magnitude of numerical errors depended heavily on the operating conditions such as mixture composition and higher jetsam volume fraction.

2.3. Two-dimensional bed studies

In a fluidized bed the gases enter through the distributor plate at the bottom of the bed to promote mixing between the different phases involved. Typically, distributor plates are modeled as uniform inlet velocity conditions, rather than a series of jets, and are appropriate for modeling reactors where the distributor holes are uniformly placed. However, in cases when the distributor holes are not uniformly distributed, this could lead to inaccurate modeling predictions.

Performance of the gas distributor plate is critical to the efficiency of fluidized beds [26]. Sasic et al. [27] demonstrated that a uniform inlet condition cannot be used for a numerical simulation if pressure fluctuations within the air-supply system strongly affect with the fluidized bed. Paiva et al. [28] investigated the influence of different kinds of distributor plates on the hydrodynamics

of a Geldart B particle for a fluidized bed approaching transition from bubbling to turbulent fluidization and created a simple model to describe voidage characteristics.

Eulerian modeling has become a commonly used way of modeling fluidized beds [29]. Earlier works using Eulerian modeling of fluidized bed were performed by Syamlal et al. [30] and Ding et al. [31]. Boehmer et al. [32] performed Eulerian simulations of bubble formation for a single jet flow in a two-dimensional fluidized bed and compared different models for evaluating granular temperature. Recently, Hernandez-Jimenez et al. [33] performed validation studies for their simulations of a quasi-2D bed with experimental data obtained through particle image velocimetry (PIV) and digital image analysis (DIA). They found that while the bubble diameters predicted by the simulations were close to the experiments, time-averaged solid phase velocity components were an order of magnitude larger than the PIV data. Utikar et al. [34] compared CFD simulations of a rectangular fluidized bed with experimental data obtained using DIA for glass and polypropelene particles with three central jets as its inlets. They found that CFD models were able to capture some aspects of fluidization such as gas volume fractions but were unable to do so with regard to bubble rise velocities.

Hong et al [35] analyzed the influence of jet characteristics, particle properties, fluidizing gas characteristics, and bed height on jet penetration heights for two vertical jets in a quasi-2D fluidized bed using numerical simulations and experiments, and found out that the jet penetration heights increased with increase in superficial gas velocity contrary to most published reports. Hosseini et al [36] investigated numerically circulation flow patterns for different distributor plates and determined that gas velocity and ratio of static bed height to width of the bed are important parameters for predicting circulation flow patterns.

2.4. Coal Biomass hydrodynamics

In lieu of the fact that energy produced by burning coal causes release of harmful CO_2, nitrogen and sulfur emissions, alternative means of reduction in the production of these pollutants have been considered through co-gasification of coal and biomass. A majority of the published literature is focused on gasification of coal and biomass, with little information published on modeling of fluidized bed hydrodynamics with coal and biomass mixtures. Hence there is a strong need to develop multiphase flow models combining experimental findings, conventional models and CFD to guide design and operation of biomass processes [37].

Zhang et al [38] studied hydrodynamics of a fluidized bed containing tobacco waste and coal for a rectangular bed. The authors observed three different fluidization velocities, i.e. initial, minimum and full fluidization velocities for different tobacco stem fractions, and suggested using mass fractions less than 7% of tobacco stem for bubbling fluidized beds. Rao et al [39] investigated minimum fluidization velocities of mixtures of biomass such as rice husks, sawdust, groundnut shell powder and sand and proposed equations for predicting U_{mf} by representing the mixture using effective particle properties could give satisfactory predictions.

Papadakis et al. [40] investigated momentum transport from fluidizing gas and sand to a solid biomass particle for a lab-scale reactor using the Eulerian-Lagrangian model in FLUENT. They determined that the drag force induced by the carrier fluid surrounding the particle was the major parameter that defined particle motion. They also investigated effects of different particles on char entrainment in another study [41], and concluded that smaller particles were efficiently entrained in the reactor. Sharma et al [42] modeled hydrodynamic behavior of biomass-biochar mixture for different operating conditions using FLUENT. The authors found that density of biomass particles had considerable effect on the mixing and segregation with the particle diameter having the least effect. Bai et al [43] investigated mixing and segregation behavior of mixtures of ground walnut shell and glass beads in a fluidized bed, with the biomass being injected through a side port. They found that segregation of biomass was dependent on the gas velocity, with segregation occurring in the lower velocity. Deza et al. [19] studied hydrodynamics of biomass fluidized bed with an Eulerian-Eulerian model using MFIX and compared simulation results with X-ray imaging measurements. The sphericity of the biomass particles were found to influence the biomass hydrodynamics significantly.

2.5. Summary

In this chapter, relevant studies about Eulerian-Eulerian modeling of fluidized beds, quasi-2D beds, and coal-biomass hydrodynamics in a fluidized bed have been reviewed. The reviews guide the research herein to determine the capabilities and limitations of the current CFD models, and to contribute to new understanding and development of models.

Chapter 3. Numerical Formulation

3.1. Governing Equations

The multifluid Eulerian-Eulerian models employed in the code Multiphase Flow with Interphase eXchanges (MFIX) [44] is used in this work. The instantaneous variables are averaged over a region that is larger than the particle spacing but smaller than the flow domain. Volume fractions are introduced to track the fraction each phase occupies in the averaging volume, where ε_g is the gas phase volume fraction (also referred to as the void fraction) and ε_s is the solids phase volume fraction. The solids phase is described with an effective particle diameter d_p and characteristic material properties, and solved using a conservation equation for the solids phase.

The continuity equations for the gas phase and the solids phase, respectively, are:

$$\frac{\partial\left(\varepsilon_g \rho_g\right)}{\partial t} + \nabla \cdot \left(\varepsilon_g \rho_g \mathbf{u}_g\right) = 0 \tag{1}$$

$$\frac{\partial\left(\varepsilon_s \rho_s\right)}{\partial t} + \nabla \cdot \left(\varepsilon_s \rho_s \mathbf{u}_s\right) = 0 \tag{2}$$

where ρ is the density and $\mathbf{u}$ the velocity vector.

The momentum equations for the gas and solids phases have the form:

$$\frac{\partial\left(\varepsilon_g \rho_g \mathbf{u}_g\right)}{\partial t} + \nabla \cdot \left(\varepsilon_g \rho_g \mathbf{u}_g \mathbf{u}_g\right) = -\varepsilon_g \nabla P_g + \nabla \cdot \overline{\overline{\sigma}}_g + \mathbf{I}_g + \varepsilon_g \rho_g \mathbf{g} \tag{3}$$

$$\frac{\partial\left(\varepsilon_s \rho_s \mathbf{u}_s\right)}{\partial t} + \nabla \cdot \left(\varepsilon_s \rho_s \mathbf{u}_s \mathbf{u}_s\right) = -\varepsilon_s \nabla P_g + \nabla \cdot \overline{\overline{\sigma}}_s - \mathbf{I}_g + \varepsilon_s \rho_s \mathbf{g} \tag{4}$$

The expressions on the left side are the net rate of momentum increase and the net rate of momentum transfer by convection. The right side includes contributions for buoyancy caused by the fluid pressure gradient, the stress tensor($\overline{\overline{\sigma}}$), gravity ($\mathbf{g}$), and the interaction forces ($\mathbf{I}_g$) accounting for the momentum transfer between the gas and solids phases. The interaction force in Eqns. (63) and (64) accounts for the gas-solids momentum transfer, which is expressed as the product of the coefficient for the interphase drag force between the gas and solids phases and the slip velocity between the two phases. The work herein has employed the Gidaspow model for the interphase drag force and previous studies by Xie et al. [45] and Deza et al. [19] have shown the validity of using the model.

The granular temperature θ for the solids phase can be related to the granular energy defined as the specific kinetic energy of the random fluctuating component of the particle velocity. The resulting transport equation for the granular temperature is:

$$\frac{3}{2}\left[\frac{\partial\left(\varepsilon_s\rho_s\theta\right)}{\partial t}+\nabla\cdot\left(\varepsilon_s\rho_s\theta\right)\mathbf{u}_s\right]=\nabla\cdot\overline{\overline{\sigma}}_s:\nabla\mathbf{u}_s-\nabla\cdot\mathbf{q}_\theta+\gamma_{slip}-\gamma_\theta+\phi_g \tag{5}$$

where $\mathbf{q}_\theta$ is the diffusive flux of granular energy, γ_{slip} is the production of translational fluctuation kinetic energy due to gas-solids slip, γ_θ is the rate of granular energy dissipation due to inelastic collisions, and ϕ_g is the transfer of granular energy between the gas phase and solids phase.

3.2. Constitutive Relationships

Kinetic theory for granular flow is used to calculate the solid stress tensor and solid-solid interaction forces in the rapid granular flow regime. Two distinct flow regimes exists in granular flow: a viscous or rapidly shearing regime in which collisional or translational momentum transfer causes the stresses to arise, and a plastic or slowly shearing regime in which the Coloumb friction between the solids in close contact is the reason for causing the stress. A blending function is employed to provide a smooth transition between both the regimes.

3.2.1. *Gas-solid equation of state*

It is assumed that the gas-density can be modeled using the ideal gas law:

$$\rho_g=\frac{p_g M_w}{RT_g} \tag{6}$$

where p_g is the gas pressure, M_w is the molecular gas weight, R is the universal gas constant and T_g is the gas temperature.

3.2.2. *Solid phase stress tensor*

The constitutive relationship for the solids phase stress tensor is:

$$\bar{\bar{\sigma}}_{sm}=\begin{cases}-P_{sm}^{pl}\bar{\bar{I}}+\bar{\bar{\tau}}_{sm}^{pl} & for\ \epsilon_g\leq\epsilon_g^*\\ -P_{sm}^{v}\bar{\bar{I}}+\bar{\bar{\tau}}_{sm}^{pl} & for\ \epsilon_g>\epsilon_g^*\end{cases}$$

where P_{sm}, $\bar{\bar{I}}$, $\bar{\bar{\tau}}_{sm}$ and ϵ_g^* are the solid pressure, identity tensor, viscous stress for the m^{th} solid phase, and void fraction at minimum fluidization, respectively. To describe the stress in the granular phase, Abu-Zaid and Ahmadi [46] took into account interstitial fluid effects, where granular pressure and stresses are:

$$P_{sm}^{v} = K_{1m}\epsilon_{sm}^{2}\theta_{m} \tag{7}$$

$$\bar{\bar{\tau}}_{sm}^{v} = 2\mu_{sm}^{v}\bar{\bar{D}}_{sm} + \lambda_{sm}^{v}tr\left(\bar{\bar{D}}_{sm}\right)\bar{\bar{I}} \tag{8}$$

The second coefficient of viscosity (λ_{sm}^{v}), the shear viscosity (μ_{sm}^{v}), and the rate of strain tensor $\left(\bar{\bar{D}}_{sm}\right)$ are given by:

$$\lambda_{sm}^{v} = K_{2m}\epsilon_{sm}\sqrt{\theta_{m}} \tag{9}$$

$$\mu_{sm}^{v} = K_{3m}\epsilon_{sm}\sqrt{\theta_{m}} \tag{10}$$

$$\bar{\bar{D}}_{sm} = \frac{1}{2}[(\nabla\mathbf{u}_{sm}) + (\nabla\mathbf{u}_{sm})^{T}] \tag{11}$$

The coefficients K_{1m} K_{2m} and K_{3m} are functions of the coefficient of restitution (e_{mm}), particle density (ρ_{sm}), particle diameter (d_p), and radial distribution function (g_{0mm}), where:

$$K_{1m} = 2(1 + e_{mm})\rho_{sm}g_{0mm} \tag{12}$$

$$K_{2m} = \frac{4d_p\rho_{sm}(1 + e_{mm})\epsilon_{sm}g_{0mm}}{3\sqrt{\pi}} - \frac{2}{3}K_{3m} \tag{13}$$

$$K_{3m} = \frac{d_p\rho_{sm}}{2}\left[\frac{\sqrt{\pi}}{3(3 - e_{mm})}[1 + 0.4(1 + e_{mm})\epsilon_{sm}g_{0mm}] + \frac{8\epsilon_{sm}g_{0mm}(1 + e_{mm})}{5\sqrt{\pi}}\right] \tag{14}$$

In the plastic regime, an arbitrary function from the frictional flow theory [47] allows compressibility in the solid phase and can be expressed as:

$$P_{sm}^{pl} = \epsilon_{sm}P^{*} \tag{15}$$

An empirical power law is used to express P^{*}

$$P^{*} = A\left(\epsilon_{g}^{*} - \epsilon_{g}\right)^{n} \tag{16}$$

where A = 10^{25} and n = 10. The solid stress tensor for the m^{th} solid phase is calculated using the formulation by Schaeffer [48]:

$$\bar{\bar{\tau}}_{sm}^{pl} = 2\mu_{sm}^{pl}\bar{\bar{D}}_{sm} \tag{17}$$

3.2.3. *Gas phase stress tensor*

The gas phase stress tensor can be described as a function of the gas pressure and the Newtonian viscous stress tensor as:

$$\bar{\bar{\sigma}}_g = -P_g \bar{\bar{I}} + \bar{\bar{\tau}}_g \tag{18}$$

The viscous stress tensor ($\bar{\bar{\tau}}_g$) and the strain rate tensor for the gas phase ($\bar{\bar{D}}_g$) are given by:

$$\bar{\bar{\tau}}_g = 2\epsilon_g \mu_g \bar{\bar{D}}_g + \epsilon_g \lambda_g tr(\bar{\bar{D}}_g)\bar{\bar{I}} \tag{19}$$

$$\bar{\bar{D}}_g = \frac{1}{2}\left[(\nabla \mathbf{u}_g) + (\nabla \mathbf{u}_g)^T\right] \tag{20}$$

3.2.4. *Gas-solids momentum transfer*

The interaction force ($\mathbf{I}_{gm}$), in the momentum Eqns. (3) and (4) accounts for the gas-solid momentum transfer:

$$\mathbf{I}_{gm} = F_{gm}(\mathbf{u}_{sm} - \mathbf{u}_g) \tag{21}$$

which is the product of interphase drag coefficient between the gas and solid phases (F_{gm}) and the slip velocity between the two phases . The interphase drag coefficient depends on the drag model that is being employed.

It should be noted that for cases where the particle diameter doesn't resemble a perfect sphere, the particle diameter used in the correlations is modified. The sphericity of a particle indicates how spherical a particle is. A sphericity of unity signifies that the particle is a perfect sphere. The modified particle diameter is:

$$d_p = \psi \overline{d_p} \tag{22}$$

where $\overline{d_p}$ is the mean diameter and ψ is the estimated sphericity of the actual particles.

3.2.4.1. *Gidaspow model with blending function*

The Gidaspow model [10] calculates the interphase drag coefficient using two correlations depending on the local void fraction and a blending function. For void fractions less than 0.8, the Ergun equation is employed to calculate the interphase drag coefficient, and for void fractions

greater than or equal to 0.8 the Wen-Yu equation is used. To avoid a discontinuity between the models, the blending function φ_{gs} introduced by [10] is:

$$\varphi_{gs} = \frac{\arctan[150 \times 1.75(0.2 - \epsilon_s)]}{\sqrt{\pi}} + 0.5 \tag{23}$$

The interphase drag coefficient for the Gidaspow model has been implemented into MFIX using the formulation [44]:

$$F_{gm} = \left(1 - \varphi_{gs}\right) F_{gm(Ergun)} + \varphi_{gs} F_{gm(Wen-Yu)} \tag{24}$$

where F_{gm} for the dense phase uses the Ergun equation when $\epsilon_g < 0.8$:

$$F_{gm(Ergun)} = 150 \frac{\epsilon_{sm}^2 \mu_g}{\epsilon_g d_p^2} + 1.75 \frac{\epsilon_{sm} \rho_g}{d_p} \left|\mathbf{u}_{sm} - \mathbf{u}_g\right| \tag{26}$$

where F_{gm} for the dilute phase uses the Wen-Yu equation when $\epsilon_g \geq 0.8$:

$$F_{gm(Wen-Yu)} = \frac{3}{4} C_D \rho_g \epsilon_g \epsilon_{sm} \frac{\left|\mathbf{u}_{sm} - \mathbf{u}_g\right|}{d_p} \epsilon_g^{-2.65} \tag{27}$$

where

$$C_D = \begin{cases} \dfrac{24\left[1 + 0.15\left(\epsilon_g Re_m\right)^{0.687}\right]}{\epsilon_g Re_m} & for\ Re < 1000 \\ 0.43 & for \quad Re \geq 1000 \end{cases}$$

3.2.4.2. *Ahmadi Turbulence model*

Turbulence predictions for the carrier phase are obtained by using a modified *k-ϵ* model:

$$\varepsilon_1 \rho_1 \left[\frac{\partial k_1}{\partial t} + U_{1j} \frac{\partial k_1}{\partial x_j}\right] = \frac{\partial}{\partial x_i}\left(\varepsilon_1 \frac{\mu_1^t}{\sigma_k} \frac{\partial k_1}{\partial x_i}\right) + \varepsilon_1 \tau_{1_{ij}} \frac{\partial U_i}{\partial x_j} + \Pi_{k1} - \varepsilon_1 \rho_1 \epsilon_1 \tag{28}$$

$$\varepsilon_1 \rho_1 \left[\frac{\partial \epsilon_1}{\partial t} + U_{1j} \frac{\partial \epsilon_1}{\partial x_j}\right] = \frac{\partial}{\partial x_i}\left(\varepsilon_1 \frac{\mu_1^t}{\sigma_\epsilon} \frac{\partial \epsilon_1}{\partial x_i}\right) + \varepsilon_1 \frac{\epsilon_1}{k_1}\left(C_{1\epsilon} \tau_{1_{ij}} \frac{\partial U_i}{\partial x_j} - \rho_1 C_{2\epsilon} \varepsilon_1\right) + \Pi_{\epsilon 1} \tag{29}$$

Except for the exchange terms Π_{k1} and $\Pi_{\epsilon 1}$, the above equations are similar to the single phase *k-ϵ* model. Different relations are used for obtaining closures for stress and strain terms involved.

The Reynold's-Stress tensor, $\tau_{1_{ij}}$, is defined as:

$$\tau_{1_{ij}} = 2\mu_1^t S_{1ij} - \frac{2}{3}\delta_{ij}\left(\rho_1 k_1 + \mu_1^t \frac{\partial U_{1k}}{\partial x_k}\right) \tag{30}$$

Here, the mean strain-rate tensor, S_{1ij} , is written as:

$$S_{1ij} = \frac{1}{2}\left(\frac{\partial U_{1i}}{\partial x_j} + \frac{\partial U_{1j}}{\partial x_i}\right) \tag{31}$$

The eddy viscosity μ_1^t is defined as :

$$\mu_1^t = \rho_1 C_{1\mu}\left[1 + \left(\frac{\tau_{12}^x}{\tau_1^t}\right)\left(\frac{\varepsilon_2}{\varepsilon_2^{max}}\right)^3\right]^{-1}\frac{k_1^2}{\epsilon_1} \tag{32}$$

The terms Π_{k1} and $\Pi_{\epsilon 1}$ represent the influence of solids phase on the gas turbulence, and are defined by the following equations for the Ahmadi model:

$$\Pi_{k1} = \beta(3\Theta_s - 2k_1) \tag{33}$$

$$\Pi_{\epsilon 1} = 0 \tag{34}$$

The constants used in the *k-ϵ* modeling approach are maintained the same as the ones used for single-phase modeling [49].

Turbulence predictions within the dispersed phase are obtained using:

$$\varepsilon_2\rho_2\left[\frac{\partial\Theta_s}{\partial t} + U_{2j}\frac{\partial\Theta}{\partial x_j}\right] = \frac{\partial}{\partial x_i}\left(\varepsilon_2\rho_2\lambda_2\frac{\partial\Theta}{\partial x_i}\right) + \varepsilon_2\rho_2\tau_{2ij}\frac{\partial U_{2i}}{\partial x_j} + \Pi_{k2} - \varepsilon_2\rho_2\epsilon_2 \tag{35}$$

where granular energy is defined as $\Theta_s = 1/3\langle u_2 u_2\rangle_2$

The interaction term is defined as:

$$\Pi_{k2} = \beta\left(\frac{2k_1}{1 + \frac{\tau_{12}^x}{\tau_1}} - 3\Theta_s\right) \tag{36}$$

Granular energy dissipation, ϵ_2, is

$$\epsilon_2 = 12(1-e^2)\varepsilon_2^2\rho_2 g_0\frac{\Theta_s^{\frac{3}{2}}}{d_p} \tag{37}$$

The solids granular conductivity for the Ahmadi model is defined as:

$$\kappa_2 = 0.1306\rho_2 d_p(1+e^2)\left(\frac{1}{g_0} + 4.8\varepsilon_2 + 12.1184 g_0\varepsilon_2^2\right)\sqrt{\Theta_s} \tag{38}$$

3.2.5. *Solid-solids momentum transfer*

The momentum transfer ($\mathbf{I}_{ml}$) between the solids in the momentum Eqn. 3 is

$$\mathbf{I}_{ml} = F_{sml}(\mathbf{u}_{sl} - \mathbf{u}_{sm}) \tag{39}$$

which is the product of the coefficient for the interphase force between the solid phases m and l (F_{sml}) and the slip velocity between the two solid phases $(\mathbf{u}_{sl} - \mathbf{u}_{sm})$. The coefficient for the interphase force is derived from a simplified version of the kinetic theory:

$$F_{sml} = \frac{3(1+e_{lm})\left(\frac{\pi}{2} + \frac{C_{flm}\pi^2}{8}\right)\epsilon_{sl}\rho_{sl}\epsilon_{sm}\rho_{sm}\left(d_{pl}+d_p\right)^2 g_{0lm}\left|\mathbf{u}_{sm} - \mathbf{u}_g\right|}{2\pi\left(\rho_{sl}d_{pl}^3 + \rho_{sm}d_p^3\right)} \tag{40}$$

where e_{lm} and C_{flm} are the coefficient of restitution and coefficient of friction between the l^{th} and m^{th} solid-phase particles, respectively, and g_{0lm} is the radial distribution function at contact for a mixture of hard spheres.

3.2.6. *Granular energy*

The constitutive relationships for the transfer of granular energy between the gas phase and the m^{th} solid phase (ϕ_{gm}) and the diffusive flux of granular energy ($\mathbf{q}_{\theta_{sm}}$) are

$$\phi_{gm} = -3F_{gm}\theta_m \tag{41}$$

$$\mathbf{q}_{\theta_{sm}} = -\frac{15d_p\rho_{sm}\epsilon_{sm}\sqrt{\pi\theta_{sm}}}{4(41-33\eta)}\left[1 + \frac{12}{5}\eta^2(4\eta-3)\epsilon_{sm}g_{0mm} + \frac{16}{15\pi}(41-33\eta)\eta\epsilon_{sm}g_{0mm}\right]\nabla\theta_{sm} \tag{42}$$

where

$$\eta = \frac{1}{2}(1+e_{mm}) \tag{43}$$

The constitutive relationship for the rate of granular energy dissipation (γ_{θ_m}) is

$$\gamma_{\theta_m} = \frac{12}{\sqrt{\pi}}(1-e_{mm}^2)\frac{\rho_{sm}\epsilon_{sm}^2}{d_p}g_{0mm}\theta_{sm}^{\frac{3}{2}} \tag{44}$$

The partial slip boundary conditions for the particle-wall interactions are employed, where the slip velocity is:

$$\mathbf{u}_{sm,slip}\,.\,\bar{\bar{\sigma}}_{sm}.\,\mathbf{n} + \frac{\pi\sqrt{3}}{6\epsilon_{sm,max}}\epsilon'\epsilon_{sm}\rho_{sm}g_{0mm}\theta_{sm,t}^{1/2}|\boldsymbol{u}_{sm}, slip|^2 = 0 \tag{45}$$

and the boundary condition for the translational fluctuation energy flux is:

$$-\mathbf{n}\cdot\mathbf{q}_{sm} = \frac{\pi\sqrt{3}}{4\epsilon_{sm,max}}(1-e_w^2)\epsilon_{sm}\rho_{sm}g_{0mm}\theta_{sm,t}^{\frac{3}{2}} + \mathbf{u}_{sm,slip}\cdot\sigma_{sm}\cdot\mathbf{n} \tag{46}$$

The slip velocity is defined as:

$$\mathbf{u}_{sm,slip} = \mathbf{u}_{sm} - \mathbf{u}_w \tag{47}$$

where $\mathbf{u}_w$ is the wall boundary velocity.

3.3. Numerical Methodology

The governing equations are discretized using a finite volume approach on a staggered grid to reduce numerical instabilities. Velocities are stored at the cell surfaces, and scalars, such as void fraction and pressure are stored at the center of the cell. Discretization of time derivatives are first order and discretization of spatial derivatives are second-order. A variable time-stepping scheme is also employed to improve convergence and execution speeds. The following sections will discuss the higher order discretization schemes used for the convective terms and the modifications employed for the SIMPLE algorithm to facilitate convergence.

3.3.1. *Higher Order Discretization*

To increase the accuracy of the numerical schemes, higher order discretization methods can be employed for the convective terms. A prevailing issue is that second order schemes tend to oscillate near discontinuities. Apart from being undesirable in the final solution, the convergence is also affected by the production of unphysical solutions. Dealing with these discontinuities motivated the development of higher order schemes such as total variation diminishing (TVD) schemes that does not produce oscillations. TVD schemes use a limiter that bounds the value of a general scalar variable Φ at the control volume face, when the local variation in Φ is monotonic, thereby preventing any spurious oscillations [50]. Figure 3.1 is a representation of the TVD scheme. If the TVD scheme is used, then the value of the scalar at the east face of the cell, Φ_e, would be

$$\Phi_e = \xi_e \Phi_E + (1 - \xi_e)\Phi_P \tag{50}$$

where ξ_e is the convection weighting factor, and can be calculated from the downwind factor dwf_e as follows:

if $u_e \geq 0$

$$\Phi_e = dwf_e \Phi_E + (1 - dwf_e)\Phi_P \tag{51}$$

$$\xi_e = dwf_e \tag{52}$$

if $u_e < 0$

$$\Phi_e = dwf_e\Phi_P + (1 - dwf_e)\Phi_E \tag{53}$$

$$\xi_e = 1 - dwf_e \tag{54}$$

The down-wind factor calculated as per the Superbee method, which can be applied to explicit conservative convection and diffusion schemes of any order of accuracy, is:

$$dwf_e = \frac{1}{2}\max[0, \min(1,2\theta), \min(2, \theta)] \tag{55}$$

If the MUSCL discretization scheme is used the down-wind factor is defined as:

$$dwf_e = \frac{1}{2}\max[0, \min(2\theta, 0.5 + 0.5\theta, 2] \tag{56}$$

where $\theta = \widetilde{\Phi}_c/(1 - \widetilde{\Phi}_c)$ and $\widetilde{\Phi}_c$ is calculated using the following expressions:

if $u_e \geq 0$

$$\widetilde{\Phi}_C = \frac{\Phi_P - \Phi_W}{\Phi_E - \Phi_W} \tag{57}$$

if $u_e < 0$

$$\widetilde{\Phi}_C = \frac{\Phi_P - \Phi_{EE}}{\Phi_E - \Phi_{EE}} \tag{58}$$

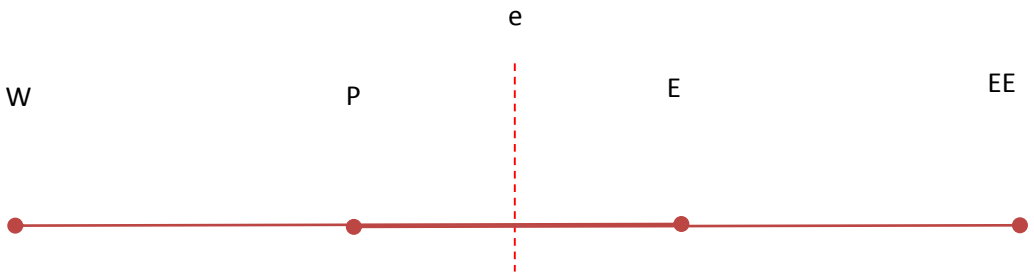

Figure 3.1. Node locations for the TVD scheme.

3.3.2. *Modified SIMPLE method*

The semi-implicit method for pressure linked equations (SIMPLE) was originally developed for single phase flow. MFIX makes use of a modified SIMPLE algorithm in order to handle

multiphase flow. The SIMPLE algorithm incorporates a pressure correction equation as a convenient equation for solving the pressure field appearing in the three single phase momentum equations. For multiphase flow, there is no unique way to derive such an equation as there are more than one continuity equation. Instead a solids volume fraction correction is used. There is no requirement for $\frac{\partial P_s}{\partial \epsilon_s}$ not to vanish when $\epsilon_s \rightarrow 0$, which is the case when a solids pressure correction is used.

In densely packed regions, a small increase in solids volume fraction tends to cause the solids pressure to increase exponentially. Solids volume fraction corrections are therefore under-relaxed to attain numerical stability as follows:

$$\text{If } (\epsilon_m)_{new} > \epsilon_p \text{ and } \epsilon'_m > 0$$

$$\epsilon'_m = \omega_{\epsilon_m} \epsilon'_m \tag{59}$$

where $(\epsilon_m)_{new}$ is volume fraction calculated at a particular cell, ϵ_p is the volume fraction for the packed region, ω_{ϵ_m} is an under-relaxation factor, and ϵ'_m is the correction value of solids volume fraction with guessed value of ϵ^*_m where

$$\epsilon_m = \epsilon^*_m + \epsilon'_m \tag{60}$$

Since gas-solids flows are inherently unstable, transient simulations are performed. To ensure numerical stability, smaller time steps and under relaxation are used for convergence.

Chapter 4. Fluidized Bed Dynamics for Non-uniform Inlet Conditions[1]

4.1. Introduction

Recent investigations of different modeling approaches based on capturing the relevant physics were performed for sand and biomass particles by the authors [51]. The paper was preliminary work related to adjusting the bed material to the same amount as the fluidizing material. The motivation for the work was that the process of fluidization is not always uniform in an experiment due to the hole arrangement in a distributor plate. The work is continued here, presenting an optimal way to account for the hydrodynamics by comparing with experiments for fluidized beds containing single solids phase and binary mixtures. In addition, non-uniformity of the particles is addressed in the proposed modeling. The next section discusses basic theory of fluidization, followed by the numerical methodologies used. The new models are then introduced and validated first for the fluidized bed containing glass particles for a single solids phase, and then used for a glass-ceramic binary mixture, where all of the materials fall within the Geldart B classification [52]. The efficacy of this simple modeling approach is demonstrated by validating with experimental pressure drop and minimum fluidization velocity.

4.2. Fluidized Bed Modeling

In the field of fluidization, it has been established that as the inlet velocity increases through an initially static bed of granular material, the pressure drop increases linearly until the critical value of minimum fluidization is reached [53]. Afterward the pressure drop remains constant with increasing velocity. Theoretically, the maximum pressure drop ΔP that can be attained by the fluidized bed system can be calculated using a force balance equating the weight of the bed material mg with the pressure at a cross-section:

$$\Delta P = \frac{mg}{A} \tag{61}$$

where A is the cross-sectional area normal to the incoming flow. The bulk density ρ_b can be expressed in terms of the mass and the initial height of the bed h_0:

[1] A significant part of this chapter is published in ***Modeling and Predicting Gas-solid Fluidized Bed Dynamics to Capture Non-uniform Inlet Conditions***, by Santhip K. Kanholy, Jillian Chodak, Brian Y. Lattimer, and Francine Battaglia, ASME Journal of Fluids Engineering, 134(11), Paper 111303, 2014. Used with permission by ASME.

$$\rho_b = \frac{m}{Ah_o} \tag{62}$$

The relation between bulk density ρ_b and particles density ρ_p can be used to determine the corresponding solids volume fraction:

$$\varepsilon_s = \frac{\rho_b}{\rho_s} \tag{63}$$

Hence if the total volume fraction occupied by the solids phase is known, the initial gas volume fraction ε_{mf} can be estimated:

$$\varepsilon_{mf} = 1 - \varepsilon_s \tag{64}$$

The Ergun equation [54] can be used to obtain an expression to calculate minimum fluidization velocity U_{mf} by using the bed material properties for particle density ρ_p, gas volume fraction ε_{mf} and gas properties for viscosity μ_g and density ρ_g:

$$U_{mf} = \frac{\left(\psi \bar{d}_p\right)^2 \left(\rho_p - \rho_g\right) g \varepsilon_{mf}^3}{150 \mu_g \left(1 - \varepsilon_{mf}\right)} \tag{65}$$

For cases where the particle diameter is not perfectly spherical, the modified (or effective) particle diameter $d_p = \psi \bar{d}_p$ is used where $\bar{d}_p$ is the mean (or nominal) diameter and ψ is the estimated sphericity of the actual particles. The sphericity is the ratio of surface area of a sphere with the same volume as the actual particle to the surface area of the actual particle.

Mixtures can be approximated using a single solids phase by defining representative particle characteristics to model multiple solids phases in a fluidized bed [55]. A mixture diameter and mixture density is determined using the mixture components. Mass fraction for solids phase component *i* is defined using the mass m_i occupied by the corresponding solids phase and the total mass *M*:

$$X_i = \frac{m_i}{M} \tag{66}$$

Mixture density [22] is obtained as a weighted average of the particle density based on the mass fraction:

$$\rho_{mix} = \left(\sum_{i=1}^{n} \frac{X_i}{\rho_i} \right)^{-1} \tag{67}$$

The mixture diameter [22] is obtained as a weighted average based on the experimental mass fraction, mixture density and the particle diameters.

$$d_{mix} = \left(\rho_{mix} \sum_{i=1}^{n} \frac{X_i}{\rho_i d_i} \right)^{-1} \tag{68}$$

Equations (67-68) can be used in Eqn. (65) by replacing the particle properties ρ_p and d_p with ρ_{mix} and d_{mix}, respectively. The solids volume fraction in Eqn. (64) can be modified to include the summation of all the solids phases.

4.3. Experimental Conditions

A series of experiments were performed in a cold flow, non-reacting fluidized bed to quantify the effects of particle diameter and density on the bed dynamics for both single particle and binary mixtures. The experimental setup is shown in Figure 4.1 with a complete description provided elsewhere [8]. The cylindrical fluidizing chamber had a 10.4 cm inner diameter and was 68.5 cm high. The chamber was fabricated of 7.62 cm thick clear cast acrylic to allow the observation of the fluidization during the experiments. The fluidizing air entered the bottom of the chamber through a distributor plate and exited the top of the chamber, which was open to atmosphere. The distributor plate was a 1.778 cm thick acrylic disk containing a series of 2 mm diameter holes such that there was a hole every 2.4 cm^2. To prevent bed material from clogging the distribution plate, a 44-mesh screen with 0.04 cm openings was attached to the distribution plate. Air was fed into the system at the bottom of the plenum located directly below the distributor plate. The 10.4 cm diameter, 15.2 cm high plenum was filled with glass beads and contained a moist sponge to humidify the air to reduce static electricity effects in the fluidizing chamber.

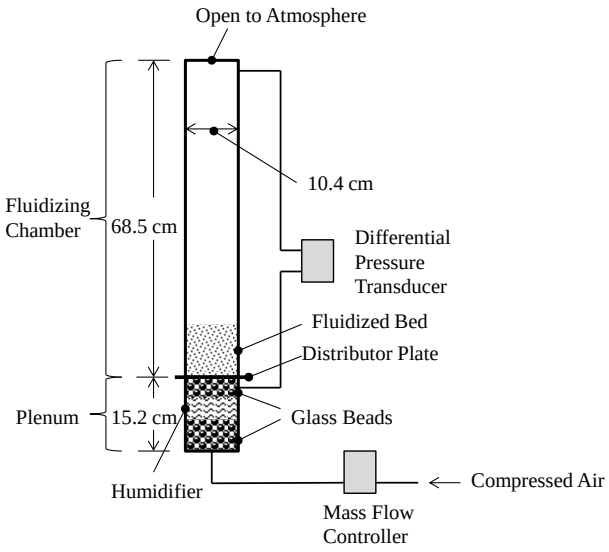

Figure 4.1. Experimental apparatus.

The fluidized bed contained instrumentation to measure the air flow rate into the system, pressure drop, and bed height. Air flow rate was controlled and measured using an Alicat Scientific MCR-500SLPM 16 Series mass flow controller with a range of 0-500 SLPM and accuracy ± 0.2% of full scale. Pressure difference across the fluidized bed was determined through measuring the differential pressure between the pressure in the plenum below the distributor plate and at the top of the fluidized bed in the freeboard close to the exit to atmosphere. This was done using a Setra DPT-2640-010D-A pressure transducer rated for 0 to 2480 Pa with an accuracy of ±0.25% of full scale. Data was collected using a National Instruments SCXI-1600 Controller module with a SCXI-1300 General Purpose terminal block. The signal-processing program for data acquisition was created using National Instruments LabView 8.6, which collected data at 1 Hz. Experiments were recorded using a video camera focused in on the bed area. A scale was attached to the side of the fluidization chamber to capture the height of fluidized material during testing.

Experimental results discussed in this paper are for tests with the bed containing particles 10.4 cm (one diameter) high in the bed. To measure the differential pressure with particles in the bed, the air flow rate was gradually increased to the maximum level and then decreased in approximately 1-2 cm/s increments to determine the differential pressure profile. Pressure drop at a given air superficial velocity was determined by subtracting the differential pressure with no particles in the bed with the differential pressure with particles in the bed.

4.4. Simulation Description

To model and simulate the experiments described in the previous section, a uniform inlet velocity was specified as the distributor plate and ambient conditions at the outlet. The no-slip wall boundary condition was specified for the gas phase and a partial-slip wall boundary condition for the solids phase. A two-dimensional (2D) domain in Cartesian coordinates was modeled to represent the centerplane of the cylindrical geometry of the experimental setup. It has been shown that a 2D domain is sufficient for modeling moderately bubbling fluidized beds [14,45,56,57,58]. The 2D rectangular grid consisted of 40×116 cells distributed uniformly with cell sizes of 0.26 cm and 0.27 along the horizontal and vertical directions respectively. Previous work [19] has shown that the chosen grid resolution is sufficient with relative errors less than 2% for a coarser grid.

4.5. Results and Discussion

Pressure drop measurements were obtained from experiments performed for different materials and are used for validation with CFD results. In order for the system to reach the maximum pressure drop, the entire bed material must fluidize. However, experiments usually have regions where material does not fluidize and remains static at the bottom and sides of the geometry, leading to slightly lower pressure drop. The primary difference between the measured value and the maximum pressure drop depends on the uniformity of the flow created by the distributor plate configuration. Conventionally, fluidized beds are modeled by considering the entire mass of the material that is present in the bed and uniform flow at the inlet based on the superficial gas velocity. The measured solids volume fraction for the static bed is also used as an initial condition for the simulations. The validation study for different fluidized bed models presented in this section will help ensure proper modeling for further CFD studies to better understand the fluidization hydrodynamics involved for single solids phase and binary mixtures.

4.5.1. *Single solids phase fluidized beds*

4.5.1.1. *Glass particles (500-600 μm)*

Simulations were performed for a single solids phase fluidized bed containing glass particles with a mean diameter of 550 μm. The modeling parameters are shown in Table 4.1(Sim-0), and were derived from the experiments. As a first step in the validation study, the predicted pressure drop is compared with the experiments in Figure 4.2. The experiments report that the minimum fluidization velocity is approximately 22 cm/s after which point the measured pressure drop is

1318 Pa [8]. The simulations capture the same pressure trends prior to fluidization but overpredict both U_{mf} and ΔP after fluidization. However, it should be noted that the simulations predict a pressure drop of 1509 Pa, which corresponds to the maximum pressure drop obtained using Eqn. (61) when the entire bed fluidizes. The mismatch in pressure drop may be attributed to regions in the bed that have not fluidized, which may occur if a distributor plate does not sufficiently create a uniform inlet flow.

Table 4.1. Parameters for the single solids phase models of glass particles (d_p = 500-600 μm).

Properties	Exp	Sim-0	Sim-1	Sim-2	Sim-3
d_p(μm)	500-600	550	550	550	440
e (-)	-	0.95	0.95	0.95	0.95
ρ_s (g/cm^3)	2.5	2.5	2.5	2.5	2.5
ρ_b (g/cm^3)	1.479	1.479	*1.576*	*1.576*	1.479
m (g)	1306.4	1306.4	*1392.3*	*1141.6*	*1141.6*
ε_{mf} (-)	0.41	0.41	*0.37*	*0.37*	0.41
h_0 (cm)	10.4	10.4	10.4	*8.5*	*9.1*

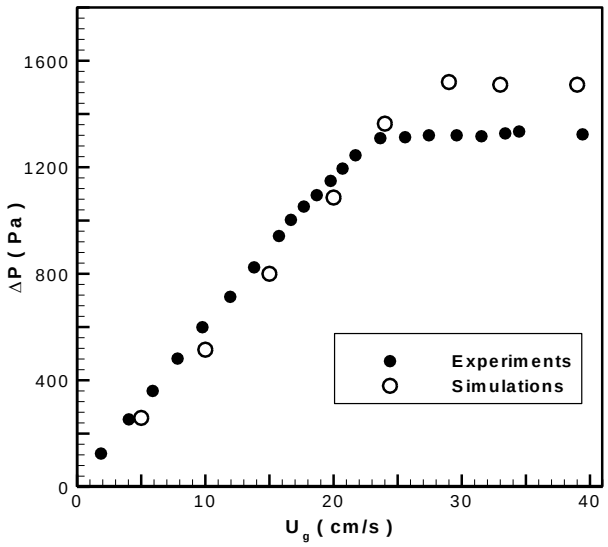

Figure 4.2. Pressure drop versus superficial gas velocity for glass particles (d_p = 500-600 μm) comparing experiments with simulations.

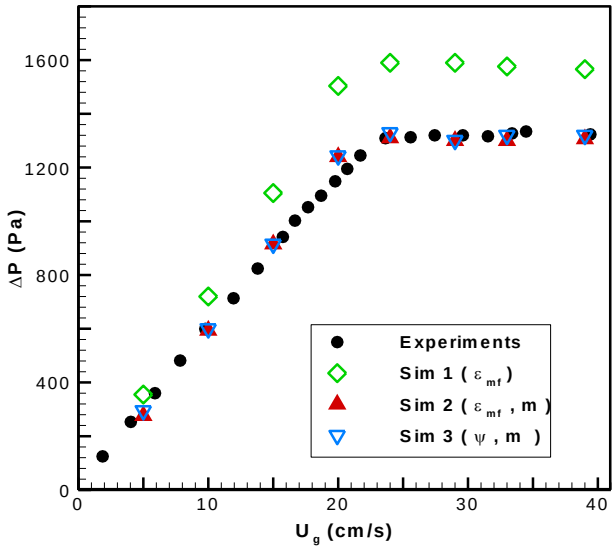

Figure 4.3. Pressure drop versus superficial gas velocity for glass particles (d_p = 500-600 µm) comparing experiments with simulations using single solids phase models.

A second approach considered to improve the computational modeling was to adjust the initial void fraction in the static bed by using the experimental value for U_{mf} and solving for ε_{mf} in Eqn. (65). While the U_{mf} measured in the experiment using a graphical method is reported as 22 cm/s, the U_{mf} deduced from the pressure measurements shown in Figure 4.2 is slightly higher, about 24 cm/s, and has been used for determining the model parameters for the simulations. By modifying the initial fluidization void fraction, Eqn. (64) provides a new ε_s, which is used to calculate ρ_b (Eqn. 63) and therefore an adjusted mass m (Eqn. 62). The adjusted parameters are italicized in Table 4.1 as Sim-1. Predictions based on the Sim-1 model, shown in Figure 4.3 (the parenthetic variables in the legend are the primary adjusted parameters), are able to capture U_{mf} fairly well compared to the previous set of simulations (Sim-0) that made use of experimental parameters for ε_{mf} and m. However the mass specified using the Sim-1 model is larger than the amount of glass beads used in the experiments and thus does not accurately represent the real system.

A third approach to further improve the simulations involved adjusting the mass present in the bed by making use of the measured pressure drop (ΔP = 1318 Pa). The new values for ε_{mf} and ρ_b found in the Sim-1 model are used again. In addition, the fluidizing mass contributing to the measured pressure drop is calculated using Eqn. (61). Finally, the initial height is adjusted using Eqn. (62) so that all of the equations are coupled. The adjusted parameters are labeled Sim-2 in

Table 4.1. Figure 4.3, shows that the predictions made using the Sim-2 model agree very well with the measured U_{mf} and the pressure drop. The Sim-2 model is thus able to account for regions of the bed that do not fluidize, and clearly demonstrates the need for adjusting the bed mass to accurately predict the pressure drop.

In order to further examine the effects of sphericity on the predictions, Figure 4.3 also compares the Sim-2, and Sim-3 model with the experiments. The Sim-2 model assumed a sphericity of unity to determine the initial void fraction present in the bed using Eqn. (65). For the Sim-3 model, the sphericity was calculated using Eqn. (65) and the experimental values of ε_{mf} and U_{mf}. The model also makes use of the adjusted bed mass by calculating the initial mass present in the bed using the measured pressure drop and Eqn. (61). The measured bulk density is used with Eqn. (62) to adjust the initial bed height h_o. The Sim-3 model predictions are in very good agreement with the experiments and the Sim-2 model for U_{mf} and ΔP. Based on the results, the Sim-3 model is a better representation of the real system and is recommended for modeling the fluidized bed.

4.5.1.2. *Ceramic particles (500-600 μm)*

To test the accuracy of the single solids phase models, ceramic particles with a diameter range of 500-600 μm were used. Ceramic particles were a challenge to model as the particles were hollow, unlike the glass particles. The experiments provided a nominal density to represent non-uniform particle material and a nominal diameter range based on the sieving process. In fact, during fluidization some of the particles were severely deformed into the shape of a disk (i.e., almost two-dimensional). Thus, the low estimate of the initial void fraction (0.28) obtained after defluidizing the bed in the experiments is attributed to the deformation and slight breakage of the ceramic particles.

Table 4.1 lists the parameters for the different models applied for the ceramic particles and Figure 4.4 compares the predictions. Similar trends observed for the glass particles are also observed for the ceramic particles with some variations. The Sim-0 model, which uses the experimentally measured ε_{mf} and d_p, underpredicts Umf drastically (a value of ~3 cm/s that is shown as circles in Figure 4.4) and overpredicts ΔP. The Sim-1 model, which uses a better estimate of the initial void fraction present in the bed compares very well for Umf and ΔP. The agreement with the pressure drop predictions is due to the fact that the mass changes when ε_{mf} is adjusted to

account for the amount of material that fluidizes. Hence estimating the void fraction using the measured U_{mf} can be considered as a better and valid approach as demonstrated by the Sim-1 and Sim-2 model. The Sim-2 model that uses both an adjusted void fraction and an adjusted bed mass predicts both Umf and pressure drop very accurately.

Table 4.2. Parameters for the single solids phase models of ceramic particles (d_p = 500-600 µm).

Properties	Exp	Sim-0	Sim-1	Sim-2	Sim-3
d_p(µm)	500-600	550	550	550	1342
e (-)	-	0.85	0.85	0.85	0.85
ρ_s (g/cm^3)	1.079	1.079	1.079	1.079	1.079
ρ_b (g/cm^3)	0.775	0.775	*0.579*	*0.579*	0.775
m (g)	684.5	684.5	*511.4*	*546.8*	*546.8*
ε_{mf} (-)	0.28	0.28	*0.46*	*0.46*	0.28
h_0 (cm)	10.4	10.4	10.4	*11.1*	*8.3*

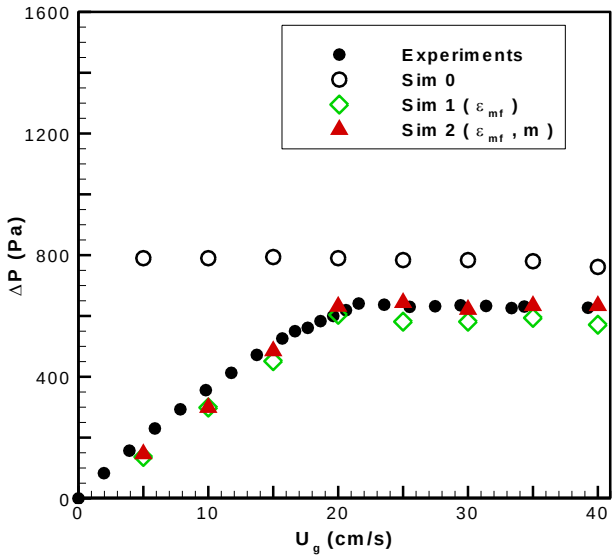

Figure 4.4. Pressure drop versus superficial gas velocity for ceramic particles (d_p =500-600 µm) comparing experiments with simulations using single solids phase models.

For the ceramic particles, it is interesting to note that the Sim-3 model predicts an unphysical effective particle diameter of 1342 μm that falls outside of the diameter range used in the experiments; thus, the simulations were not performed. Possible reasons for an unphysical effective particle diameter could be attributed to the non-uniformity of these particles, both in shape and density of the hollow ceramic material.

4.5.1.3. *Ceramic particles (1000-1120 μm)*

The models were also tested particles for ceramic particles with a nominal diameter range of 1000-1120 μm. The particles presented similar difficulties in that they were susceptible to breakage and deformation. Figure 4.5 compares the pressure drop predictions with the experiments and the parameters used in the models are listed in Table 4.3. The trends observed here for the simulations were similar to those observed for both glass and ceramic particles of 500-600 μm size range. It should be noted that the Sim-1 and Sim-2 models gave initial void fraction value of 0.33, which less than the theoretical value of 0.37 for a perfectly packed bed of spherical particles. However, the value of 0.33 could be realistic because the ceramic particles break and deform. It is also noted that the effective particle diameter used in the Sim-3 is smaller than the measured particle diameter range, which can be justified considering that broken particles were found in the bed. In spite of these issues, the Sim-2 and Sim-3 model were able to accurately predict pressure drop and obtain fairly close predictions for U_{mf}.

Table 4.3. Parameters for the single solids phase models of ceramic particles (d_p =1000-1120 μm).

Properties	Exp	Sim-0	Sim-1	Sim-2	Sim-3
d_p(μm)	1000-1120	1060	1060	1060	530
e (-)	-	0.85	0.85	0.85	0.85
ρ_s (g/cm^3)	1.3	1.3	1.3	1.3	1.3
ρ_b (g/cm^3)	0.681	0.681	*0.877*	*0.877*	0.681
m (g)	601.9	601.9	*775.1*	*402.7*	*402.7*
ε_{mf} (-)	0.48	0.48	*0.33*	*0.33*	0.48
h_0 (cm)	10.4	10.4	10.4	*5.4*	*7.0*

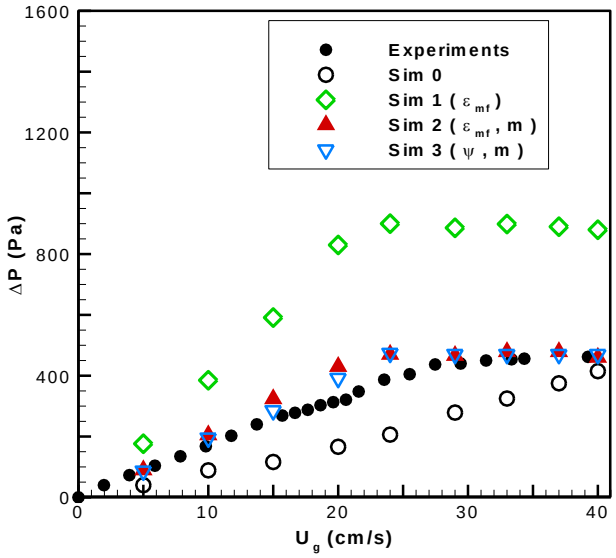

Figure 4.5. Pressure drop versus superficial gas velocity for ceramic particles (d_p =1000-1120 μm) comparing experiments with simulations using single solids phase models.

4.5.2. *Binary Mixtures*

Two different binary mixtures were modeled: a mixture of glass and ceramic particles with diameters of 500-600 μm and a mixture of ceramic particles with two diameter ranges, 500-600 μm and 1000-1120 μm. The previous studies in Sect. 5.1 helped to establish an effective particle diameter for the glass beads and ceramic particles. These effective particle diameters for each material are used to represent each solids phase (see Table 4.4). For example, glass beads were found to have an effective particle diameter of 479 μm based on the Sim-3 model. For the ceramic particle study (Sect. 5.1.2), the Sim-2 model indicated that the effective particle diameter is 550 μm. However, based on the Sim-3 model for the larger size ceramic particles (Sect. 5.1.3), the effective particle diameter was 530 μm. The binary mixture models also account for the fluidizing mass by using the measured ΔP and estimating ε_{mf} using the measured U_{mf}, as described in the next sections.

4.5.2.1. *Glass-Ceramic binary mixture*

Four mixture models were tested for the binary mixture with glass and ceramic particles of the same size range (500-600 μm): Sim-S, Sim-B0, Sim-B1 and Sim-B2. For the Sim-S model, the binary mixture was modeled using a single solids phase characterized with a mixture density and

mixture diameter using Eqns. (67) and (68). These mixture properties for the characteristic solids phase are substituted into Eqn. (65) along with the measured U_{mf} to determine the initial fluidizing void fraction, which is then used to find the corresponding ε_s (Eqn. 64) and ρ_b (Eqn. 63). The mass of the bed is also adjusted using the measured ΔP and Eq. (61). The new values for m and ρ_b are used to adjust the initial height of the bed (Eqn. 62) and are shown in Table 4.4 (Sim-S model) and the data is presented in Figure 4.6. The Sim-S model is able to capture the measured pressure drop trend and is also able to predict the measured U_{mf}.

Table 4.4. Parameters for the binary mixture models of glass-ceramic particles.

Properties	**Experiment**		**Sim-S**	**Sim-B0**		**Sim -B1**		**Sim -B2**	
	Glass	Ceramic	Mix. Props.	Glass	Ceramic	Glass	Ceramic	Glass	Ceramic
d_p (μm)	500 - 600	500 - 600	*515*	479	550	479	550	479	550
ρ_s (g/cm^3)	2.5	1.079	*1.725*	2.5	1.079	2.5	1.079	2.5	1.079
m (g)	667.4	345.4	*834.4*	667.4	345.4	*549.8*	*284.6*	*489.0*	345.4
ρ_b (g/cm^3)	-	-	*0.980*	0.755	0.391	*0.646*	*0.334*	*0.554*	*0.391*
Xi (-)	0.66	0.34		0.66	0.34	0.66	0.34	*0.59*	*0.41*
ε_g (-)	-		*0.43*	*0.34*		*0.43*		*0.42*	
h_0 (cm)	10.4		*10.0*	10.4		*10.0*		10.4	

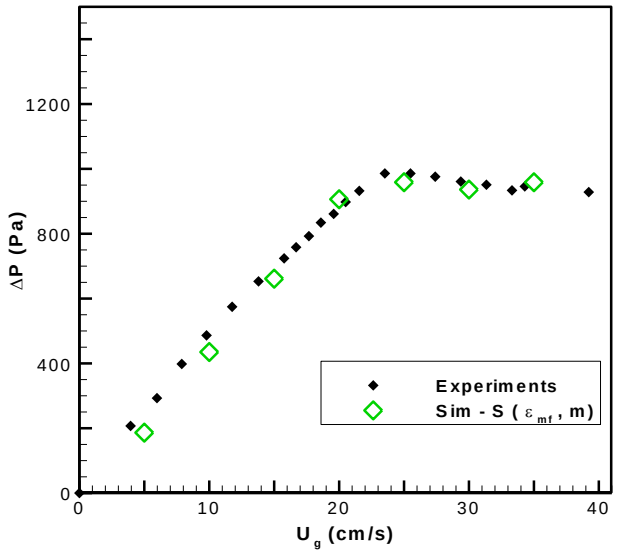

Figure 4.6. Pressure drop versus superficial gas velocity for glass-ceramic binary mixture comparing experiments with simulations using the single solids phase model.

Although it is extremely encouraging that a single solids phase can be used to model a binary mixture, it is of value to determine how best to model two solids phases based on the conclusions of Sect 4.1. The Sim-B0 model represents two solids phases for the glass and ceramic particles based on the effective particle diameters determined in Sect 4.1, and the mass and particle densities reported in the experiments. The solids volume fraction is then defined for the binary system:

$$\varepsilon_{s,total} = \frac{1}{V_{total}}\left(\frac{m_1}{\rho_1} + \frac{m_2}{\rho_2}\right) \tag{69}$$

where the subscripts 1 and 2 correspond to the two solids phases of glass and ceramic particles. Equation (14) is solved using the experimental conditions for mass and density of each material and the total volume of the initial system. The initial void fraction is then found using Eq. (64) and the individual bulk densities are solved using Eqn. (63). The properties are shown in Table 4.4 (Sim-B0) and the corresponding pressure drop curve is shown as open circles in Figure 4.7. Clearly, U_{mf} is significantly underpredicted (10 cm/s) compared to 22 cm/s as measured in the experiments and the overall pressure drop is overpredicted. The large discrepancies were not unexpected based on the study presented in Sect. 4.1. Therefore, another model was tested to better approximate the amount of mass fluidizing for each solids phase.

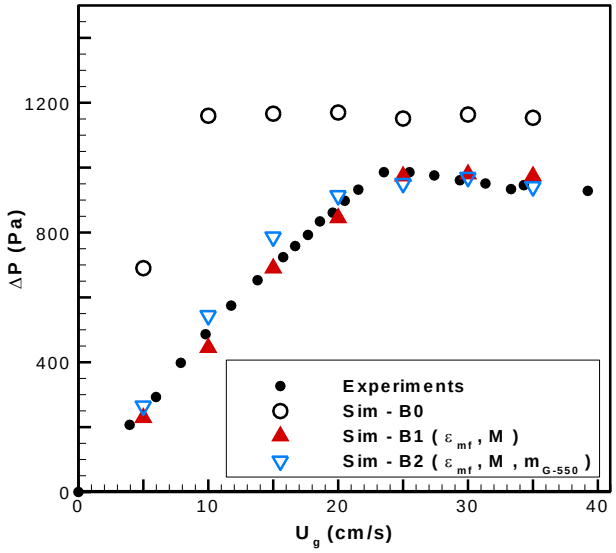

Figure 4.7. Pressure drop versus superficial gas velocity for glass-ceramic binary mixture comparing experiments with simulations using binary mixture models.

The Sim-B1 model uses the Sim-S procedure to calculate void fraction, total mass and adjusted height, but new masses for each component are needed. The mass fractions reported in the experiments along with the new total mass M are substituted into Eqn. (66) to calculate new mass components. As seen in Figure 4.7, the Sim-B1 model accurately captures the fluidization trends of the binary mixture. Because the ceramic particles have a smaller density, a final model was considered to determine if all of the material fluidized before the glass beads. The Sim-B2 model assumes that the entire amount of ceramic particles fluidizes and thus the mass of the glass beads ($m_{G\text{-}550}$) is adjusted to correspond to the measured pressure drop. As a consequence, the mass fractions are calculated using Eqn. (66). In addition, new bulk densities are used in Eqn. (69) to find the new initial void fraction (Eqn. 64). Interestingly, the Sim-B2 and Sim-S models predict virtually identical trends. The similarity is because the glass beads have a larger density that contributes more to the mixture density in the Sim-S model. However, it is important to note that after the point of minimum fluidization, the pressure drop predictions are the same for the Sim-S, B1 and B2 models. Comparing all four models, the Sim-B1 model performs exceptionally well for the glass-ceramic mixture.

4.5.2.2. *Ceramic-Ceramic binary mixture*

For the ceramic-ceramic binary mixture with two particle sizes, all four binary mixture models were tested (see Table 4.5). Comparisons with experimental results are shown in Figure 4.8. As shown previously, the Sim-B0 model is unable to predict the ΔP and U_{mf}, but the Sim-S model, which uses a single solids phase to model the ceramic-ceramic binary mixture, is able to predict U_{mf} and ΔP fairly well. The Sim-B1 model, which accounts for the actual fluidizing mass is able to predict U_{mf} and ΔP as well, but predicts a very subtle distinct slope prior to fluidization. The Sim-B2 model, which assumes full fluidization of the lower density ceramic-550 microns (and a new mass is calculated for the larger particle, $m_{C\text{-}1060}$) particles fails to capture ΔP and U_{mf}. It is possible that the issues mentioned pertaining to the ceramic particles could be a possible reason for such a behavior. Overall, the Sim-B1 model, which uses the mixture properties to adjust void fraction and calculate new masses for each phase based on the actual fluidizing mass performs the best.

Table 4.5. Parameters for the binary mixture models of ceramic-ceramic particles.

Properties	Experiment		Sim-S	Sim-B0		Sim -B1		Sim -B2	
	Ceramic	Ceramic	Mix. Props.	Ceramic	Ceramic	Ceramic	Ceramic	Ceramic	Ceramic
d_p (μm)	500 - 600	1000-1120	*540*	550	530	550	530	550	530
ρ_s (g/cm^3)	1.079	1.3	*1.173*	1.079	1.3	1.079	1.3	1.079	1.3
m (g)	345.4	309.2	*455.5*	345.4	309.2	*240.3*	*215.1*	345.4	*110.1*
ρ_b (g/cm^3)	-	-	*0.607*	0.39	0.35	*0.32*	*0.29*	*0.39*	*0.12*
Xi (-)	0.53	0.47		0.53	0.47	0.53	0.47	*0.76*	*0.24*
ε_g (-)	-		*0.48*	*0.37*		*0.48*		*0.54*	
h_0 (cm)	10.4		*8.8*	10.4		*8.8*		10.4	

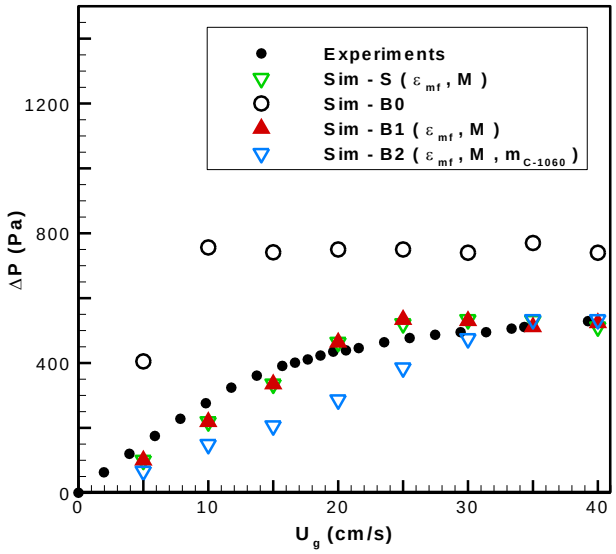

Figure 4.8. Pressure drop versus superficial gas velocity for ceramic-ceramic binary mixture comparing experiments with simulations using binary mixture models.

4.6. Conclusions

CFD modeling of fluidized bed containing single solids particles and binary solids particles were performed for glass particles and ceramic particles of 550 μm and ceramic particles of 1060 μm average particle diameters, and for binary solids fluidized bed consisting of glass-ceramic and ceramic-ceramic mixtures. The need to adjust the mass and the initial void fraction present in the bed using experimentally measured pressure drop and the minimum fluidization velocity was clearly demonstrated for both single solids and binary mixtures. Doing so helps to account for the material that does not fluidize due to the distributor plate in addition to the non-uniformity of the

particles due to deformation. Different single solids fluidized bed models and binary solids fluidized bed models were presented based on adjusting these parameters. All models were validated with experimental pressure drop measured for all the particles. Of the single solids fluidized bed models, Sim-3 model performed best, which used the measured void fraction for the defluidized static bed in order to estimate an effective particle diameter and adjust for the fluidizing material. The Sim-B1 model performed best among the binary solids fluidized bed models and uses better estimations of the fluidizing mass of each solids phase.

Chapter 5. Multiple Jet Interactions For Different Distributor Plates

5.1. Introduction

Fluidized bed technology has found its application in gasification due to its efficient heat transfer and mixing characteristics [10]. The gases enter through the distributor plate at the bottom of the bed to promote mixing between the different phases involved, enhancing the heat transfer, mass transfer and chemical reaction rates, which makes it very useful within the processing industry. However, the hydrodynamics of a fluidized bed are complicated, thus making it difficult to evaluate its efficiency with chemical reactions. For proper performance and efficient operation, it becomes necessary to model the interactions between the two phases within the fluidized bed. Typically, distributor plates are modeled as uniform inlet velocity conditions, rather than a series of jets, and are appropriate for modeling reactors where the distributor holes are uniformly placed. However, in cases when the distributor holes are not uniformly distributed, this could lead to inaccurate modeling predictions. Hence, there is a need to investigate how best to accurately model the distributor plate configuration.

The motivation for this study is to capture the fluidization hydrodynamics for reactor distributor plate configurations with multiple jets and validate with experiments. For this purpose distributor plate configurations with a single row of 9 and 5 holes are selected for a quasi-2D reactor setup. Hydrodynamics are predicted using both 2D and 3D simulations.

5.2. Problem Description

The fluidized bed reactor used in the experiments[2] consisted of a rectangular geometry 25.4 cm wide, 1.27 cm deep, and 30 cm high. Since the depth of the bed is much smaller than the bed width, the reactor can be considered as a quasi-2D geometry. Humidified air entered a plenum chamber to reduce electrostatic effects and was then injected into the bed through a perforated distributor plate with 2 mm diameter holes. A differential pressure transducer was used to measure pressure drop between the plenum and the freeboard. The distributor plate had 9 equally spaced 2-mm-diamter holes with a 2.8 cm pitch. In the first configuration all the holes were open. In the second configuration only alternate holes were kept open by blocking 4 holes. PIV and DIA were

[2] The experimental data was provided courtesy of Dr. Brian Lattimer and Gaurav Agarwal, Extreme Environments, Robotics & Materials Laboratory, Mechanical Engineering Department, Virginia Tech.

used to obtain time-averaged solids volume fractions and solids particle flux information. Complete details of the experiments performed are found in [9]. For the simulations, rather than using a uniform inlet velocity condition, as is usually implemented, the inlet is modeled as a series of holes for which an appropriate jet inlet velocity is specified, and will be discussed next.

The first domain tested in the CFD modeling is a two-dimensional (2D) plane in Cartesian coordinates, which represents a plane that cuts through the center of the holes. A three-dimensional (3D) model of the distributor configurations is also tested. For the 2D model, the grid resolution consists of 125 × 74 cells, 125 × 148 cells and 250 × 148 cells distributed uniformly in the *x*- and *z*-directions, respectively, as the coarse, medium and find grid respectively. For the 3D model, the grid is uniformly discretized with 125 × 74 × 8 cells, 125 × 148 × 8 cells and 250 × 148 cells × 8 For the 5-holed distributor plate, only the fine grid is considered for both 2D and 3D simulation.

It must also be mentioned that the orifice velocity for the 2D jet model is significantly lower than the value used in the 3D model. Based on previous work [19], if the geometry was cylindrical and if the distribution of jets were symmetric about the axis, then a 2D uniform inlet velocity condition would have been able to capture the hydrodynamics of the fluidized bed. However, when the geometry is modeled as 2D, preservation of the true 3D flow rate would require extremely high velocities for 2D jets. To properly account for the 2D inlet velocity, the 3D flow rate per unit width is used to specify the jet velocity.

5.3. Discussion and Results

The CFD modeling for the two- and three-dimensional models of the 9-holed and 5-holed distributor configuration are validated with measurements from the experiment for different hydrodynamic parameters such as pressure drop across the bed, volume fractions, solids velocity distributions, and deadzone distributions. Analysis of deadzones based on the distributor configurations is also considered. The conditions used in the experiments and simulations are shown in Table 5.1 for a bed medium of glass beads.

Table 5.1. Experimental conditions and model parameters for the simulations of the nine-holed distributor.

Models / Properties	Exp	Sim	
	-	2D	3D
d_p (μm)	500-600	550	550
ψ (-)	-	0.9	0.9
e (-)	-	0.95	0.95
ρ_s (g/cm^3)	2.5	2.5	2.5
ρ_b (g/cm^3)	1.541	1.541	1.541
ε_g (-)	0.383	0.383	0.383
U_{mf} (cm/s)	23.3	20.3	20.3

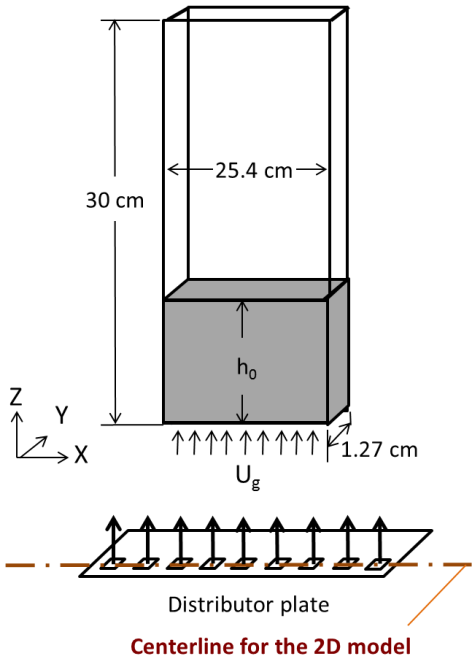

Figure 5.1. Schematic of the computational domain and the distributor plates modeled in the simulations.

5.3.1. *Distributor plate with 9 jets*

5.3.1.1. *Pressure drop*

The pressure drop through the bed is used to validate the CFD modeling for the two and three-dimensional models of the 9-holed distributor plate. Simulations were performed for coarse, medium and fine grid resolutions, for both two-dimensional and three dimensional simulations, as shown in Figure 5.2(a-b). The experiments indicate a linearly increasing pressure drop with

increasing inlet gas velocity until the point of minimum fluidization. After U_{mf} = 23 cm/s, the rate of increasing pressure drop slightly lowers. The difference between experimental measurements and the theoretical value of pressure drop expected when the entire bed mass is fluidizing, as indicated by the black line, indicates that there are regions of deadzones above the distributor formed between the jets. With further increasing gas velocity, the jets are able to entrain more solid particles into fluidization, subsequently increasing the pressure drop across the fluidized bed.

For the 2D simulations (Figure 5.2(a)), there is a linearly increasing pressure drop with increasing inlet gas velocity until the point of fluidization following which the pressure drop remains constant. All three grids predict similar pressure drop. It is interesting to note that the 2D simulations indicate smaller regions of deadzone mass as is indicated by the difference between simulation predictions and theoretical value expected if the entire bed mass fluidizes. The 3D simulations indicate a similar trend of linearly increasing pressure drop until the point of fluidization. However with further increasing velocity, the pressure drop initially lowers and then increases again. The pressure drop predicted is dependent on the 3D grid resolution. With increasing velocity, the coarse grid predicts the highest pressure drop, followed by the medium grid and fine grid. The fine grid predictions are closer to the experimental measurements than coarse and medium grid. The dependency of the pressure drop predictions on the grid indicates how the improved grid resolution used in the 3D simulations is able to resolve the jets with more accuracy, thus predicting deadzone mass closer to what was observed in the experiments.

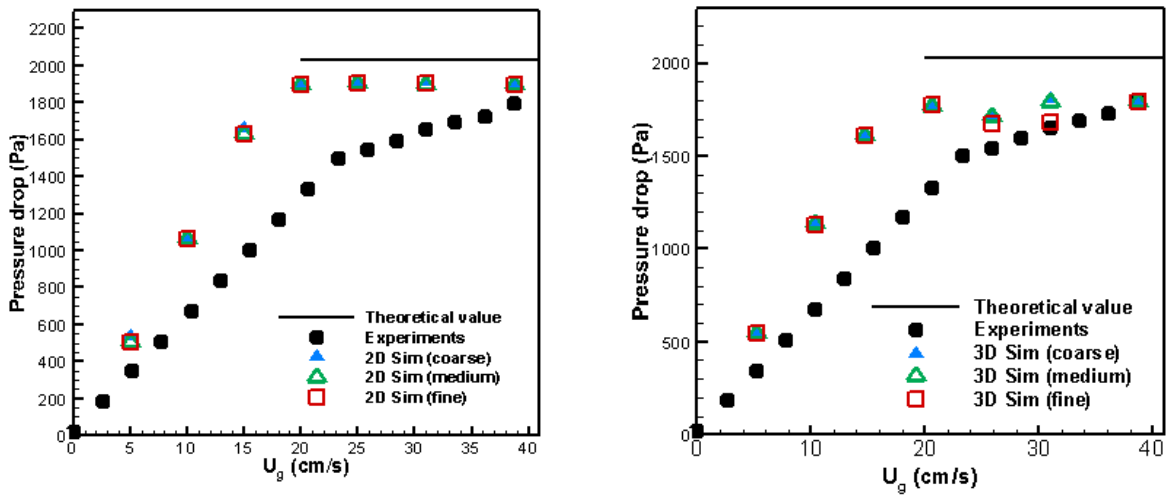

(a) 2D simulations (b) 3D simulations

Figure 5.2. Pressure drop vs. inlet gas velocity comparing different grid resolutions for both (a) 2D and (b) 3D simulations

5.3.1.2. *Solids volume fraction*

Time averaged solids volume fractions are compared between experiments and simulations for the inlet velocity of $U_g = 1.35\ U_{mf}$. The time averaging is performed for 3.3 s for both experiments and simulations. Spatially averaged solids volume fraction across the bed width are plotted against the height of the bed and compared between experiments and 2D and 3D simulations. The coarse, medium and fine grid are compared for both 2D and 3D simulations. Both simulations are in accordance with the experiments by predicting a fairly constant solids volume fraction of about 0.55 until the height of about 15 cm above the distributor plate, above which the amount of solids significantly decreases throughout the remainder of the freeboard. The 2D simulations predict a slightly higher bed expansion in comparison with the experiments. The 3D simulations, which also allow solids to expand into the depth of the bed predict bed expansion height closer to the experiments.

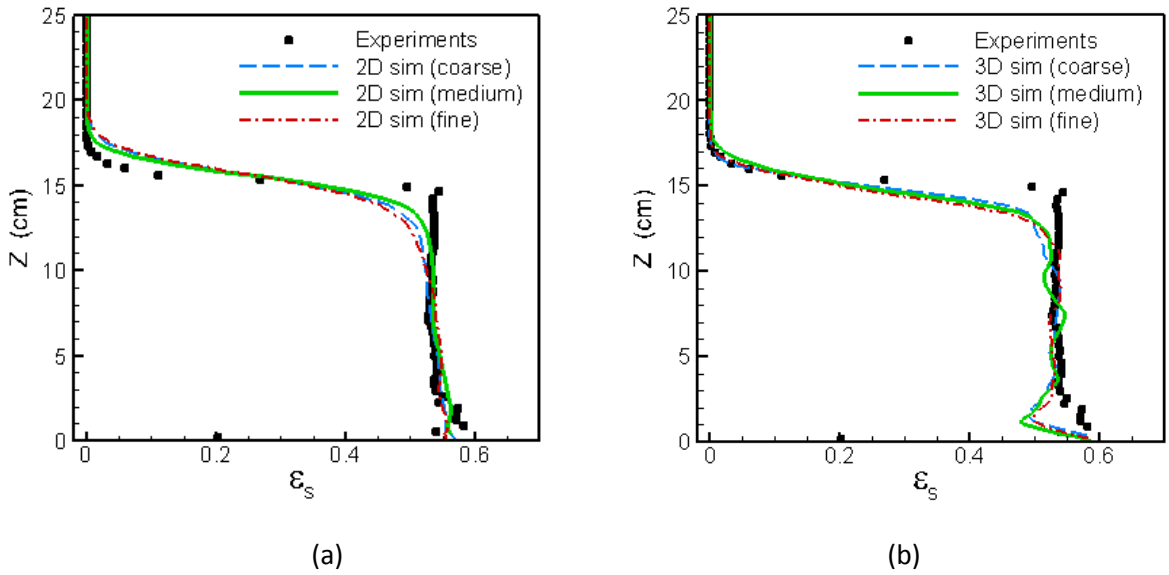

Figure 5.3. Solids volume fraction spatially-averaged across bed width versus height for (a) 2D simulations and (b) 3D simulations

Time averaged gas volume fraction contours are compared between 2D coarse, medium and fine grid simulations and the experiment in Figure 5.4. The time averaging is done for 3.3 s at a frequency of 25 Hz. The experiment shows the presence of more gas closer to the wall. This could be due to the Coanda effect, where jets closer to the wall attach, resulting in an accumulation of gases along the wall. The jets begin to spread and the effect of the jets decreases with bed height.

The jets appear to coalesce at a height of about Z = 5 cm, where there is more gases present. The 2D coarse grid simulation indicates the coalescence of the jets predominantly in the top half of the bed. The medium grid simulation indicates increased refinement of the distribution of void fraction throughout the bed when compared with the coarse grid simulations. The fine grid simulation is able to resolve the jets with finer flow details, while capturing the coalescence of the jets closer to the distributor plate. Even with just 2D simulations, the effects of increasing grid refinement can be easily observed with the gas distribution.

Time averaged gas volume fraction contours are also compared between experiments and the coarse, medium and fine grids for the 3D simulations in Figure 5.5. For the 3D simulations, void fraction contours are obtained after averaging three planes closest to the plane of the jets through the distributor. All three grid resolutions show coalescence of the jets symmetric about the vertical centerline. With increasing refinement of the grid, the evolution of the jets into the bed is captured with more detail. The jets also penetrate more into the bed with increasing grid refinement.

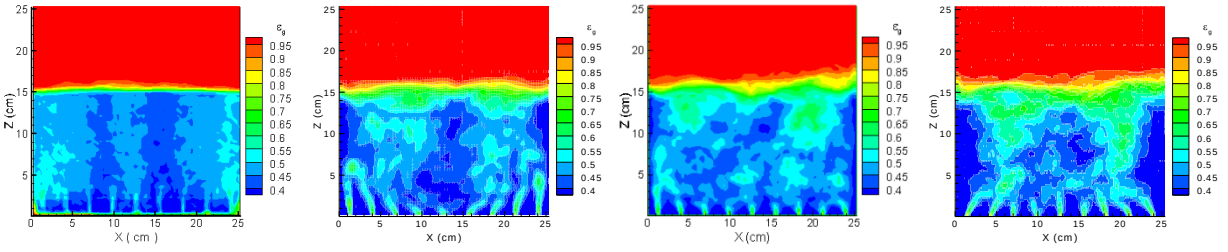

(a) (b) (c) (d)

Figure 5.4. Solid volume fraction contours of a plane through the distributor hole centerline comparing the (a) experiment (b) 2D coarse grid (c) 2D medium grid (d) 2D fine grid simulations.

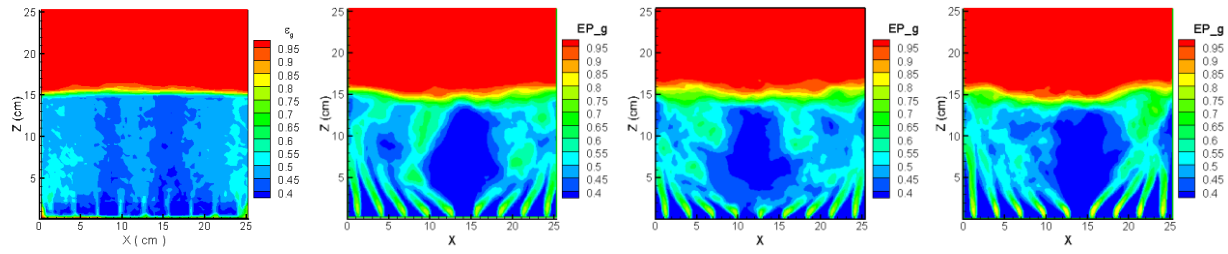

(a) (b) (c) (d)

Figure 5.5. Solid volume fraction contours of a plane through the distributor hole centerline comparing the (a) experiment (b) 3D coarse grid (c) 3D medium grid (d) 3D fine grid simulations.

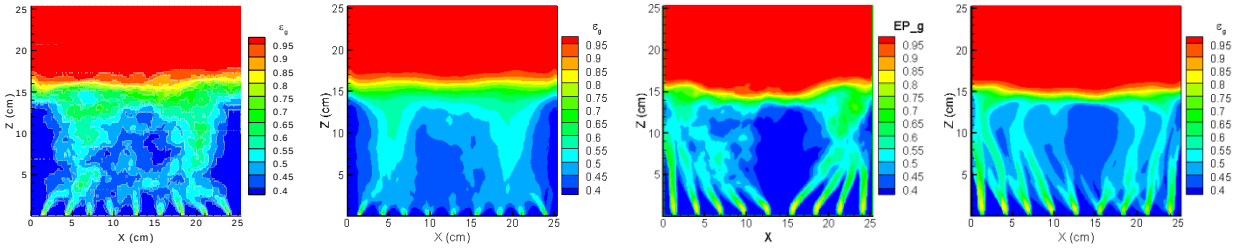

Figure 5.6. Solid volume fraction contours of a plane through the distributor hole centerline comparing different time averages for (a) 2D simulation (3.3 s) (b) 2D simulation (10 s) (c) 3D simulation (3.3 s) (d) 3D simulation (15 s)

The effects of increasing the sample size in the time-averaging is analyzed for both 2D and 3D simulations in Figure 5.6. With additional samples, the effects of the jets are smeared for both 2D and 3D simulations. The 2D and 3D simulations with more time-averaging show a wider span for the jets. However, even with just 3.3 seconds of time-averaging, the prominent features of the flow such as the coalescence of the jets are still captured for both 2D and 3D simulations.

Figure 5.7 and Figure 5.8 compare the solids volume fraction profiles at Z = 0.5 cm, 1 cm, 2cm and 4 cm between the experiments and coarse, medium and fine grids of the 2D and 3D simulations respectively. In general the solids volume fraction profiles compare fairly well with the experiments, with the average value remaining the same. The jets can be easily identified at 0.5 cm and 1 cm, with the lowest peaks coinciding with the jet holes of the distributor plate. The effect of the jets reduces with increasing height. Eventually the variations in solids volume fraction becomes less once the gas jets merge within the bed medium.

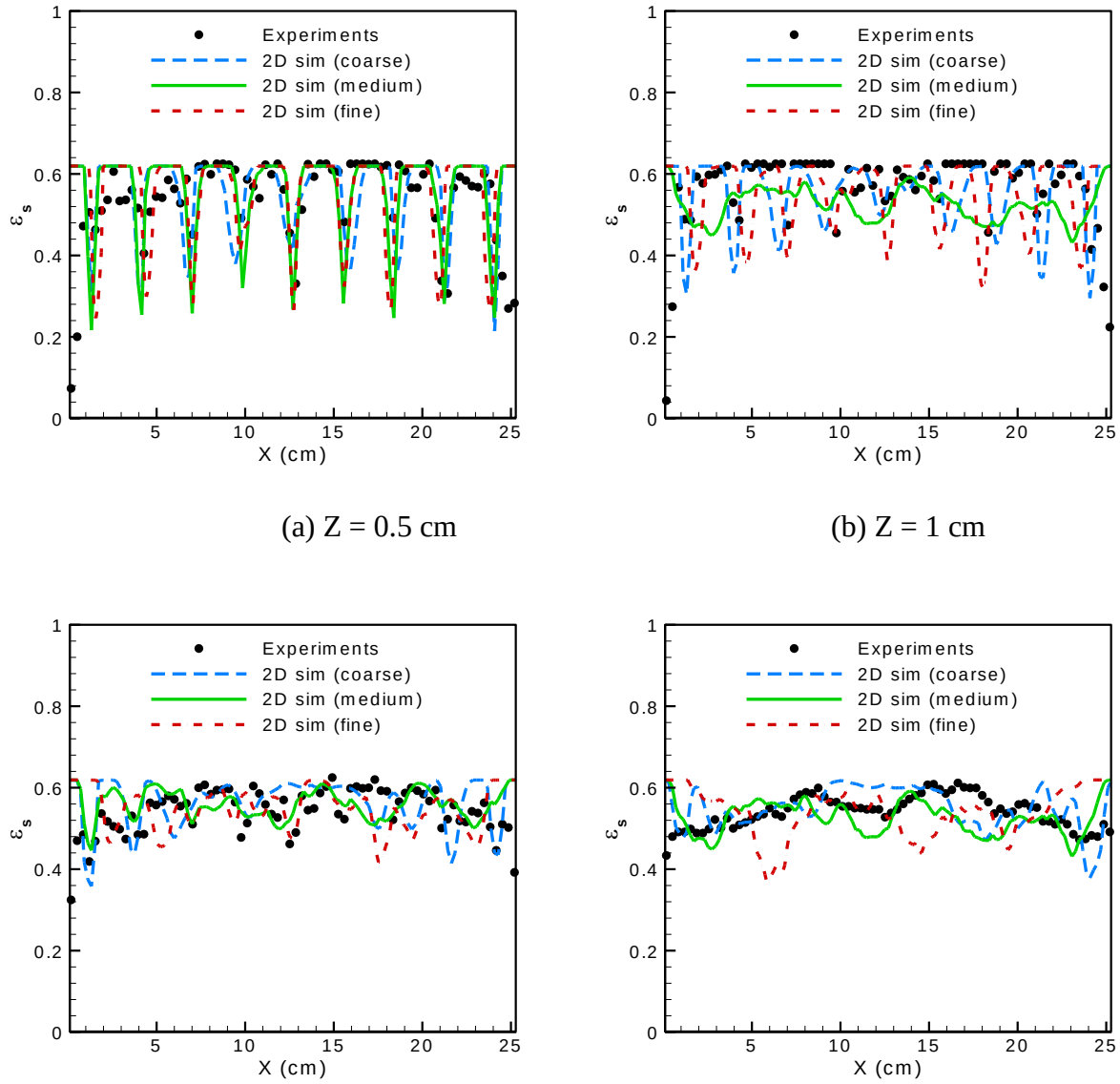

(a) Z = 0.5 cm

(b) Z = 1 cm

(c) Z = 2 cm

(d) Z = 4 cm

Figure 5.7. Solids volume fraction profiles comparing the experiment, 2D coarse, medium and fine grid simulations at heights above the distributor plate corresponding to (a) Z = 0.5 cm , (b) Z = 1 cm (c) Z = 2 cm , (d) Z = 4 cm at an inlet velocity of 31 cm/s.

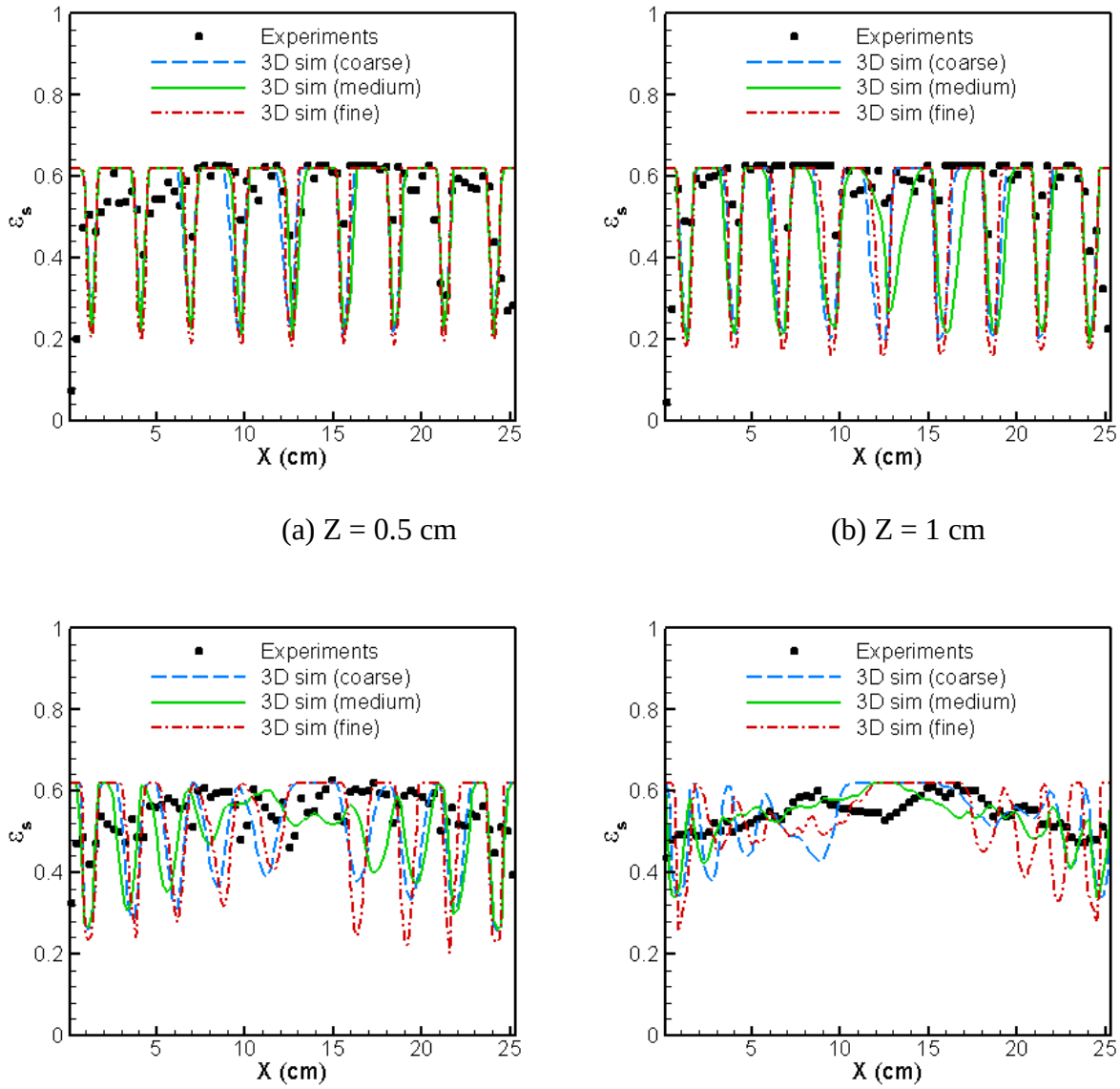

(a) Z = 0.5 cm

(b) Z = 1 cm

(c) Z = 2 cm

(d) Z = 4 cm

Figure 5.8. Solids volume fraction profiles comparing the experiment, 3D coarse, medium and fine grid simulations at heights above the distributor plate corresponding to (a) Z = 0.5 cm , (b) Z = 1 cm (c) Z = 2 cm , (d) Z = 4 cm at an inlet velocity of 31 cm/s.

5.3.1.3. *Solids velocity*

Figure 5.7 shows time-averaged normalized solids velocity magnitude contours superimposed with solids velocity vectors for 2D and 3D simulations with coarse, medium and fine grids along with the experiments. For the sake of clarity, every fourth vector is shown for 2D and 3D medium and fine grids. The experiments indicate regions of high velocity magnitude at the top of the bed possibly indicating eruption of a bubble, thus throwing solids particles into the freeboard. With increasing grid refinement, 2D and 3D simulations show regions of circulating particles on either side of the bed with increased refinement.

It is interesting to see that upon increasing grid resolution for 2D simulations, the fine grid indicates movement of solids particles vertically downwards closer to the wall, while all the 3D simulations show the particles moving vertically upwards along the walls. It is encouraging to note that 3D simulations indicate similar regions of high magnitude when compared with the experiment.

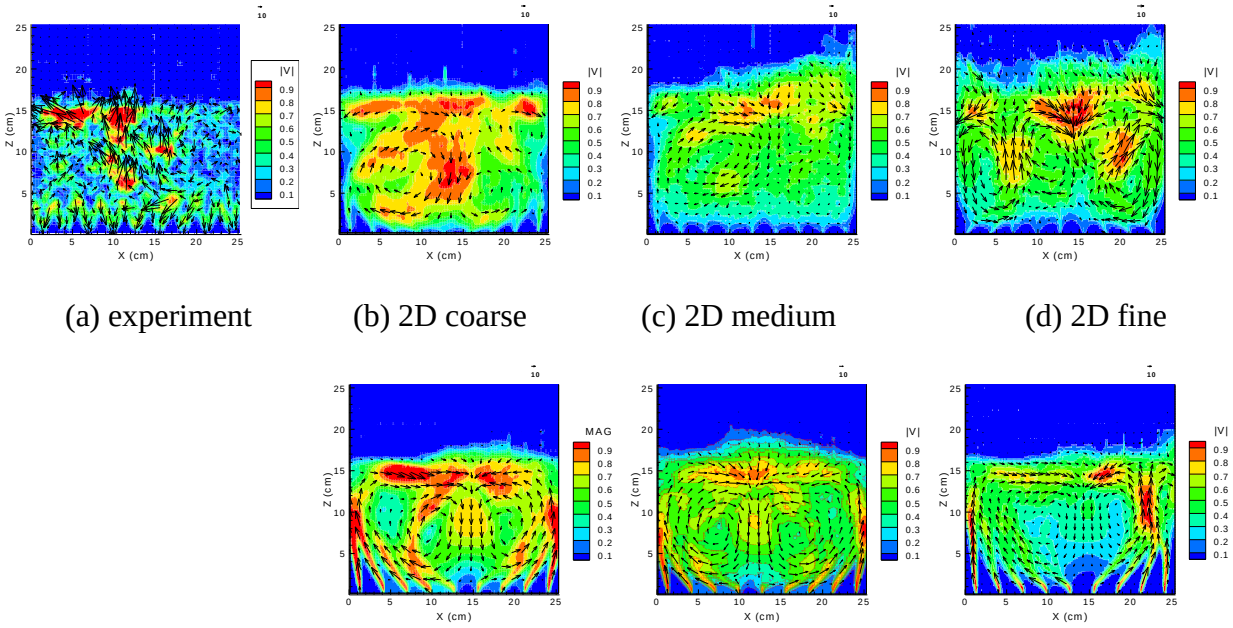

(a) experiment (b) 2D coarse (c) 2D medium (d) 2D fine

(e) 3D coarse (f) 3D medium (g) 3D fine

Figure 5.9. Solids velocity vectors and contours comparing the experiment, coarse, medium and fine grids for 2D and 3D simulations

5.3.2. *Distributor plate with 5 jets*

5.3.2.1. *Pressure drop*

A different distributor plate with 5 inlet holes is modeled using 2D and 3D simulations with the fine grid. Pressure drop predicted by the simulations is validated with measurements made in the experiments, shown in Figure 5.10. The experiments indicate a linearly increasing pressure drop with increasing inlet gas velocity until the point of minimum fluidization. After U_{mf} = 20 cm/s, the pressure drop remains constant. The difference between experimental measurements and the pressure drop expected if the entire bed mass fluidized, indicates that there are regions of deadzones that have formed between the jets above the distributor. In comparison with the 9-holed distributor, there is less mass fluidizing for the 5-holed distributor.

For the 2D simulations (Figure 5.10), there is a linearly increasing pressure drop with increasing inlet gas velocity until the point of fluidization, following which the pressure drop increases slightly. The 3D simulations predict a similar trend of linearly increasing pressure drop until fluidization. However with further increasing velocity, the pressure drop begins to decrease unlike the 2D simulations, indicating that the fluidizing mass decreases with increasing gas velocity. The 3D simulations give predictions closer to the experiments than the 2D simulations, especially at higher inlet velocities.

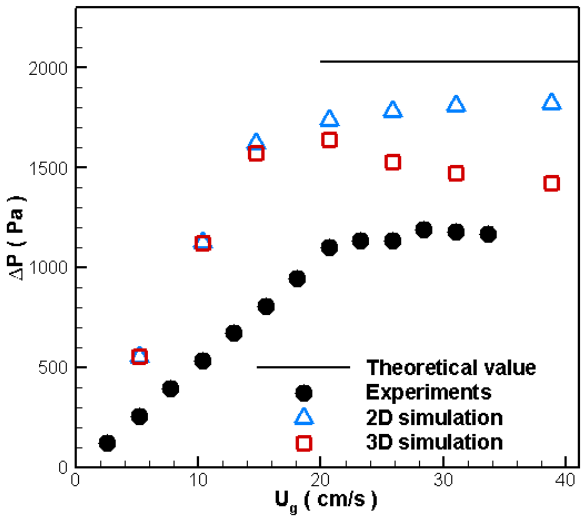

Figure 5.10. Pressure drop vs. inlet gas velocity comparing experiments, 2D and 3D simulations

5.3.2.2. *Solids volume fraction*

Time averaged solids volume fraction contours of the 5-holed distributor are shown in Figure 5.11(a-c) for an inlet velocity of 31 cm/s. Results are compared between the experiments, and the 2D and 3D simulations using the fine grid. Time averaging is performed for 3.3 s for both experiments and simulations. In the experiments, the jets are observed to emerge vertically from the distributor. For the 2D simulation, the gas jets tend to direct the flow towards the walls, even for the central jet because solids descend in the central bed region. The 3D simulations show jets penetrating deeper into the bed and erupting at the free surface, thus forming channels from the distributor plate to the top of the bed, while in the experiments the jets diffuse into the bed.

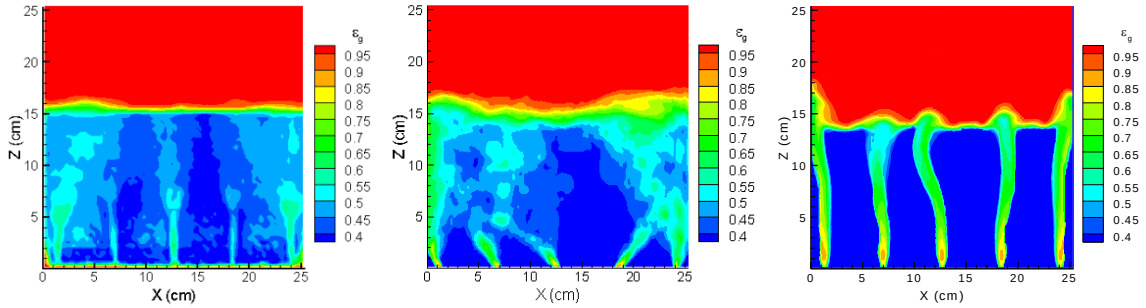

(a) Experiments (b) 2D simulation (c) 3D simulation

Figure 5.11. Solid volume fraction contours of a plane through the distributor hole centerline comparing the (a) experiment (b) 2D simulation (c) 3D simulation

Spatially-averaged solids volume fraction profiles are shown in Figure 5.12 for an inlet velocity of 31 cm/s, comparing both 2D and 3D simulations with experiments. Trends are similar to that observed for the distributor plate with 9 holes. Throughout the bed the solids volume fraction is uniform until about Z = 15 cm, above which solids volume fraction decreases steeply until the bed has fully expanded to a maximum height. The 2D simulation compares better with the experiments than the 3D simulation for the bed expansion height, as is apparent in Figure 5.11.

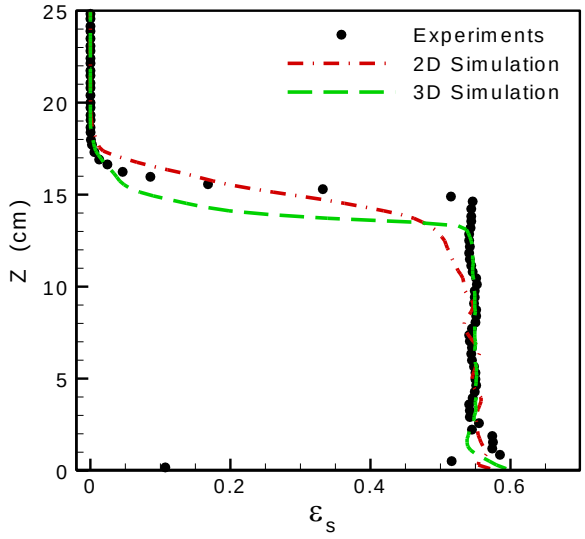

Figure 5.12. Solids volume fraction spatially-averaged across bed width versus height for experiments, 2D and 3D simulation at U_g = 31 cm/s

An additional comparison is considered between the experiments and the 2D and 3D simulations by examining solids volume fraction profiles at four different heights close to the distributor. Figure 5.13(a-d) compares the profiles at Z = 0.5 cm, 1 cm, 2 cm and 4 cm above the distributor. The simulations compare fairly well with the experiments at heights of 0.5 cm. The effect of the jets reduces with height as is seen from Figure 5.13(c-d). The 2D simulation is able to capture the decreasing effect of the jets, with the jets diffusing about Z = 2 cm. It is notable that the 3D simulations show a constant solids volume fraction profile in regions of the bed other than the jets. A possible explanation is that the high turbulence in the jets is not captured by the models that were used in the simulation.

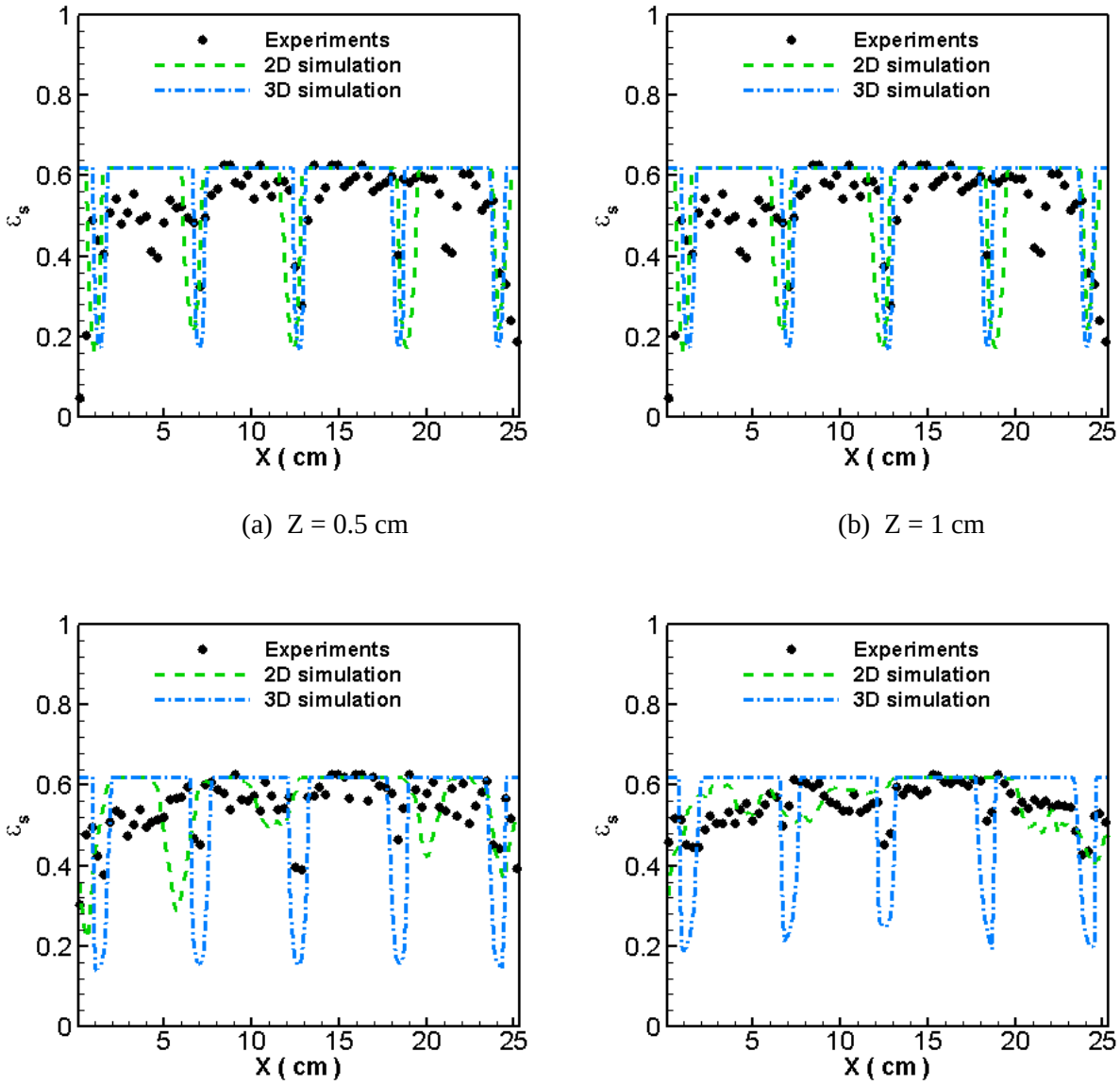

(a) Z = 0.5 cm

(b) Z = 1 cm

(c) Z = 2 cm

(d) Z = 4 cm

Figure 5.13. Solids volume fraction profiles comparing the experiment, 2D and 3D simulations at heights above the distributor plate corresponding to (a) Z = 0.5 cm, (b) Z = 1 cm, (c) Z = 2 cm, (d) Z = 4 cm at an inlet velocity of 31 cm/s

5.3.2.3. *Solids velocity*

Time-averaged normalized solids velocity magnitude contours superimposed with solids velocity vectors for 2D and 3D simulations are shown in Figure 5.14. For the 3D simulation, the first 3 planes close to the distributor holes are spatially averaged. For the sake of clarity, every

fourth vector is shown. Experiments show solid particles being entrained into the jets near the distributor plate. The experiments also show a bubble erupting close to Z = 12 cm. The simulations show that the particles are mostly moving vertically near the distributor plates for both 2D and 3D simulation. For the 3D simulation though, the jets remain vertical, and penetrate through the bed forming channels.

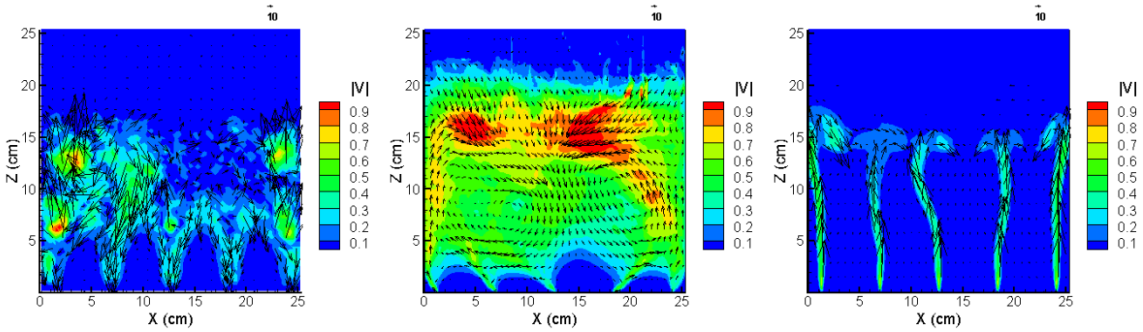

(a) Experiments **(b) 2D simulation** **(c) 3D simulation**

Figure 5.14. Solids velocity vectors and contours comparing the experiment, coarse, medium and fine grids for 2D and 3D simulations

5.3.3. *Deadzone estimation*

For further analysis of the hydrodynamics involved, solids velocity vectors for 3D simulations are further analyzed for both the 9-holed distributor plate and the 5-holed distributor plate. Since the 3D simulation is able to provide additional data with regard to the nature of the flow into the depth of the bed, studying the 3D solids velocity vectors could give additional insight into the nature of fluidization observed.

Figure 5.15(a-b) shows the time-averaged solids velocity vectors for the 3D simulation of the 9-holed distributor. Figure 5.15(a) shows the velocity vectors in 3D at different YZ planes at distances of X = 0.9 cm, 6.9 cm, 18.1 cm and 24.2 cm along the bed width. The solid particles are transferred vertically along the walls into the top of the bed. Depending upon where the slice is, at the top of the bed the particles are either transported into the middle of the bed or along the side walls to the walls behind the jets. The YZ planes closer to the middle shows particles moving towards the center of the bed, and the planes closer to the wall shows the particle being thrown to the walls behind the jets. The side-view (Figure 5.15(b)) also shows the solid particles being entrained into the jet near the bottom of the distributor plate, and being transferred towards the wall behind the jets at the top of the bed.

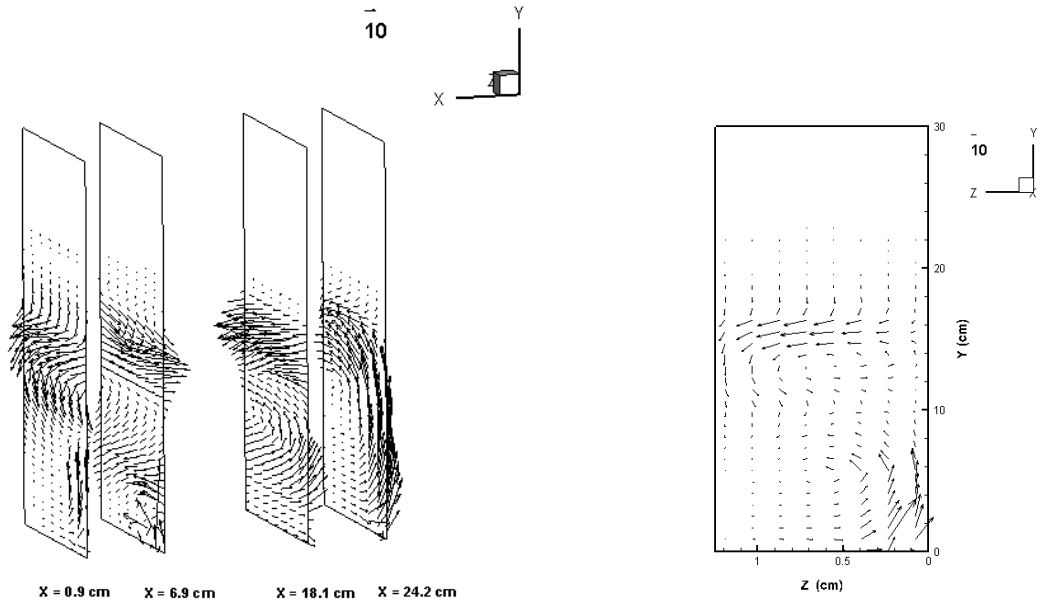

(a) YZ planes at different points along the bed width (b) Side view

Figure 5.15. Solids velocity vectors for the3D simulation of the 9-hole distributor at (a) different YZ planes along the bed width and (b) for a side-view through the bed

Figure 5.16(a-b) shows the time-averaged solids velocity vectors for the 3D simulation of the 5-holed distributor plate. Figure 5.16(a) shows the velocity vectors in 3D at different YZ planes at distances of X = 1.4 cm, 11.7 cm, 18.1 cm and 24.2 cm along the bed width. The 5-holed distributor plate 3D simulation shows a different pattern of movements for the solid particles in comparison with the 9-holed distributor. The 3D simulation indicates jets penetrating close to the front walls with the solid particles being thrown off the top of the bed towards the back wall. The side-view, in Figure 5.15(b) shows the solid particles being entrained into the jet near the bottom of the distributor plate, and being thrown to the wall behind the jets at the top of the bed as well.

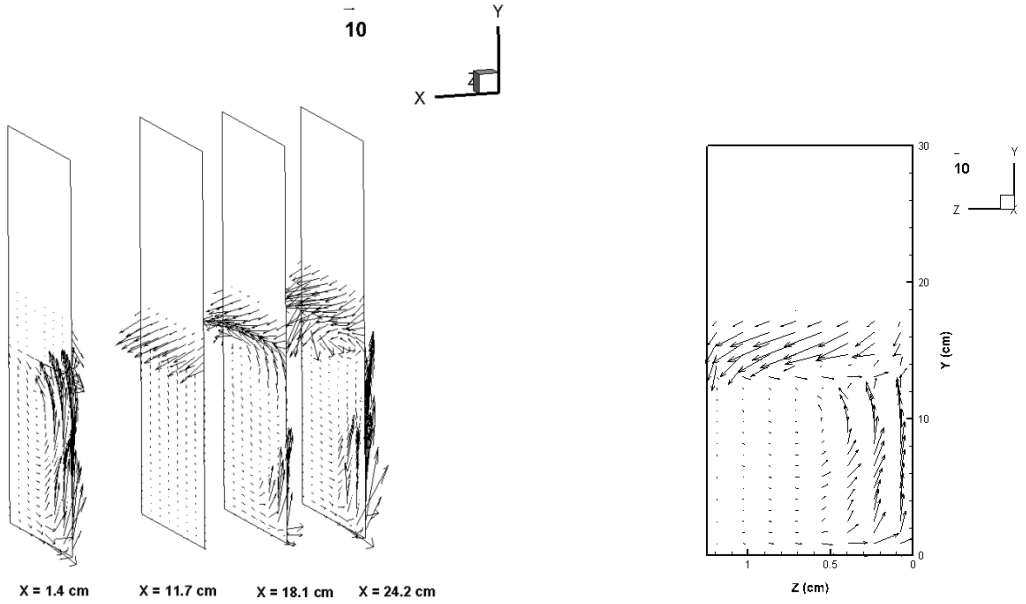

(a) YZ planes at different points along the bed width (b) Side view

Figure 5.16. Solids velocity vectors for the3D simulation of the 5-hole distributor at (a) different YZ planes along the bed width and (b) for a side-view through the bed

Both distributor plates also show that there are regions of the bed, especially close to the walls, where the solids are not moving at all. This is more evident for the 5-holed distributor than the 9-holed distributor. These regions indicate the deadzones or regions where fluidization does not occur. Deadzones do not contribute to the pressure drop. The deadzone mass can be determined from the pressure drop after calculating the fluidizing mass from the latter. The fluidizing mass is subtracted from the total mass in the bed to determine the deadzone mass. Deadzone mass is plotted for the 2D and 3D grid resolutions for the 9-holed distributor in Figure 5.17(a-b), and for the 2D and 3D fine grid for the 5-holed distributor in Figure 5.18.

The inverse relationship of the deadzone mass with pressure drop is clearly evident by comparing Figure 5.17 with pressure drop comparisons in Figure 5.2. The experiments show decreasing deadzone mass with increasing inlet gas velocity. Once the bed is fluidized at 20 cm/s, the rate at which the amount of deadzone mass reduces. The 2D simulations under-predict the deadzone mass, and the 3D simulations give better predictions of deadzone mass once the bed fluidizes in comparison with the experiments. The 3D simulations give better predictions for deadzone mass than the 2D simulations, with the 3D fine grid performing the best.

For the 5-holed distributor shown in Figure 5.18, the experiments linearly decrease until the point of fluidization after which the deadzone mass remains constant. Both 2D and 3D simulations under-predict the deadzone mass until fluidization is attained. Subsequently, 2D simulations predict the trend in which deadzone mass decreases, while the 3D simulations predict increasing deadzone mass in comparison with the experiments.

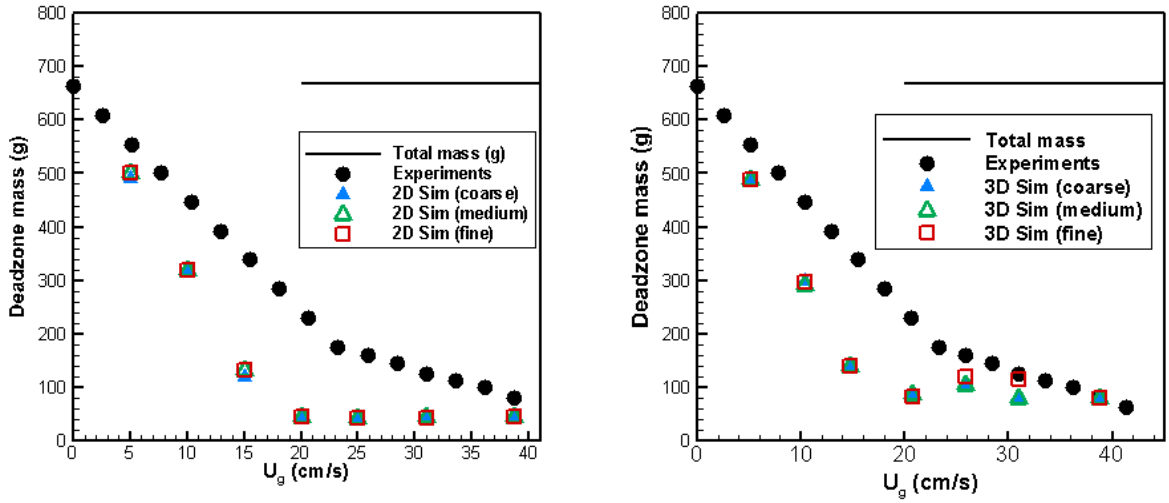

(a) 2D simulations (b) 3D simulations

Figure 5.17. Deadzone mass vs. inlet gas velocity comparing different grid resolutions for both (a) 2D and (b) 3D simulations for the 9-hole distributor

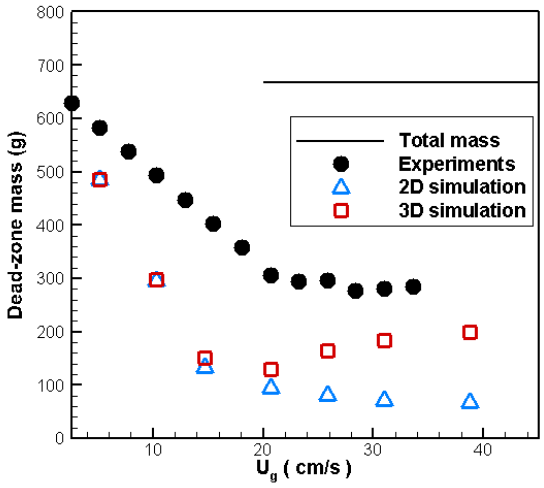

Figure 5.18. Deadzone mass vs. inlet gas velocity comparing experiments, 2D and 3D simulations for the 5-hole distributor

5.3.3.1. *Deadzone distribution*

To further enhance the understanding of the deadzone distribution for each distributor plate, regions of deadzone mass are identified using time-averaged gas volume fraction isocontours. The lowest gas-volume isocontour indicates the regions where there are more solids than gas. The isocontours are plotted for both distributor plate simulations to reveal how the deadzones are distributed, shown in Figure 5.19. For the 5-hole distributor plate, the deadzone regions are larger than the regions shown for the 9-hole distributor plate. For both distributor plates, the jets penetrate almost halfway into the depth of the bed. However the heights of the deadzones formed between the jets are different for each distributor. The Coanda effect can be clearly observed near the walls; examining the particle distribution, there is an absence of solid particles as the jets attach to the wall.

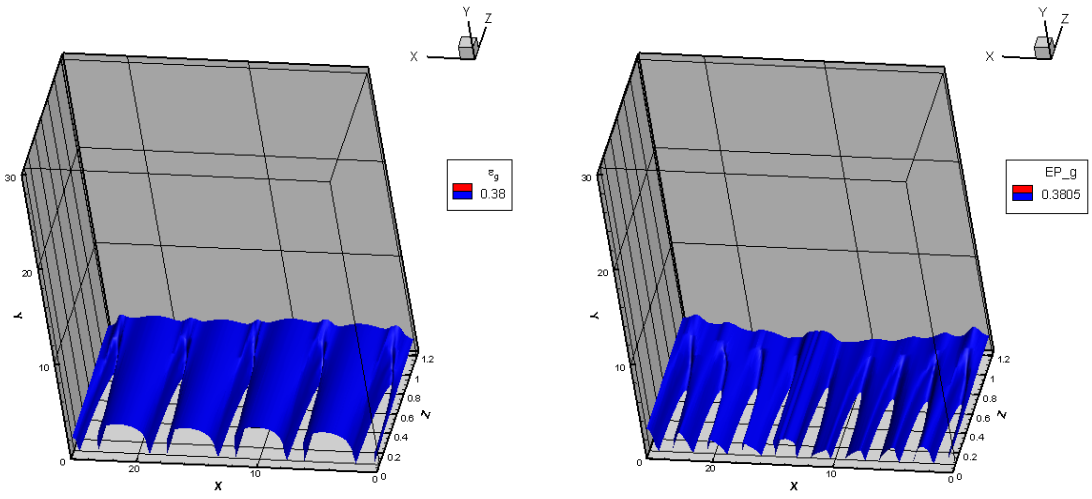

(a) Z = 0.5 cm (b) Z = 1 cm

Figure 5.19. Distribution of deadzones for 5-holed distributor and 9-holed distributor

5.4. Summary

Simulations were performed for a quasi-2D bed with a 9-hole and 5-hole distributor plate configuration in both 2D and 3D simulations. Pressure drop, solids volume fraction contours, and profiles and solids velocity vectors were compared between simulations and experiments. It was found that 3D simulations are necessary to model the discrete jets with more accuracy. Deadzone mass, which represents non-fluidizing solids, was also analyzed. Further research into the effects of turbulence quantities may offer additional insight into improving accuracy of the modeling predictions.

Chapter 6. Coal-biomass fluidization

6.1. Introduction

Coal-biomass fluidized beds are investigated by making use of adjusted mass models that were presented in Chapter 4. The adjusted mass models are used to study fluidized beds for single solids phases of coal and biomass materials (switchgrass, poplar wood, and cornstover) and binary mixtures of switchgrass-coal, poplar wood-coal and cornstover-coal. The analysis includes pressure drop, bed expansion heights, and volume fractions.

6.2. Experimental Setup

The fluidized bed reactor used in the experiments[3] is made from borosilicate glass and equipped with a 100-μm frit gas distributor. The reactor has a 5.08 cm inner diameter and 30 cm height. At the top of the reactor column, an expanding freeboard zone is provided to reduce particle entrainment. Nitrogen gas is fed into the reactor through the distributor plate and the reactor discharges the gas to the atmosphere.

The initial height of the bed is recorded. Following this step, nitrogen is injected below the distributor plate incrementally from zero and progressively at a rate of 33 cm^3/s to 233 cm^3/s, which corresponds to 11.5 cm/s, using an Aalborg mass flow controller (Model GFC 37, Orangeburg, New York,) with a range of 0-500 cm^3/s and accuracy ±1.5%. The pressure drop is measured with a distilled water filled manometer (accuracy of ±0.25) and is recorded when the bed reaches a stable state at each flow rate. The bed heights are recorded and visual observations are made.

6.3. Simulation description

To model and simulate the experiments a two-dimensional (2D) domain in Cartesian coordinates is modeled to represent the centerplane of the cylindrical geometry of the experimental setup. The computational domain used is shown in Figure 5.1. Uniform inlet velocity is specified as the distributor plate and ambient conditions at the outlet. The no-slip wall boundary condition is specified for the gas phase and a partial-slip wall boundary condition for the solids phase. The 2D rectangular grid consisted of 40×200 cells distributed uniformly with cell sizes of 0.12 cm and

[3] The experimental data was provided courtesy of Dr. Foster Agblevor and Guevara Che Nyendu, USTAR Bioenergy Center, Biological Engineering Department, Utah State University.

0.15 cm along the horizontal and vertical directions respectively. The numerical uncertainty due to discretization is estimated by analyzing the grid convergence index (GCI).

6.4. Single solids fluidized beds

The fluidization behavior of single solids fluidized beds of coal and different biomass materials such as switchgrass, poplar wood and cornstover were investigated and the results will be discussed. The properties of the materials used in the single solids model are shown in Table 6.1. The adjusted mass model which made use of the mass that was contributing to the pressure drop was used. The images of the biomass samples used are shown in Figure 6.2.

Table 6.1. Modeling parameters used for single solids fluidized bed

Properties	Coal		Switchgrass		Poplar wood		Cornstover	
	Exp	Sim	Exp	Sim	Exp	Sim	Exp	Sim
d_p(μm)	62	62	145	145	153	153	418	418
ψ(-)	1	1	1	1	1	1	1	1
ρ_s (g/cm^3)	1.38	1.38	1.1	1.1	1.12	1.12	1.21	1.21
m(g)	30	*12.4*	30	*16.9*	30	*13.2*	30	*24.3*
ρ_b (g/cm^3)	0.50	0.36	0.19	0.57	0.16	0.38	0.21	0.85
ε_g(-)	0.64	*0.74*	0.83	*0.48*	0.86	*0.66*	0.83	*0.30*
h_o(cm)	3	*1.25*	7.05	*1.45*	7	*1.7*	6	*1.41*

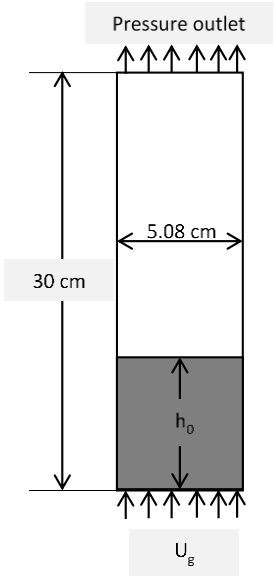

Figure 6.1. Schematic of the computational domain

Switchgrass **Poplar wood** **Cornstover**

Figure 6.2. Images of biomass samples used in the fluidized bed reactor (Images courtesy of the Biological Engineering Department at Utah State University)

6.4.1.1. *Pressure drop*

The pressure drop across the bed for varying inlet velocities is analyzed for different single solids materials comprising coal, and biomass solids such as switchgrass, poplar wood, and cornstover, respectively, in Figure 6.3. Pressure drop measured by the experiments are indicated by red circles, with the simulations predictions depicted by open triangles.

In Figure 6.3, experiments shows that coal fluidization occurs at U_{mf} = 3.2 cm/s. There is the characteristic spike around the point of fluidization as is expected for Geldart A particles, followed by a constant pressure drop of about 78 Pa when the bed is fully fluidized. The simulations for coal particles under-predict U_{mf} but predict a constant pressure drop similar to the experiments. For switchgrass, experiments indicate a fairly constant pressure drop after fluidizing at U_{mf} = 2 cm/s. The simulations predict the spike in pressure drop as is expected for Geldart A particle around the fluidization point and then remains constant. Pressure drop for different inlet velocities for poplar wood is also shown in Figure 6.3. The experiments indicate fluidization around 4.4 cm/s followed by a constant pressure drop of 65 Pa. Simulations accurately capture the trends observed in the experiments for poplar wood. Pressure drop for varying inlet velocities for cornstover is compared between experiments and simulations. Experiments show the bed fluidizing at U_{mf} = 4.9 cm/s. Just as in coal, there is the spike observed immediately around minimum fluidization followed by a constant pressure drop of 118 Pa. The simulations capture the U_{mf} and predict the trend of constant pressure drop just as is seen in the experiments.

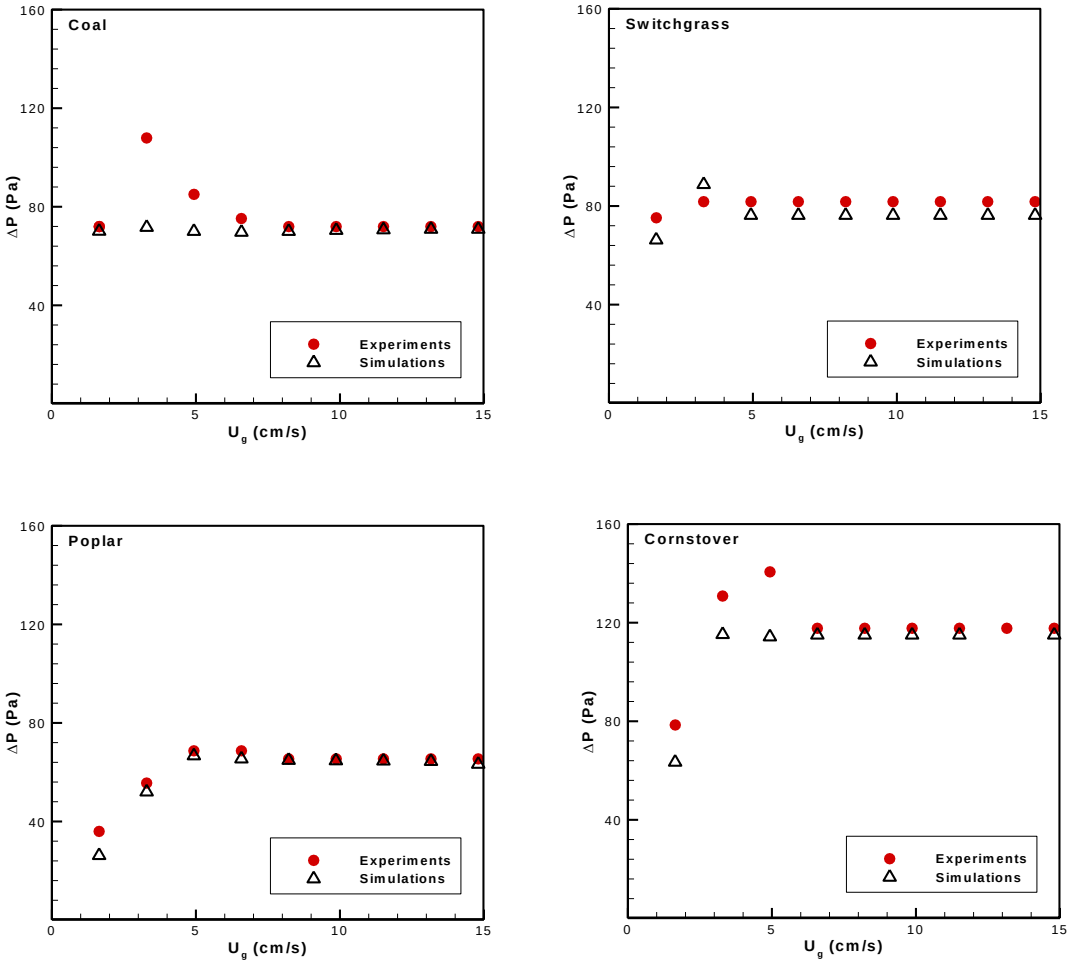

Figure 6.3. Comparison of pressure drop between experiments and simulations for single solids

Pressure drop and minimum fluidization velocity measured in the experiments and predictions are summarized in Figure 6.4.The horizontal axis represents different materials, with the left and right vertical axes representing pressure drop and U_{mf}, respectively. The filled symbols indicate experimental measurements, and the hollow symbols show simulation predictions. Amongst all materials, switchgrass has the lowest U_{mf}, followed by coal, poplar wood, and cornstover in the increasing order. For the biomass materials, the lowest pressure drop is observed for poplar wood, and the highest was for cornstover. Simulations slightly over-predict the pressure drop for coal, while slightly under-predict the pressure drop for biomass materials. Overall, the simulations compare well with the experimental measurements for different materials.

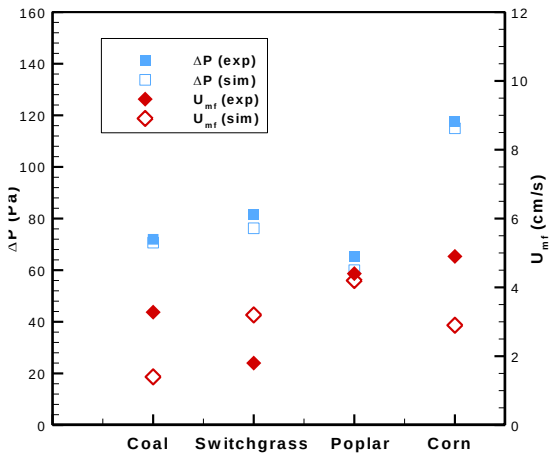

Figure 6.4. Pressure drop and minimum fluidization velocity for coal and biomass materials

6.4.1.2. *Bed expansion heights*

Bed expansion heights normalized with the initial bed height for material used in the mixtures are analyzed for varying inlet gas velocities in Figure 6.5. The red circular symbols indicate the experimental measurements for normalized bed height, while the hollow triangles indicate the simulation predictions.

For all materials, with increasing inlet velocity, the normalized bed height also increases in the experiments. The same trend is captured by the simulations. For coal, the rate of increasing bed height is different after U_{mf}. The simulations over-predict the bed expansion height for coal after the point of fluidization. For switchgrass the experiments show the bed expansion height rapidly rising after 10 cm/s. The simulations predict a linearly increasing bed expansion height for switchgrass. For poplar wood, the experiments indicate a linearly increasing bed expansion height, with the simulations also showing similar trend. The simulation compare well with the experiments prior to U_{mf} of 4.4 cm/s, after which the bed expansion height is over-predicted. The rate of increase of bed height was steeper for the simulations when compared with the experiments. For cornstover, the simulations the bed expansion remained almost constant. The simulations match very well with the experiments, giving very close bed expansion heights. Overall, coal particles has the highest bed expansion of all materials. Among the biomass materials, poplar wood has the highest bed expansion height.

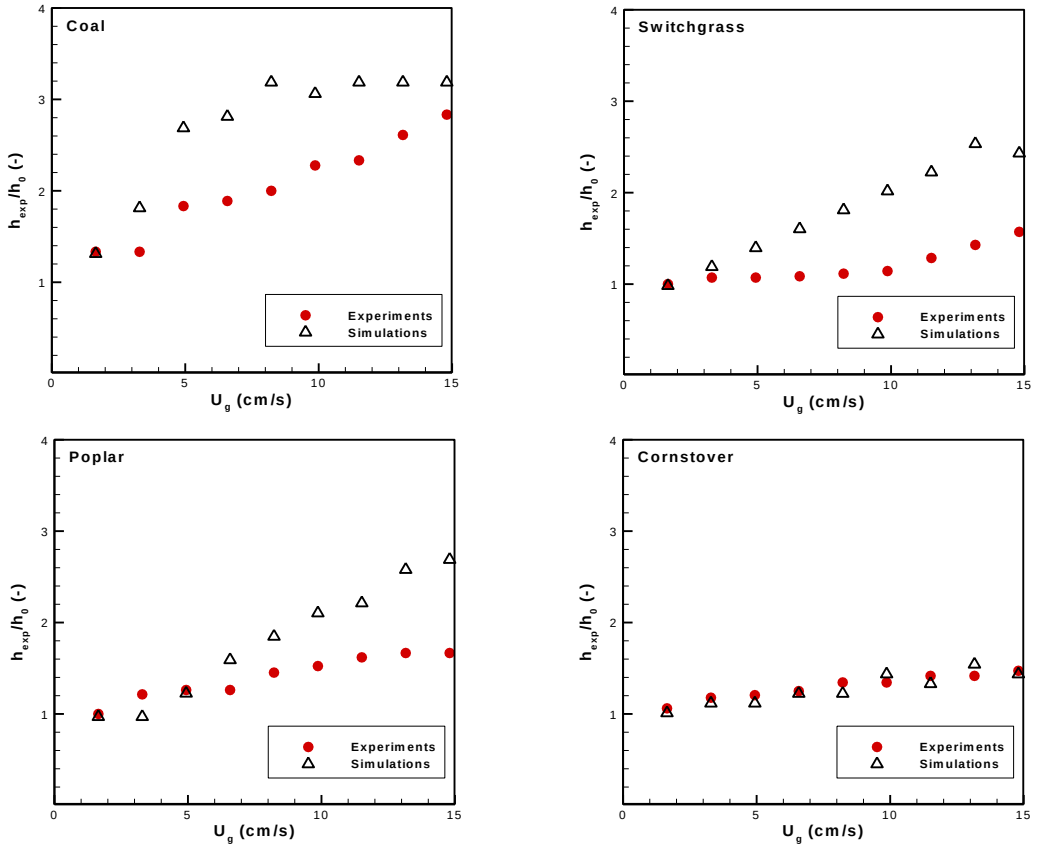

Figure 6.5. Comparison of normalized bed expansion heights predictions between experiments and single solids and binary mixture models of simulations for switchgrass-coal binary mixtures

6.4.1.3. *Solids volume fraction contours*

Time-averaged solids volume fraction contours are analyzed for the single solids simulations of different fluidized bed materials. Figure 6.6 presents solids volume fraction contours time-averaged from 5 to 20s for the inlet velocity at 2 U_{mf} at a sampling rate of 100 Hz. Figure 6.6(a-d) presents the time averaged solids volume fraction obtained for coal, switchgrass, poplar wood and cornstover, respectively. The legends indicate the maximum and minimum solids volume fraction for each material.

For coal, the simulation indicated fairly uniform distribution of solids throughout the domain, with slight concentration of coal near the bottom of the bed and the right wall. The solids volume fraction contours for switchgrass indicate a symmetrical distribution of the material about the vertical centerline of the bed. A majority of the solids particles are distributed throughout the bed. A similar symmetrical distribution is observed for the poplar wood with particles observed circulating along the walls and the central portion of the bed. For cornstover, a uniform distribution

of solids that was symmetrical about the vertical-center line was observed. However cornstover, being a difficult material to fluidize, doesn't show significant circulation.

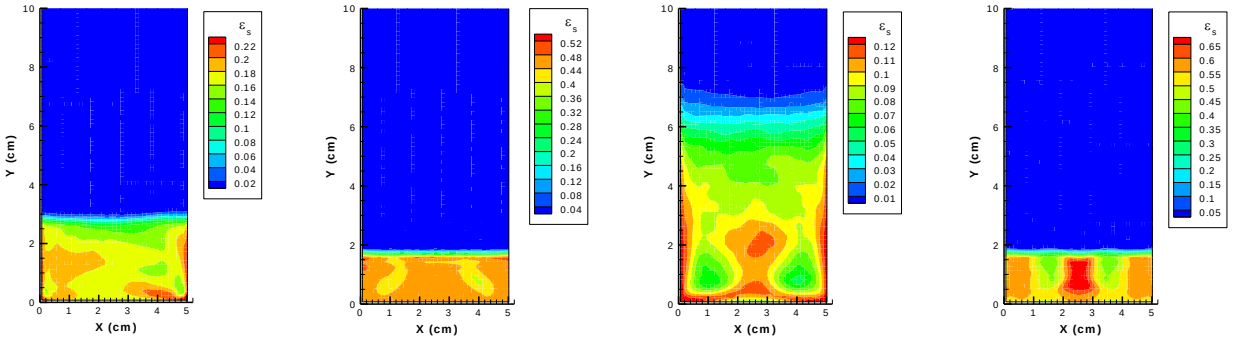

(a) Coal **(b) Switchgrass** **(c) Poplar wood** **(d) Cornstover**

Figure 6.6. Time averaged solids volume fraction contours at U_g/U_{mf} = 2 for different materials

6.5. Coal-biomass binary mixtures

6.5.1. *Switchgrass-coal binary mixture*

This section will present the investigation of fluidization behavior of binary mixture fluidized bed containing switchgrass-coal binary mixture. Pressure drop, bed expansion heights, and solids volume fraction will be analyzed.

6.5.1.1. *Pressure drop*

Pressure drop measured in the experiments is compared with predictions made using two approaches to model switchgrass-coal binary mixtures. The first model uses a characteristic particle diameter and particle density to represent the two materials as a single solids phase. The second model uses two solids phases to represent the materials within the binary mixture. The modeling parameters used for the 10:90 mixture are shown in Table 6.2. The modeling parameters used for the remaining mixtures are listed in the Appendix A. In Figure 6.7, the red circular symbols indicate the experiments with the hollow symbols indicating the simulations. The blue triangles represent the single solids model predictions (S), and the green squares indicate the binary mixture model (B).

Table 6.2. Modeling parameters used for switchgrass-coal 10:90 mixture

Properties	Experiments		Sim-S	Sim -B	
	Switchgrass	Coal	Mix. Props.	Switchgrass	Coal
$d_p(\mu m)$	145	62	*67*	145	62
$\psi(-)$	-	-	1	1	1
ρ_s (g/cm^3)	1.1	1.38	1.35	1.1	1.38
m(g)	3	27	*24.3*	*2.4*	*21.9*
ρ_b (g/cm^3)	-	-	0.39	0.04	0.35
X_i (-)	0.1	0.9		0.10	0.90
$\varepsilon_g(-)$	-		*0.71*	*0.71*	
h_0(cm)	3		*3.1*	*3.1*	

For the switchgrass-coal mixture of 10:90, the experiments indicate a linearly increasing pressure drop until the point of fluidization after which the pressure drop remains constant. Both simulation models capture the minimum fluidization velocity, with the single solids model predicting a higher pressure drop with further increasing inlet velocity, and the binary mixture model predicting a lower pressure drop. The 20:80 binary mixture has the lowest minimum fluidization velocity of all the mixtures. Experiments show a constant pressure drop with further increasing velocity. Both models capture the same trend observed for the pressure drop while predicting a slightly higher pressure drop. The binary mixture model predicts a slightly higher U_{mf} in comparison with the experiments, while the single solids model captures U_{mf} fairly accurately. The binary mixture with the 30:70 ratio of switchgrass-coal displays the same trend of linearly increasing pressure drop across the bed until the point of minimum fluidization, followed by a constant pressure drop. Both models capture the same trend observed. However as the velocity further increases, the simulations predict lower pressure drop when U_g = 15 cm/s. Experiments and simulations for the switchgrass-coal binary mixture of 40:60 show a similar trend seen in the experiments, with the single solids model predicting a higher U_{mf}. The binary mixture model however captures both U_{mf} and ΔP fairly close to the experimental values, with the pressure drop being predicted slightly lower than what was observed in the experiments. For the switchgrass-coal binary mixture with the ratio of 50:50 both the models indicate a similar trend observed in the experiments, with the simulations predicting a higher pressure drop in comparison with the experiments.

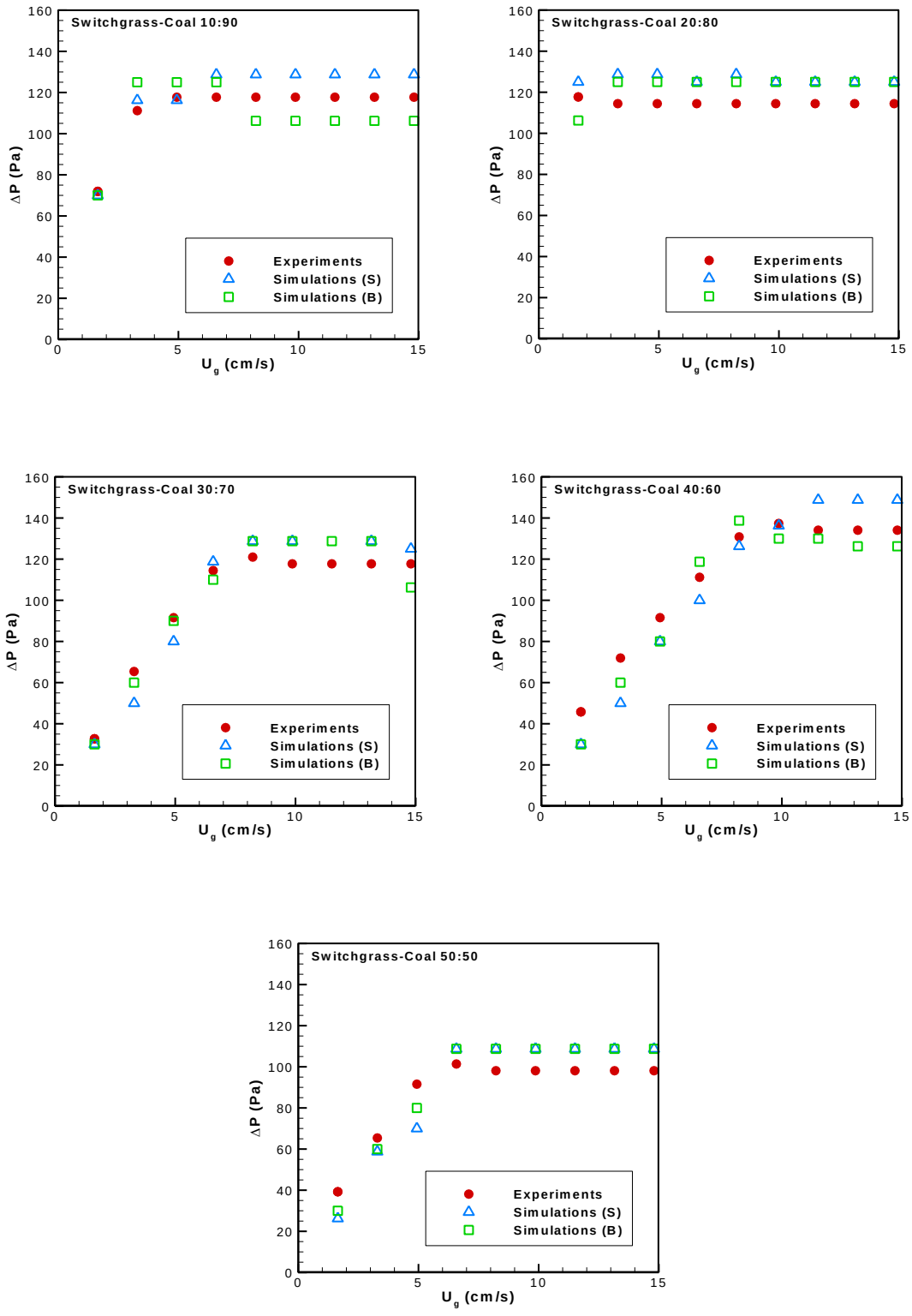

Figure 6.7. Comparison of pressure drop between experiments and simulations for single solids and binary mixture models for switchgrass-coal mixture

Figure 6.8 compares the pressure drop and the minimum fluidization velocity measured in the experiments with the predictions made by the simulations using the binary mixture model. The horizontal axis represents the varying mass ratio of switchgrass, with the left vertical axis representing the pressure drop across the bed and the right vertical axis representing the minimum fluidization velocity. The blue square symbols show the pressure drop predictions, and the red diamond symbols represent U_{mf}. The filled symbols indicate the experimental measurements and the hollow symbols show simulation predictions.

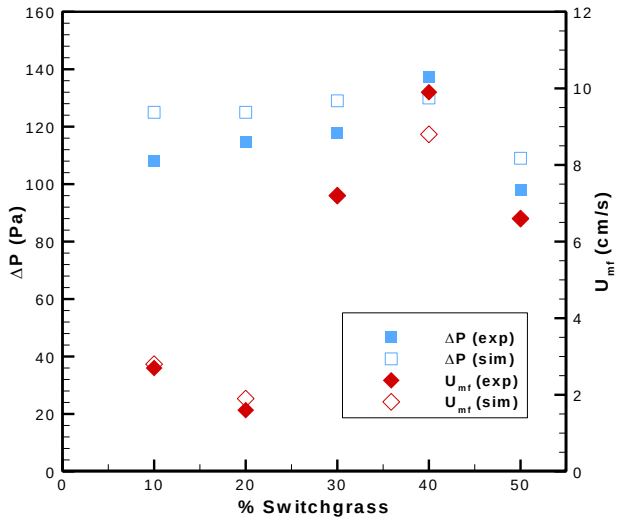

Figure 6.8. Pressure drop and minimum fluidization velocity estimates comparing different binary mixtures of switchgrass and coal

The effect of increasing the mass of switchgrass present in the binary mixture on pressure drop and minimum fluidization velocity can be seen in Figure 6.8. With increasing mass of switchgrass, the pressure drop measured by the experiments increases until switchgrass is equal to 40% of the mass of the entire bed. The simulations over-predict the pressure drop measured experimentally, except when the bed contains 40% switchgrass. The pressure drop then decreases when half the bed contains switchgrass. The reduced pressure drop observed at 50% switchgrass is also captured by the simulations. The sudden reduction in pressure drop at 50% switchgrass in comparison to other switchgrass mixtures suggests the influence of switchgrass in reducing the amount of mass that is fluidizing within the bed.

The trend observed for the minimum fluidization velocity measured by the experiments is different from the one seen for the pressure drop. The minimum fluidization velocity first decreases and then increases to the maximum of about 10 cm/s and then decreases again with the increasing switchgrass mass in the bed. The simulations compare very well with the U_{mf} measured with the experiments. The lowest minimum fluidization velocity is observed for the case of switchgrass-coal mixture in the ratio of 20:80, with the highest U_{mf} being observed for the binary mixture of 40:60.

6.5.1.2. *Bed expansion heights*

Figure 6.9 compares expanded bed heights normalized with the initial bed height for the binary mixtures containing switchgrass and coal for varying inlet gas velocities. The red circular symbols indicate the experimental measurements for normalized bed height, while the hollow symbols indicate the simulation predictions, with the blue triangles representing the single solids model, and the green squares the binary mixture model.

For all the mixtures, with increasing inlet velocity, the normalized expanded bed height also increases. The same trend is captured by the simulations, with both models (S and B) predicting similar bed expansion heights. The simulations compare well with the experiments for binary mixtures containing lower switchgrass content of 10% and 20% of the bed mass, also showing a linear rate of increasing bed expansion. However with increasing switchgrass content, the simulations tend to under-predict bed expansion heights in comparison with the experiments. The experiments indicate nonlinear bed expansion prior to the U_{mf} = 7 cm/s for the 30:70 mixture, followed by a more linear increasing bed expansion. For the 40:60 mixture, the experiments show a steeper rate of increase in bed height past the point of minimum fluidization velocity. Simulations indicate a lower rate of bed expansion prior to the point of minimum fluidization with a slightly higher rate later on, for a lower bed height in comparison with the experiments for the 30:70, 40:60 and 50:50 mixtures. It is also worthy of noting here that the experimental error in bed expansion heights would be higher than the simulations considering the fact that the measurements were obtained using the human eye and a ruler.

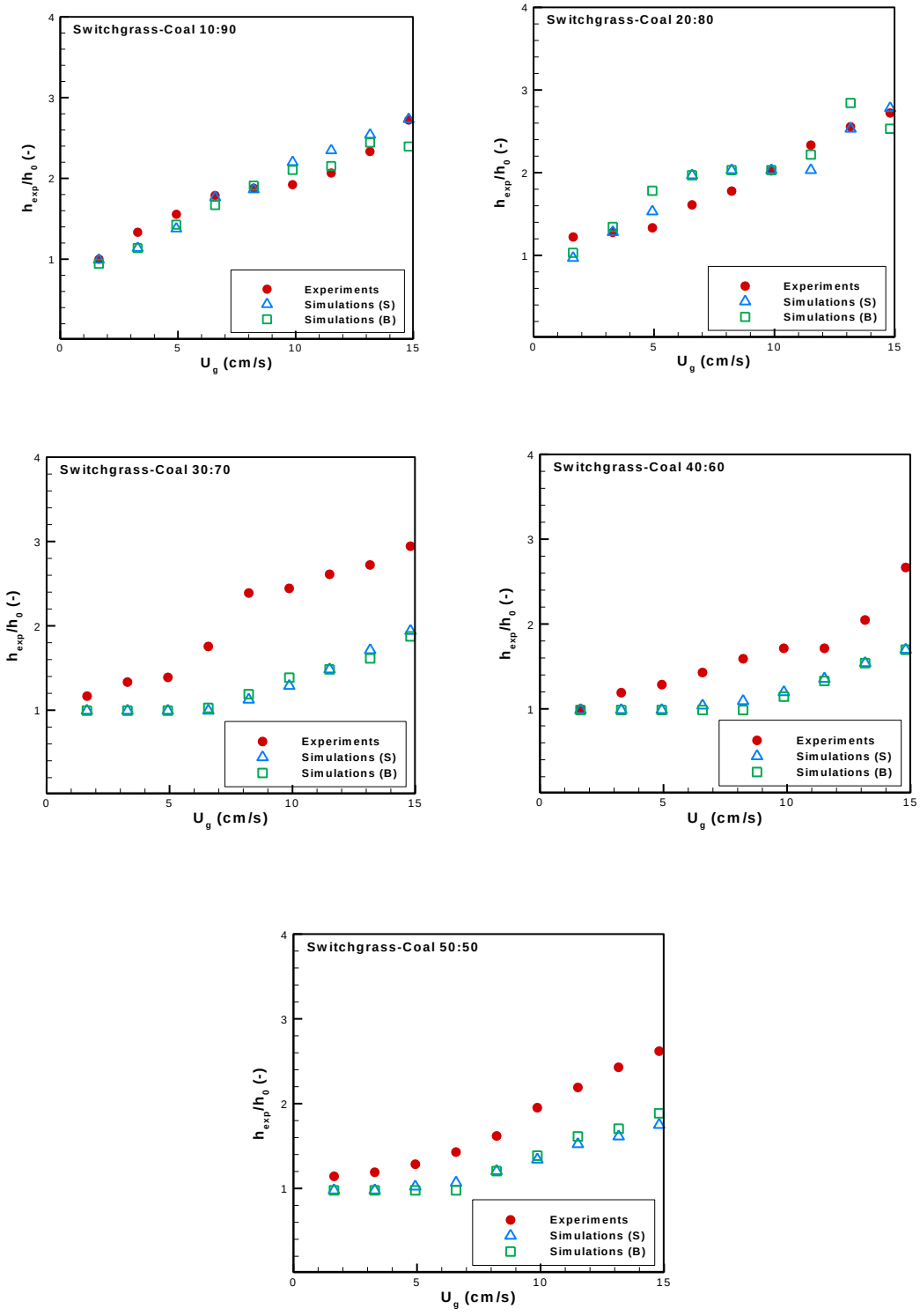

Figure 6.9. Comparison of normalized bed expansion heights predictions between experiments and single solids and binary mixture models of simulations for switchgrass-coal binary mixtures

6.5.1.3. *Solids volume fraction contours*

To analyze the hydrodynamics involved within the binary mixtures, further analysis using the solids volume fraction contours are considered. Figure 6.10 presents solids volume fraction contours time-averaged from 5 to 20s for the inlet velocity at 2 U_{mf} at a sampling rate of 100 Hz. From left to right for each column, the total solids volume fractions are presented for the single solids model, binary mixture model, and then the switchgrass and coal volume fractions predicted using the binary mixture model.

For the 10:90 binary mixture, the single solids model and binary mixture model presents a uniform distribution about the vertical centerline of the bed, with symmetrical distribution observed for the binary mixture model. Switchgrass volume fraction contour shows that switchgrass is mainly concentrated near the bottom of the bed. The hydrodynamics of the bed modeled using the binary mixture model is dominated by coal.

For the 20:80 mixture, the single solids model indicates a uniformly distributed bed, with the binary mixture model indicating more solids concentrated near the bottom of the bed. Analyzing the individual components contribution to the solids volume fraction indicates that switchgrass is mixing more within the lower portion of the bed. However the majority of the solids volume fraction contribution is still from coal for this mixture. A possible reason is that this is the optimum condition where coal dominates the hydrodynamics but switchgrass also contributes to the overall hydrodynamics.

For the 30:70 mixture, the time averaged total solids volume fraction predicted by the single solids model and the binary mixture model are fairly identical, with a symmetrical distribution of solids. The binary mixture model indicates a slightly higher bed expansion in comparison to the single solids model. The development of symmetrical pockets of air close to the bottom of the bed can be clearly seen upon investigating the individual solids volume fraction contours. With 30% of the mass present being switchgrass, the increasing influence of switchgrass on the hydrodynamics can also be seen. The higher bed expansion observed for the binary mixture also seems to indicate that coal particles expand farther than the switchgrass particles.

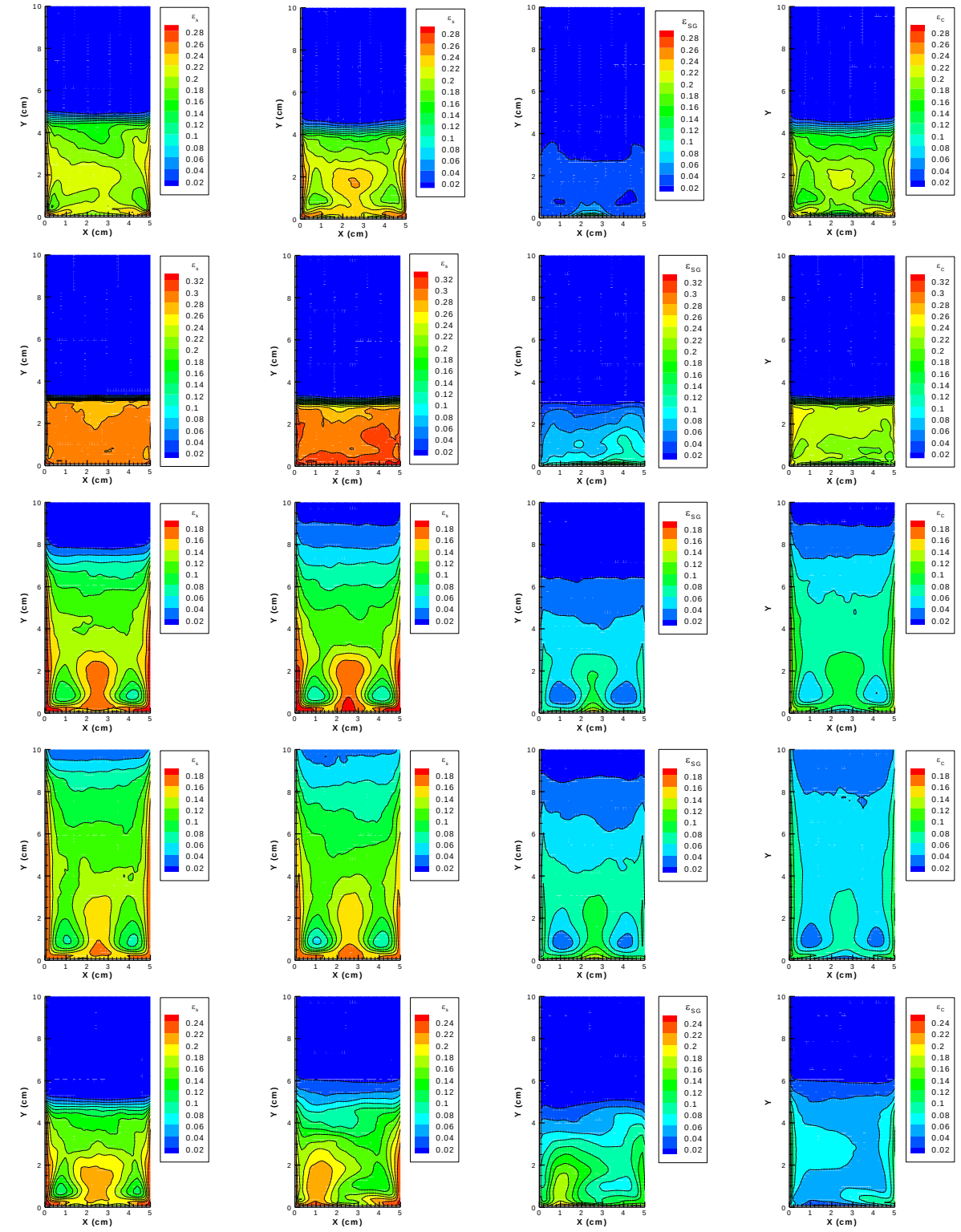

(a) Total solids volume fraction (S) (b) Total solids volume fraction (B) (c) Switchgrass volume fraction (d) Coal volume fraction

Figure 6.10. Time averaged solids volume fraction contours at U_g/U_{mf} = 2. (a) Total solids volume fraction using the single solids model, (b) total solids volume fraction using the binary mixture model, (c) switchgrass volume fraction and (d) coal volume fraction. Top row to bottom row are mixture ratios of 10:90, 20:80, 30:70, 40:60 and 50:50, respectively

For the 40:60 mixture, the time averaged solids volume fraction contours are very similar for both single solids and binary mixture models. The pockets of air observed in the 30:70 mixture can also be seen for this case as well. Both switchgrass and coal are contributing to the overall hydrodynamics but the bed material is not uniformly distributed.

The 50:50 binary mixture clearly indicates how further increasing the switchgrass affects the hydrodynamics. The single solids model predicts a symmetric distribution, but the binary mixture model is asymmetric. Further analysis of the individual solids volume fraction contours indicates the increasing influence of switchgrass within the bed contributing to the asymmetrical distribution observed. The higher bed expansion height observed for the binary mixture particles seems to be due to the coal particles.

Figure 6.11 represents instantaneous volume fraction contours for the models obtained at 5 s, 10 s, 15 s and 20 s during the fluidization of the 40:60 poplar wood-coal binary mixture at $U_g = 2U_{mf}$. The void fraction from the single solids model shows that the bed is fairly well mixed quickly in time with less bubbles in the bed. The void fraction from the binary mixture model shows the distribution of solids becoming more uniform within the bed over time. Analyzing the switchgrass volume fraction, the increasing influence of switchgrass over the bed can be seen, with the switchgrass initially concentrated at the bottom of the bed and subsequently being redistributed to other regions of the bed. The coal particles are initially dominant in the top half of the bed. When the switchgrass begins to mix with coal over time, the coal particles are redistributed fairly uniformly through the entire bed. Thus the switchgrass and coal are synergistically ensuring proper distribution of solids during fluidization. Proper distribution of coal particles is important to ensure proper chemical reactions during gasification.

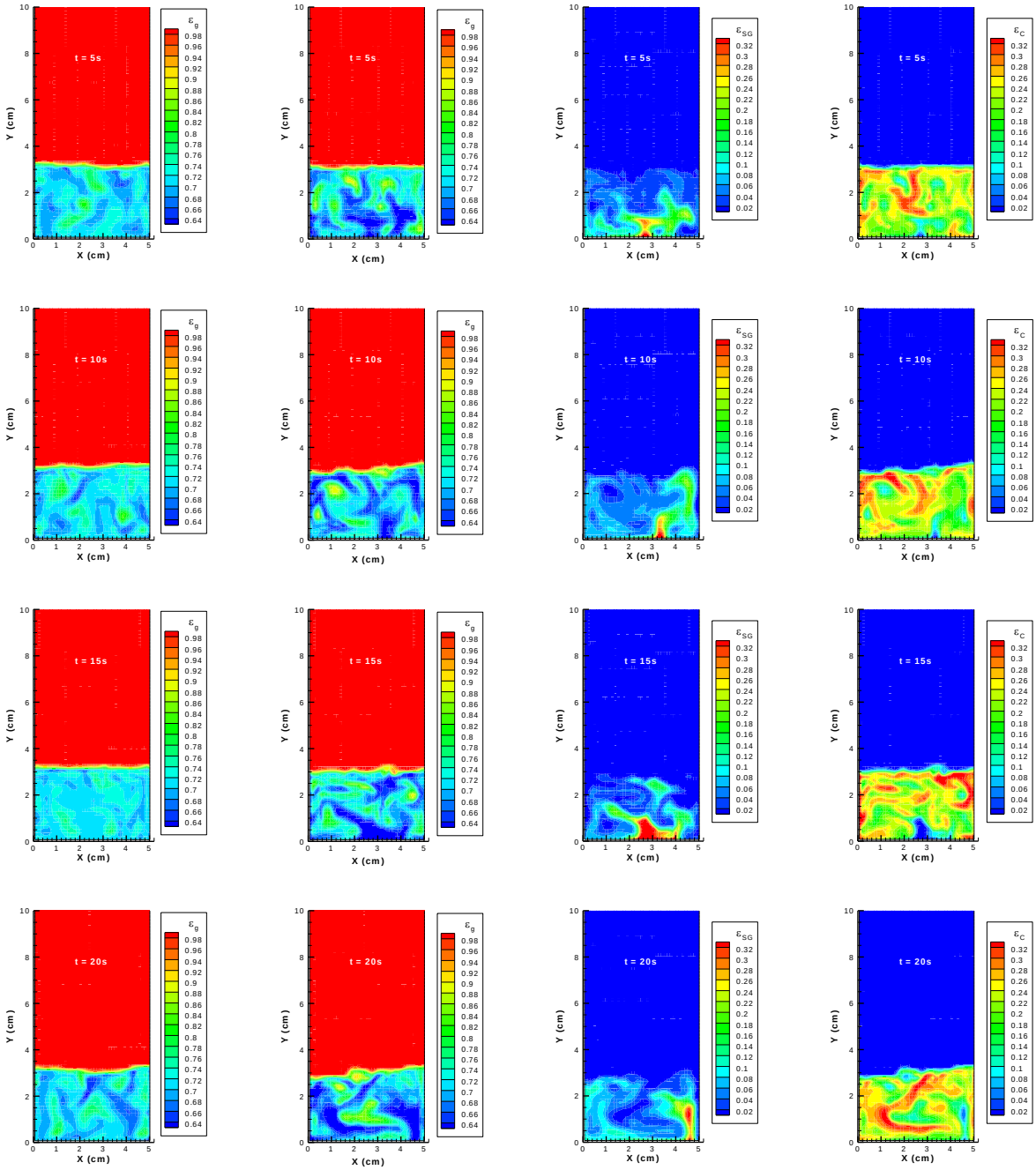

Figure 6.11. Instantaneous volume fraction contours at U_g/U_{mf} = 2 for the mixture ratio of 20:80. (a) Total gas volume fraction using the single solids model, (b) total gas volume fraction using the binary mixture model, (c) switchgrass volume fraction and (d) coal volume fraction. Top row to bottom row are at the instants of 5s, 10s, 15s, and 20s respectively

6.5.2. *Poplar wood-Coal Binary Mixture*

6.5.2.1. *Pressure drop*

Pressure drop measured in the experiments is compared with predictions made using the single and binary models for poplar wood-coal mixtures, in Figure 6.13. The modeling parameters used for the 10:90 poplar wood-coal mixture are shown in Table 6.3. The modeling parameters used for the remaining mixtures are listed in the Appendix A. For the poplar wood-coal mixture of 10:90, the experiments indicate a linearly increasing pressure drop until the point of fluidization at U_{mf} = 3.3 cm/s after which the pressure drop remains constant at 79 Pa. Both simulation models capture the minimum fluidization velocity, with both models predicting pressure drop slightly higher than the experiments.

The 20:80 poplar wood-coal binary mixture shows an interesting fluidization trend in the experimental measurements. Pressure drop rises sharply to the point of fluidization at U_{mf} = 4.9 cm/s. With further increasing velocity, pressure drop remains constant until around $U_g = 2\ U_{mf}$, and then decreases with increasing inlet velocity. Both simulation models predict U_{mf} fairly accurately. The simulations predict constant pressure drop subsequent to fluidization, unlike the experiments. It is possible that the higher pressure drop observed in the experiments indicates that the majority of the bed mass is fluidizing once fluidization has been attained. With further increasing gas velocity, the bed mass contributing to fluidization decreases possibly due to elutriation.

The binary mixture with the 30:70 ratio of poplar wood-coal displays the trend of linearly increasing pressure drop across the bed until the point of minimum fluidization of U_{mf} = 4.9 cm/s, followed by constant pressure drop. Both models capture the same trend observed, with the binary mixture model predicting a slightly higher U_{mf} than the single solids model. Experiments and simulations for the poplar wood-coal binary mixture of 40:60 show a similar trend, with the binary mixture model predicting a higher U_{mf} than the single solids model. Both simulation models capture the pressure drop after fluidization fairly accurately.

For the poplar wood-coal binary mixture with the ratio of 50:50 both the models indicate a similar trend observed in the experiments. The binary mixture model captures the U_{mf} and pressure drop with more accuracy than the single solids model, with the latter predicting a lower pressure drop when compared with the experimental measurements.

Table 6.3. Modeling parameters used for poplar wood-coal 10:90 mixture

Properties	Experiments		Sim-S	Sim -B	
	Poplar wood	Coal	Mix. Props.	Poplar wood	Coal
d_p(μm)	153	62	*67*	153	62
ψ(-)	-	-	1	1	1
ρ_s (g/cm^3)	1.12	1.38	1.35	1.12	1.38
m(g)	3	27	*16.2*	*1.6*	*14.6*
ρ_b (g/cm^3)	-	-	0.36	0.04	0.32
X_i (-)	0.1	0.9		0.1	0.9
ε_g(-)			*0.74*	*0.74*	
h_0(cm)	3		*2.2*	*2.2*	

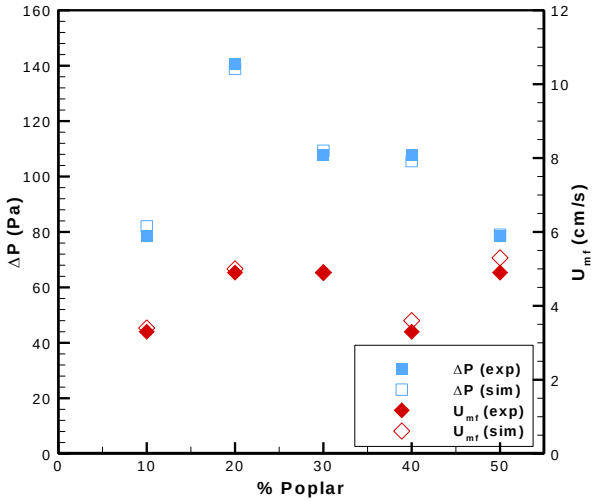

Figure 6.12. Pressure drop and minimum fluidization velocity estimates comparing different binary mixtures of poplar wood and coal

Figure 6.13 summarizes the pressure drop and the minimum fluidization velocity measured in the experiments along with simulation predictions for the different poplar wood-coal binary mixtures. The horizontal axis represents the varying mass ratio of switchgrass, with the left vertical axis representing the pressure drop across the bed and the right vertical axis representing the minimum fluidization velocity. The blue square symbols show the pressure drop predictions, and the red diamond symbols represent U_{mf}. The filled symbols indicate the experimental measurements and the hollow symbols show simulation predictions.

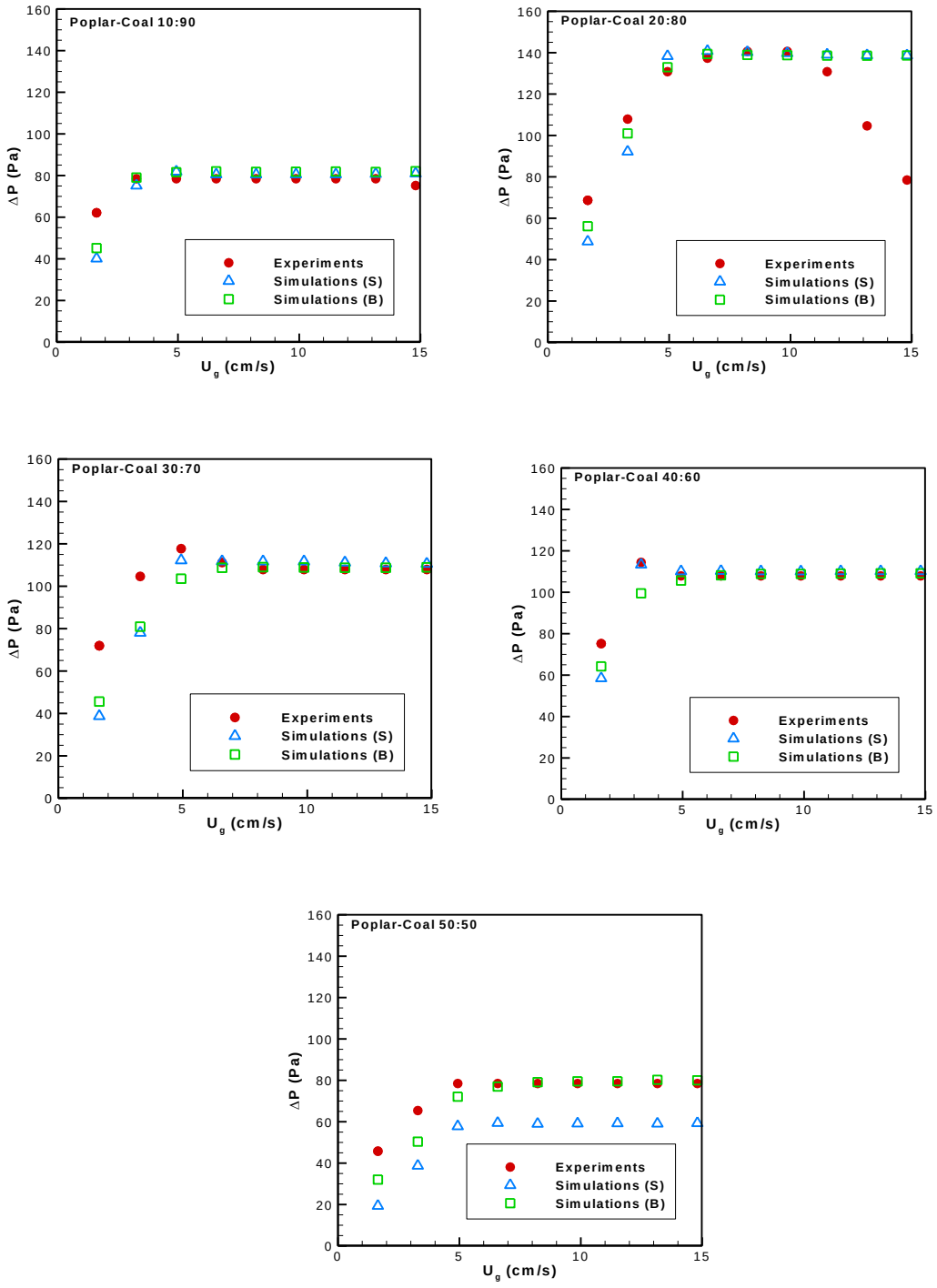

Figure 6.13. Comparison of pressure drop between experiments and simulations for single solids and binary mixture models for poplar wood-coal mixtures

With the increasing mass of poplar wood present in the bed, the pressure drop of the bed after fluidization increases first when the mass percent of switchgrass is 20 percent the mass of the entire bed and then decreases subsequently. The simulations accurately capture the pressure drop observed. The decreasing pressure drop is possibly indicating how with further increase of poplar wood in the bed, the bed mass that is fluidizing is decreasing. This shows how beyond a certain point, biomass doesn't contribute to the fluidization.

For the minimum fluidization velocity, experiments show the U_{mf} slightly increasing with increasing poplar wood until bed contains 40 percent poplar wood. The U_{mf} then increases back to about 4.9 cm/s when bed contains equal amount of poplar wood and coal. Simulations capture the U_{mf} measured fairly accurately. Coal has a lower U_{mf} of about 1.4 cm/s than poplar wood which is about 4.9 cm/s. So as you increase in the poplar wood content in the bed, the slightly increasing value of U_{mf} observed for the mixture makes sense.

6.5.2.2. *Bed expansion heights*

Figure 6.14 compares expanded bed heights normalized with the initial bed height for the binary mixtures containing poplar wood and coal for varying inlet gas velocities. For all the mixtures, with increasing inlet velocity, the normalized expanded bed height also increases. The same trend is captured by the simulations, with both models predicting similar bed expansion heights. When poplar wood is 10 percent the bed mass, there is a non-linear rate of increasing bed expansion until 7 cm/s, followed by a steady rate of increasing bed expansion height. Both simulation models for the 10 percent poplar wood mixture predict a lower bed height compared to the experiments although the trends are similar. For the 20:80 mixture, the bed expansion increases and at 10 cm/s, which is about 2 Umf, there is a sudden increase in bed expansion as is captured by the experiments. Both simulation models indicate a linearly increasing rate of bed expansion, while under-predicting bed expansion heights.

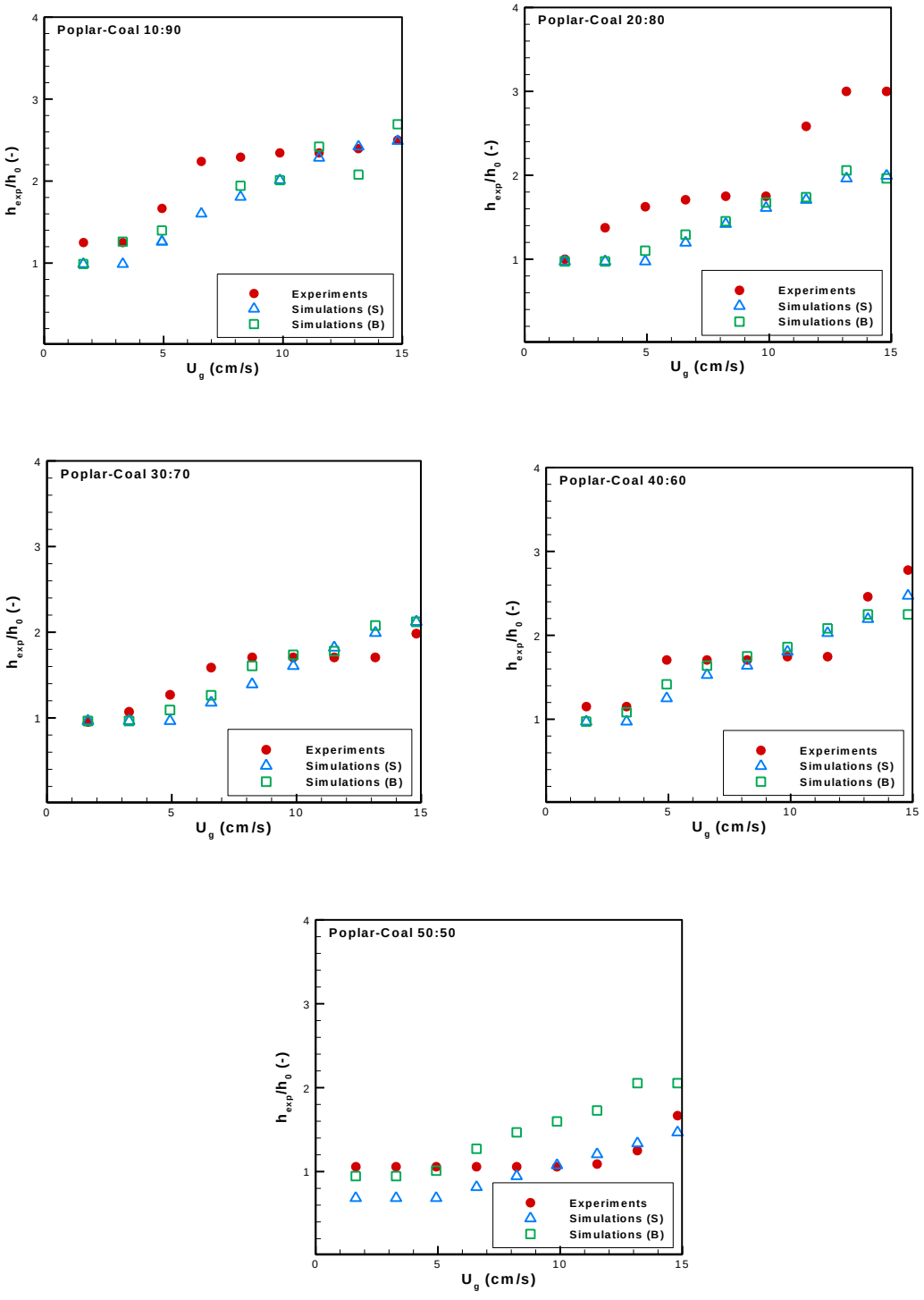

Figure 6.14. Comparison of normalized bed expansion heights predictions between experiments and single solids and binary mixture models of simulations for poplar wood-coal binary mixtures

For the 30:70 and 40:60 poplar wood-coal mixture, the bed expansion heights slightly increase with increase in velocity until around the point of minimum fluidization velocity 3.3 cm/s, followed by a fairly constant bed expansion height. The simulation predicts linearly increasing bed expansion heights. For the 50:50 poplar wood-coal binary mixture, the bed expansion heights increases at a slower rate until about Ug = 13 cm/s, followed by which it increases at a higher rate. The single solids model seems to be more accurate than the binary mixture model in capturing the bed heights observed, with the binary mixture model predicting higher bed expansion heights.

6.5.2.3. *Solids volume fraction contours*

For further analysis of the hydrodynamics involved, time-averaged solids volume fraction contours are considered Figure 6.15 presents solids volume fraction contours time-averaged from 5 to 20s for the inlet velocity at 2 U_{mf} at a sampling rate of 100 Hz. From the left to right, for each row, the total solids volume fraction are presented for the single solids model, binary mixture model, and then the switchgrass and coal volume fractions predicted using the binary mixture model.

For the 20:80 mixture, the simulations indicates a fairly symmetrically distributed bed, with both the single solids and binary mixture model indicating more solids concentrated near the bottom of the bed. Analyzing the individual components contribution to the solids volume fraction indicates that poplar wood is mixing more within the lower portion of the bed. However the majority of the solids volume fraction contribution is still from coal for this mixture. The bed expansion observed for the mixture is primarily due to the coal particles than poplar wood.

For the 30:70 mixture, the time averaged total solids volume fraction predicted by the single solids model and the binary mixture model are identical, with a symmetrical distribution of solid particles on either side of the vertical line. The development of symmetrical pockets of air about the centerline closer to the bottom of the bed can be clearly seen upon investigating the individual solids volume fraction contours. With 30% of the mass present being poplar wood, the increasing influence of poplar wood on the hydrodynamics can also be seen in the binary mixture solids volume fraction contour. The bed expansion observed for the binary mixture seems to indicate that coal particles expand farther than the poplar wood particles.

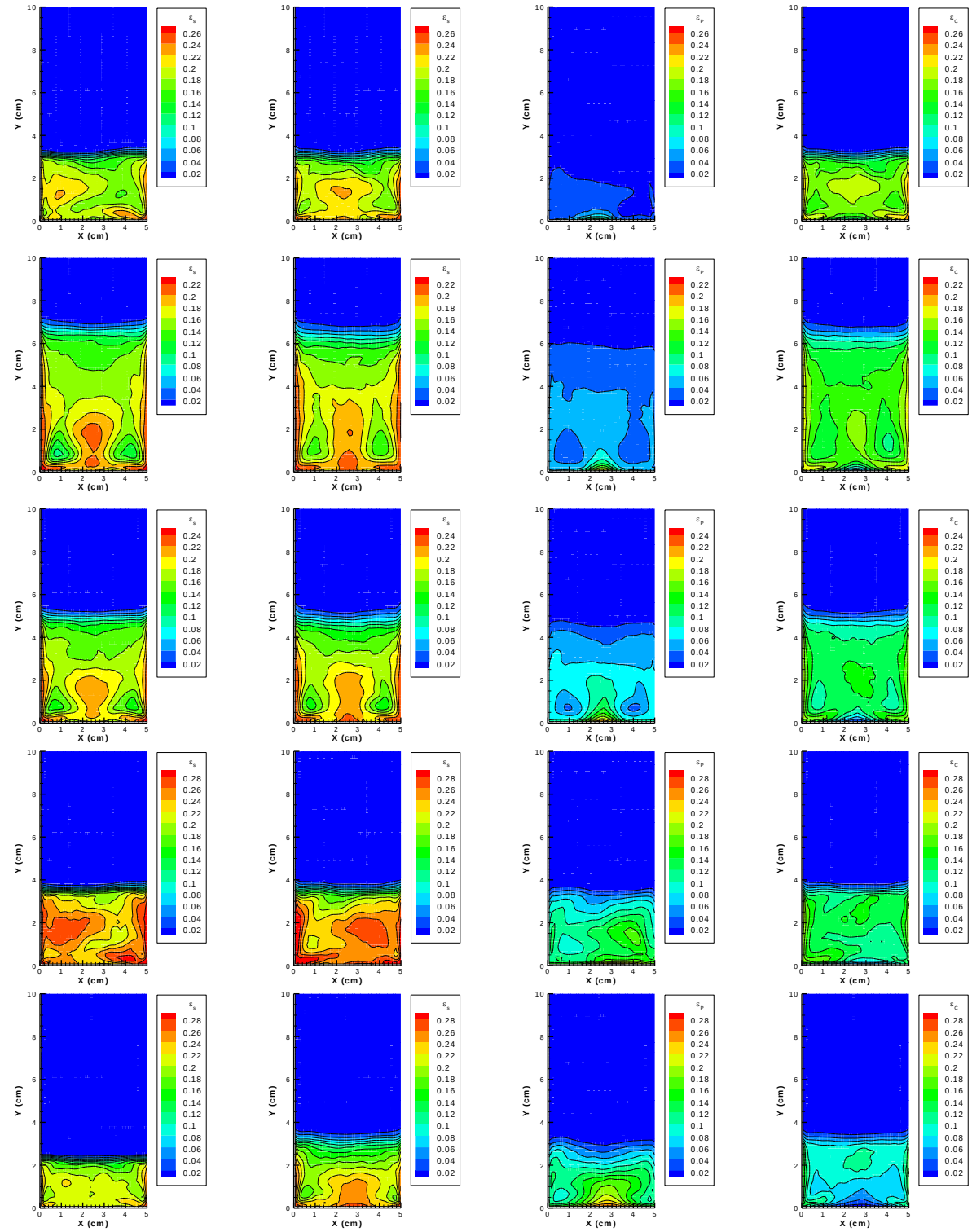

(a) Total solids volume fraction (S) (b) Total solids volume fraction (B) (c) Poplar volume fraction (d) Coal volume fraction

Figure 6.15. Time averaged solids volume fraction contours at $U_g/U_{mf} = 2$. (a) Total solids volume fraction (single solids model), (b) total solids volume fraction (binary mixture model), (c) poplar volume fraction and (d) coal volume fraction. Top row to bottom row are mixture ratios of poplar-coal at 10:90, 20:80, 30:70, 40:60 and 50:50, respectively

For the 40:60 mixture, the time averaged solids volume fraction contours are fairly similar for both single solids and binary mixture models, with particles being distributed on the left side of the bed for the single solids and the right side for the binary mixture. The increasing influence of poplar wood in the hydrodynamics of the binary mixture can be observed.

The 50:50 binary mixture clearly indicates how further increasing the poplar wood affects the hydrodynamics. The single solids model predicts an asymmetric distribution, the binary mixture model is symmetric. Further analysis of the individual solids volume fraction contours indicates the influence of poplar wood within in the central region of the bed, with the coal particles being uniformly distributed. The bed expansion height observed is higher for the binary mixture model than the single solids model.

Figure 6.16 represents solids volume fraction contours for the models obtained at different instants of 5s, 10s, 15s and 20s during the fluidization of the 40:60 poplar wood-coal binary mixture at $U_g = 2\ U_{mf}$. The single solids model shows that the bed is fairly well mixed quickly in time with less bubbles in the bed. The total solids volume fraction from the binary mixture model shows a bed where the distribution of solids becomes more uniform over time. Analyzing the poplar wood volume fraction, the influence of switchgrass over the bed can be seen, with the poplar wood initially concentrated at the bottom of the bed and subsequently being redistributed to other regions of the bed. The coal particles are initially dominant in the top half of the bed. When the switchgrass begins to mix with it over time, the coal particles are redistributed fairly uniformly over the entire bed.

6.5.3. *Cornstover-Coal Binary mixture*

6.5.3.1. *Pressure drop*

Pressure drop measured in the experiments is compared with predictions made by both models for cornstover-coal binary mixtures and presented in Figure 6.17. Table 6.4 presents the modeling parameters used for cornstover-coal 10:90 mixture. The modeling parameters used for the remaining mixtures are listed in the Appendix A. For the cornstover-coal mixture of 10:90, the experiments indicate a linearly increasing pressure drop until the point of fluidization after which the pressure drop remains constant. Both simulation models capture the minimum fluidization velocity, and pressure drop fairly accurately. For the 20:80 binary mixture, experiments show a similar trend as observed with 10:90 mixture with the pressure drop linearly increasing before

fluidization and remaining constant after. The single solids model is able to capture both U_{mf} and pressure drop fairly accurately, while the binary mixture model captures the pressure drop and a slightly higher U_{mf} in comparison with the experiments.

For the binary mixtures with cornstover-coal ratios of 30:70, 40:60 and 50:50, the experiments indicate a linearly increasing pressure drop until the point of fluidization, subsequently remaining constant. The single-solids model is able to predict both pressure drop and minimum fluidization velocity fairly accurately for these mixtures when compared with experiments. However as the content of cornstover in the bed increases, the binary mixture model predicts a higher U_{mf} when compared to the experiments. As the content of the cornstover increases in the bed, the binary mixture model also fails to capture the pressure drop accurately as well. Judging by these observations, it would appear that the binary mixture model is incapable of modeling cornstover-coal hydrodynamics. It is also interesting to point out that the experiments experienced poor fluidization when cornstover was used.

Table 6.4. Modeling parameters used for cornstover-coal 10:90 mixture

Properties	**Experiments**		**Sim-S**	**Sim -B**	
	Cornstover	Coal	Mix. Props.	Cornstover	Coal
d_p(μm)	418	62	*69*	418	62
ψ(-)	-	-	1	1	1
ρ_s (g/cm^3)	1.21	1.38	1.36	1.21	1.38
m(g)	3	27	*24.3*	*2.4*	*21.9*
ρ_b (g/cm^3)	-	-	0.30	0.03	0.27
X_i (-)	0.10	0.90		0.10	0.90
ε_g(-)			*0.78*	*0.78*	
h_o(cm)	3		*4*	*4*	

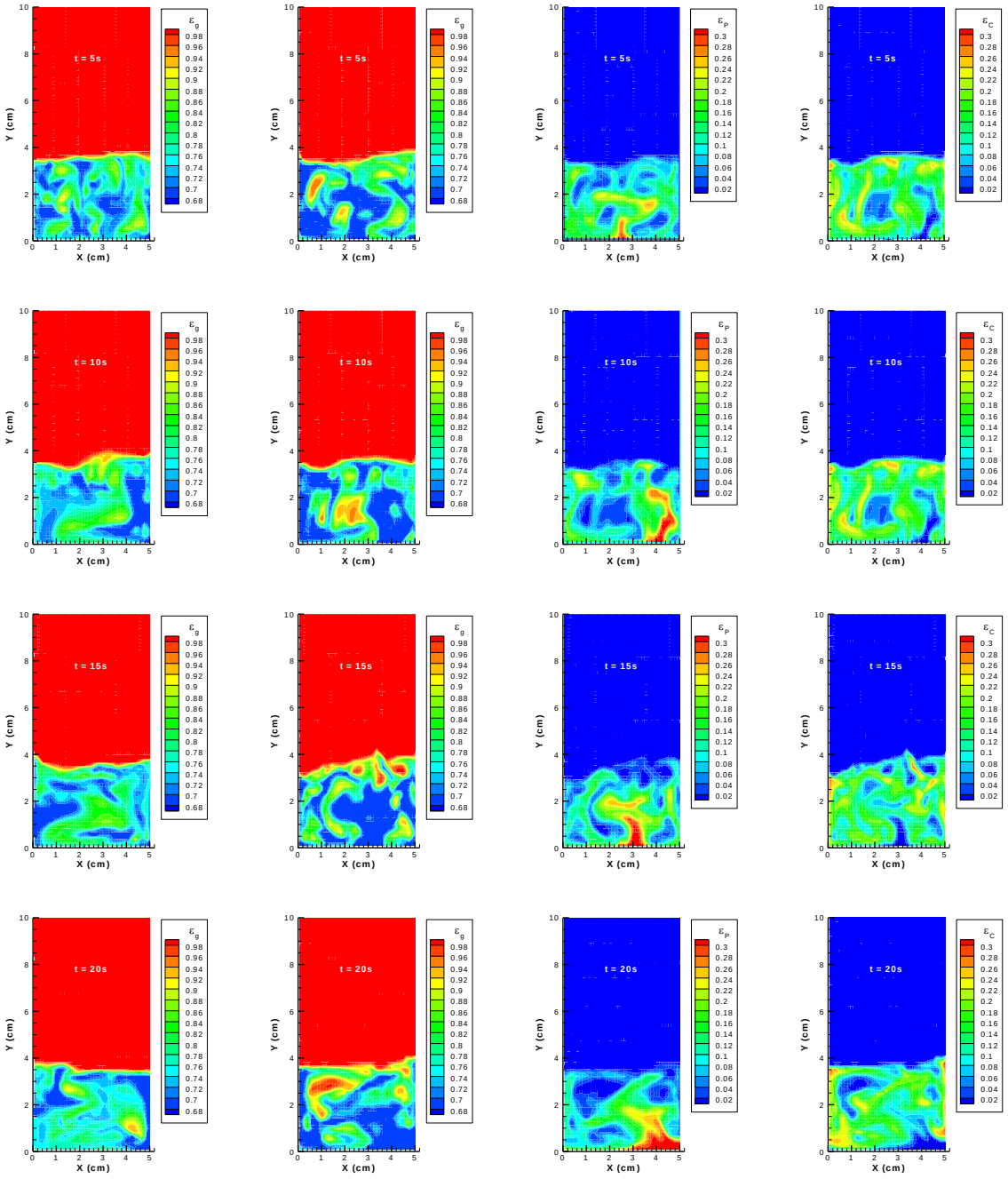

(a) Gas volume fraction (S) (b) Gas volume fraction (B) (c) Poplar volume fraction (d) Coal volume fraction

Figure 6.16. Instantaneous volume fraction contours at $U_g/U_{mf} = 2$ for the mixture ratio of 20:80. (a) Total gas volume fraction using the single solids model, (b) total gas volume fraction using the binary mixture model, (c) poplar volume fraction and (d) coal volume fraction. Top row to bottom row are at the instants of 5s, 10s, 15s and 20s respectively

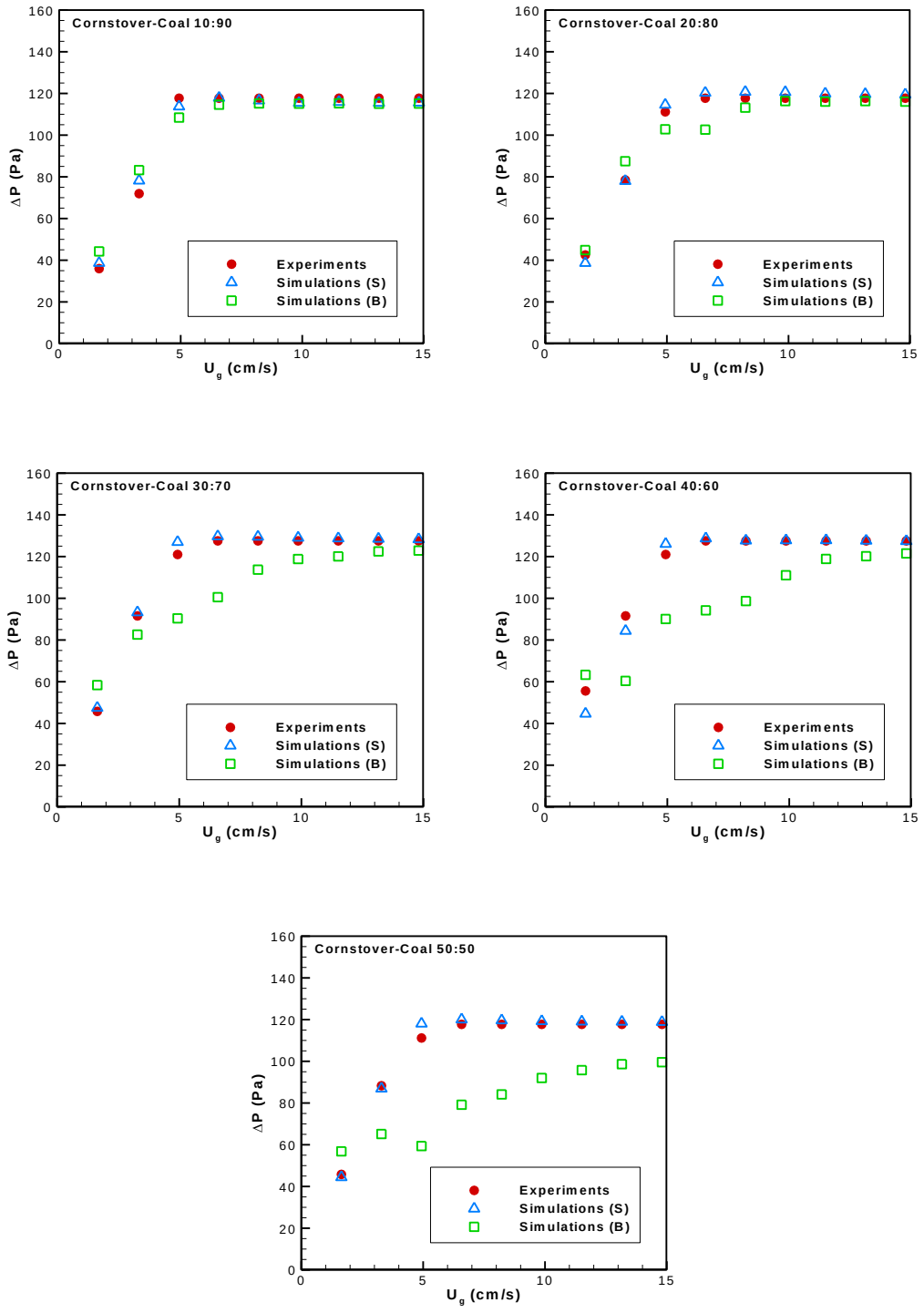

Figure 6.17. Comparison of pressure drop between experiments and simulations for single solids and binary mixture models for cornstover-coal mixtures

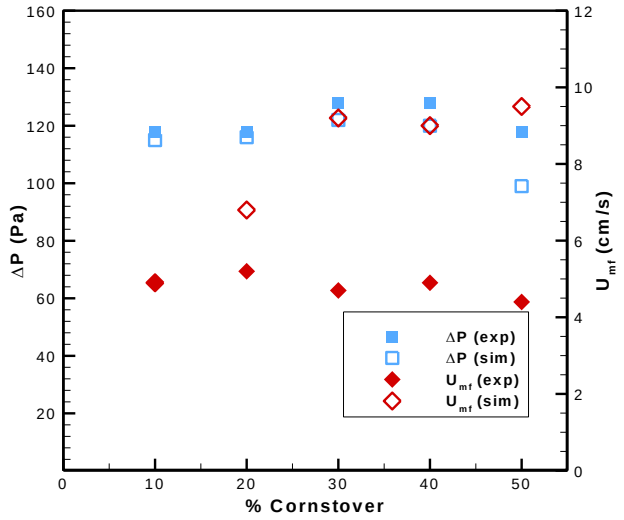

Figure 6.18. Pressure drop and minimum fluidization velocity estimates comparing binary mixtures of cornstover and coal

Figure 6.18 compares the pressure drop and the minimum fluidization velocity measured in the experiments with the predictions made by the simulations for different cornstover-coal binary mixtures. The filled symbols indicate the experimental measurements and the hollow symbols show simulation predictions.

The effect of increasing the mass of cornstover present in the binary mixture on pressure drop and minimum fluidization velocity can be seen in Figure 6.18. With increasing mass of cornstover, the pressure drop measured by the experiments remains constant until cornstover is equal to 30% the mass of the entire bed. The simulations slightly under-predict the pressure drop measured experimentally, until the bed contains 40% cornstover. Pressure drop measured in the experiments decreases when half the bed contains cornstover. While a decrease in pressure drop observed at 50% cornstover is also captured by the simulations, the predicted pressure drop is lower than that measured in the experiments. The binary mixture simulations are unable to capture the pressure drop accurately with increasing cornstover content.

The minimum fluidization velocity decreases slightly with increasing cornstover mass in the bed. The simulations compare very well with the U_{mf} measured with the experiments when cornstover is 10% of the bed. With increasing cornstover content, the simulations over-predict U_{mf}.

As was mentioned earlier, it was observed in the experiments that cornstover-coal had poor fluidization with less mixing. It would appear that the inability of the simulations predict accurately the U_{mf} and pressure drop could be pointing to the poor fluidization characteristics of cornstover.

6.5.3.2. *Bed expansion heights*

Figure 6.19 compares expanded bed heights normalized with the initial bed height for the binary mixtures containing cornstover and coal for varying inlet gas velocities. For all the mixtures, with increasing inlet velocity, the normalized expanded bed height also increases. The same trend is captured by the simulations, with both models predicting similar bed expansion heights. The simulations under-predict expanded bed heights, when compared with the experiments for binary mixtures containing cornstover content of 10, 20, 30 and 40% of the bed mass, also showing a linear rate of increasing bed expansion. Both single solids and binary mixture simulation models give similar predictions. Simulations indicate a lower rate of bed expansion prior to the point of minimum fluidization with a slightly higher rate later on, for a lower bed height in comparison with the experiments. The experiments have a non-linear rate of increase in bed expansion height. For the 50:50 cornstover-coal mixture, the simulations compare better with the experiments than other mixtures, with the simulations giving similar predictions until about U_g = 1.5 U_{mf}, beyond which the simulations under-predict bed expansion heights. It should also be noted that that the experimental error in bed expansion heights would be higher than the simulations considering the fact that the measurements were obtained through observation and a ruler.

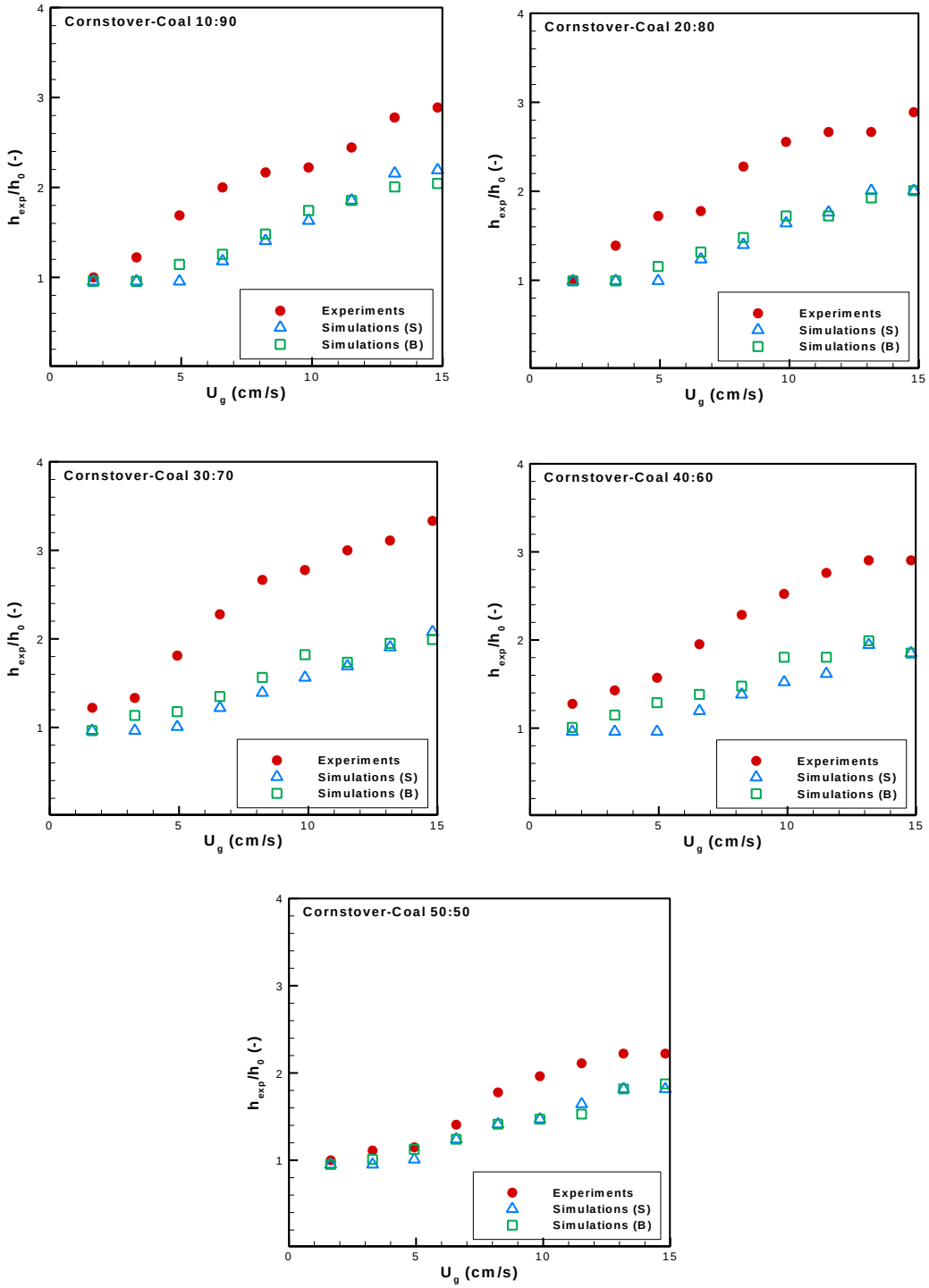

Figure 6.19. Comparison of normalized bed expansion heights predictions between experiments and single solids and binary mixture models of simulations for switchgrass-coal binary mixtures

6.5.3.3. *Solids volume fraction contours*

Further analysis using the solids volume fraction contours are considered for the cornstover-coal binary mixture. Figure 6.20 presents solids volume fraction contours time-averaged from 5 to 20s for the inlet velocity at 2 U_{mf} at a sampling rate of 100 Hz.

For the 10:90 binary mixture, the single solids model and binary mixture model present a more symmetric distribution about the vertical centerline of the bed. Cornstover is mainly concentrated near the bottom of the bed. The hydrodynamics of the bed modeled using the binary mixture model is clearly dominated by coal.

For the 20:80 mixture, the single solids model indicates a symmetrically distributed bed, with the binary mixture model indicating more solids concentrated near the bottom of the bed. Analyzing the individual components contribution to the solids volume fraction indicates that cornstover is mixing more within the lower portion of the bed. Coal is fairly uniformly distributed throughout the bed. Majority of the solids volume fraction contribution is from coal for the top half of the bed, with cornstover influencing the bottom half.

For the 30:70 mixture, the time averaged total solids volume fraction predicted by the single solids model and the binary mixture model are similar, with a symmetrical distribution of solid particles about the vertical centerline. The binary mixture model indicates regions of the bed that are concentrated with solids near the bottom of the bed in comparison to the single solids model. Upon analyzing individual solids volume fraction contours, it is clear that cornstover is present in the bottom of the bed. Coal is fairly distributed throughout the domain, and is responsible for the bed expansion height observed.

For the 40:60 mixture, the time averaged solids volume fraction contours are different between single solids and binary mixture models. The single solids model predicts a bed where there is non-uniform distribution of solids about the bed. The binary mixture model however indicate solids remaining not fluidizing at the bottom of the bed. Cornstover doesn't seem to be contributing to the fluidization, as it is present more in these deadzones. Coal appears to be distributed on top half of the bed. However the lack of uniform fluidization observed for this mixture seems to point towards the fact that increasing the mass percent of cornstover doesn't seem to improve fluidization.

The 50:50 binary mixture clearly indicates how further increasing the cornstover doesn't help with fluidization of the mixture. The single solids model predicts a uniform distribution, while

the binary mixture model shows a bed that is yet to fluidize. Further analysis of the individual solids volume fraction contours indicates the cornstover content within the bed contributing to the lack of fluidization observed. The bed expansion height observed for the binary mixture particles seems to be due to the coal particles.

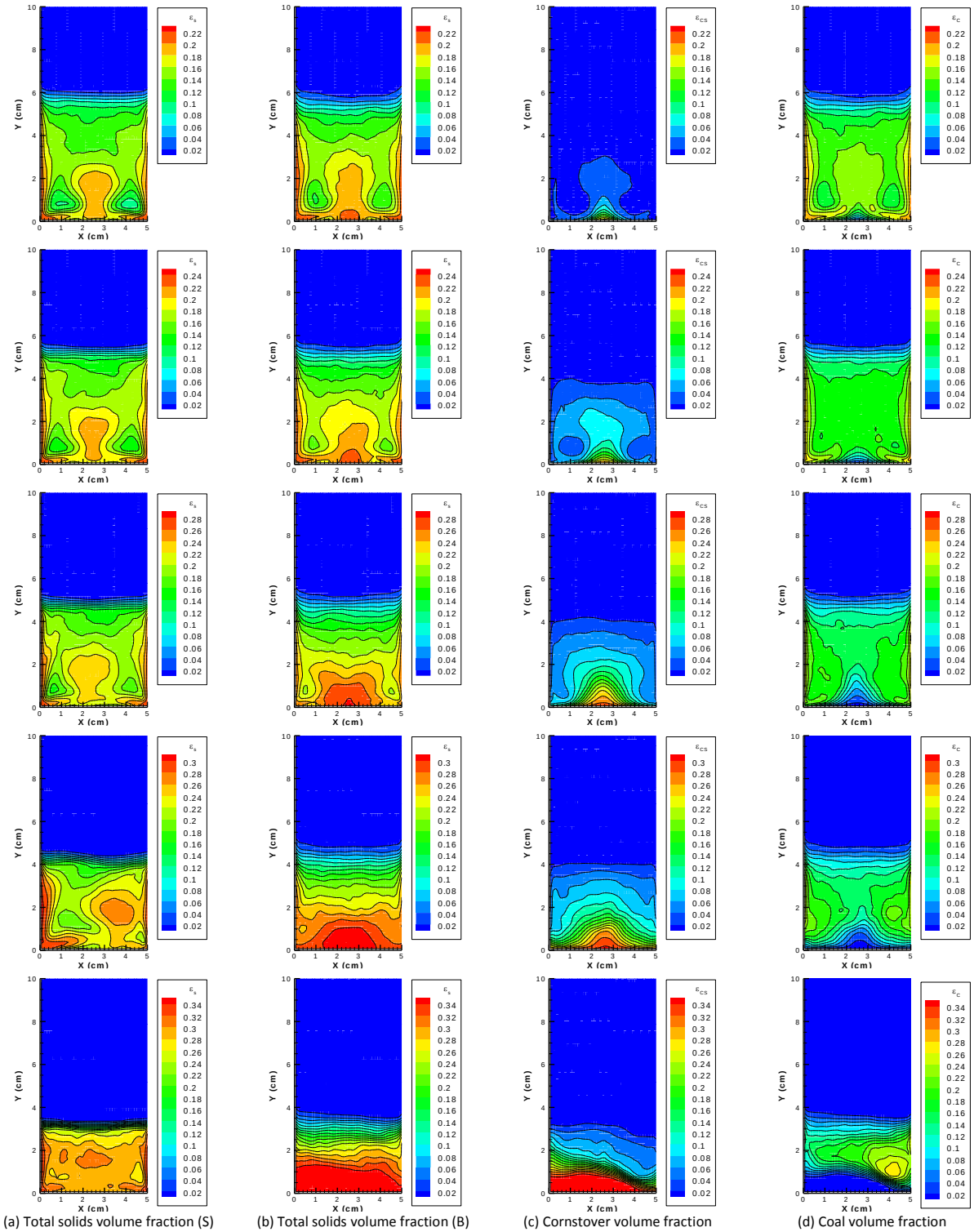

Figure 6.20. Time averaged solids volume fraction contours at U_g/U_{mf} = 2. (a) Total solids volume fraction using the single solids model, (b) total solids volume fraction using the binary mixture model, (c) switchgrass volume fraction and (d) coal volume fraction. Top row to bottom row are mixture ratios of 10:90, 20:80, 30:70, 40:60 and 50:50, respectively

Chapter 7. Conclusions and Recommendations

7.1. Conclusions

Fluidized bed reactors have many industrial applications due to excellent mixing and heat-transfer characteristics. The design of the reactors can be effectively pursued through the use of CFD, making it cheaper than pilot-scale experiments. However CFD modeling of fluidization hydrodynamics can be very challenging. The goal of this study was to computationally model fluidized bed using a finite volume CFD code (MFIX), and validate the simulation predictions with experiments whenever possible.

The first part of the study was focused on modeling non-uniform inlet conditions caused by the distributor plate and is presented in Chapter 4. An adjusted mass model was used to capture the non-uniform inlet conditions arising from the distributor plate. The model accounted only for the fluidizing mass contributing to the pressure drop using experimental measurements of pressure drop and minimum fluidization velocity. The model was applied on single solids phase and binary mixtures. The model was also able to account for the non-uniform nature of the hollow ceramic particles by using a better estimate of initial void fraction present in the bed. Pressure drop and minimum fluidization velocity predictions made by the adjusted model compared very well with the experimental measurements.

The second part of the research extended the study of distributor plate modeling by making use of an inlet configuration with 9 and 5 holes, which was then used to analyze the hydrodynamics for a quasi-2D fluidized bed. Simulations were performed for a quasi-2D bed with a 9-hole and 5-hole distributor plate configuration in both 2D and 3D simulations. Pressure drop, solids volume fraction contours and profiles, and solids velocity vectors were compared between simulations and experiments. Three different grid resolutions were examined for the 9-holed distributor. It was found that 3D simulations are necessary to model the discrete jets with more accuracy. For the 5-holed distributor, fine grid simulations were used for the 2D and 3D simulations. The jets penetrated higher into the bed for the 3D simulation of 5-holed distributor more than the experiments, possibly indicating the need for a better turbulence model in order to capture the diffusion of the high velocity jets. Deadzone mass, which represents non-fluidizing solids, was also analyzed, which further proved the need for modeling the quasi-2D bed using 3D simulations.

Deadzone distributions within the bed were also analyzed. It was found that as the distance between the jets increased, the size of the deadzones between the jets also increased in height. The distribution of deadzone around the jet was also observed to be higher towards the back wall than the wall closer to the jets.

For the final part of the study, hydrodynamics of coal and biomass blends of switchgrass, cornstover, and poplar wood were investigated using the adjusted mass model developed in Chapter 4. The CFD predictions were compared with experimental measurements provided by the team led by Prof. Agblevor at Utah State University. The adjusted mass models were found to perform reasonably well for both the single solids fluidized bed and binary mixture fluidized bed in predicting fluidization characteristics such as pressure drop for different inlet gas velocities, and minimum fluidization velocity. Bed heights predicted by the simulations were able to indicate the point of fluidization, and compared reasonably well with the experiments. For the binary mixtures, the adjusted mass models were implemented using a representative particle, and as binary mixtures, and were able to compare very well with the experiments for switchgrass and poplar wood. Prediction of fluidization characteristics were found to be difficult for cornstover-coal mixture with the binary mixture model with increasing cornstover mass in the bed. Time-averaged solids volume fraction contours were analyzed for each mixture, along with solids volume fraction contour for corresponding individual constituents. It was found that with increasing biomass content, the influence biomass constituent in the fluidized bed hydrodynamics increased. For switchgrass-coal and poplar wood-coal mixture, the optimum mixture ratio was found to be 20:80. The cornstover-coal binary mixture model showed that cornstover was not fluidizing and thus not contributing to the pressure drop as percent of cornstover in the bed increased. The effectiveness of adjusted mass model in capturing fluidization characteristics of coal, biomass, and coal-biomass mixtures were thus clearly illustrated.

7.2. Recommendations

The adjusted mass model was clearly illustrated as the modelling technique to capture the effect of non-uniform inlet study in chapter 4. For future work, it would be of interest to study the effects of different drag models upon the model. The effect of different numerical schemes upon the prediction for fluidization trends would also be interesting.

It would be of clear interest to investigate different turbulence models for the modeling of jets. The Ahmadi turbulence model was used for the simulation. For the 5-holed distributor, the jets

formed channels to the surface of the bed, unlike the experiments were the jets diffused halfway through the bed. A multiphase turbulence model accounting of the diffusion of the jets / momentum dissipation would also be interesting to see. An alternative approach would be to develop constitute relations from DPM simulation results and adapt it within the Eulerian-Eulerian modeling framework to account for the turbulence in the jets.

The use of adjusted mass model can also be studied further for different biomass materials, and could also be possibly validated for a variety of biomass fluidized beds. For the future work, a parametric investigation of sphericity, coefficient restitution, specularity coefficient, may be investigated. An alternative would be to account for particle breakage for biomass particles, and subsequently the presence of a wide variety of particle sizes in the fluidized bed by making use of population balance models within the bed. The ultimate test of the adjusted mass model would be to simulate a gasification reaction within a fluidized bed by making use of a chemical reaction model to simulate coal-biomass gasification. It would be interesting to see the difference of predictions between an original mass model and the adjusted mass model as well.

References

[1] Kunii, D. and Levenspiel, O., 1991, Fluidization Engineering, Butterworth-Heinemann, Boston, USA.

[2] Delebarre, A., 2002 "Does the Minimum Fluidization Exist?". *Journal of Fluids Engineering-Trans. ASME*, **124**, September, pp. 595-600.

[3] Pepiot, P., C. J. Dibble, Foust T.D., 2010. "Computational Fluid Dynamics Modeling of Biomass Gasification and Pyrolysis". Computational Modeling in Lignocellulosic Biofuel Production, American Chemical Society. **1052**: 273-298.

[4] Gòmez-Barea A., Leckner B., 2010. Modeling of biomass gasification in fluidized bed. *Prog. Energy Combustion Sci.*, **36**, 444-509.

[5] Bridgwater, A.V., 1995. "The technical and economical feasibility of biomass gasification for power generation. *Fuel* **74**, 631-653.

[6] Prins M. J., Ptasiński K. J., Janssen F.J.J.G., 2007. From coal to biomass gasification: Comparison of thermodynamic efficiency. *Energy*, **32**, 1248-1259.

[7] Pannala, S., D'Azevedo, E. Syamlal, M., 2003. "Hybrid (OpenMP and MPI) Parallelization of MFIX: A Multiphase CFD Code for Modeling Fluidized Beds". *Proceedings of the 2003 ACM symposium on Applied computing*, ACM Press, 199-206.

[8] Chodak, J., 2010."Pyrolysis and Hydrodynamics of Fluidized Bed Media". M.S Thesis 2010, etd-05172010-091509.

[9] Agarwal, G., Lattimer, B., Ekkad, S., Vandsburger, U., 2011, "Influence of multiple gas inlet jets on fluidized bed hydrodynamics using Particle Image Velocimetry and Digital Image Analysis", *Powder Technology*. **214**(1), 122-134.

[10] Gidaspow, D., 1994. *Multiphase Flow and Fluidization: Continuum and Kinetic Theory Descriptions*. Academic Press, Boston, MA.

[11] Boyalakuntla, D., 2003. "Simulation of Granular and Gas-Solid Flows Using Discrete Element Method". PhD dissertation, Carnegie Mellon University, Pittsburgh, Pennsylvania.

[12] Huilin, L., Shuyan, W., Yunhua, Z., Yang, L., Gidaspow, D., Ding, J. 2005, "Prediction of particle motion in a two-dimensional bubbling fluidized bed using discrete hard-sphere model". *Chemical Engineering Science*, 60 (12). pp. 3217-3231.

[13] Syamlal, M., O'Brien, T. J., 1988. "Simulation of granular layer inversion in liquid fluidized beds". *International Journal of Multiphase Flow,* 14 (4). pp. 473-481.

[14] Zimmerman, S., Taghipour, F., 2005. "CFD modeling of the hydrodynamics and reaction kinetics of FCC fluidized-bed reactors". *Industrial and Engineering Chemistry Research,* 44 (26). pp. 9818-9827.

[15] Sun, J., Battaglia, F., Subramaniam, S., 2007. "Hybrid Two-Fluid DEM Simulation of Gas-Solid Fluidized Beds". *J. Fluids Eng.-Trans. ASME,* 129(11), pp. 1394-1403.

[16] vanWachem, B.G.M, Almstedt, A.E., 2003. "Methods for multiphase computational fluid dynamics". *Chemical Engineering Journal*, 96, pp. 81–98.

[17] Esmaili, E., Mahinpey, N., 2001. "Adjustment of drag coefficient correlations in three dimensional CFD simulation of gas-solids bubbling fluidized bed". *Advances in Engineering Software*, 42, pp. 375-386.

[18] Pei, P., Zhang, K., Wen, D., 2012. "Comparative analysis of CFD models for jetting fluidized beds: The effect of inter-phase drag force". *Powder Technology*, 221, pp. 114-122.

[19] Deza, M., Franka, N. P., Heindel, T.J., and Battaglia, F., 2009. "CFD modeling and X-ray imaging of biomass in a fluidized bed". *J. Fluids Eng.-Trans. ASME,* 131 (11), pp. 111303.

[20] Hosseini, S.H., Zhong, W., Esfahany, M.N., Pourjafar, L., Azizi, S., "CFD Simulation of the Bubbling and Slugging Gas-Solid Fluidized Beds". *J. Fluids Eng.-Trans. ASME,* 132(4), pp. 041301.

[21] Gavi, E., Heindel, T.J., Fox, R.O., 2010. "Modeling fluidization in biomass gasification processes". In proceedings of International Conference on Multiphase Flow. Paper No 1956.

[22] van Wachem, B.G.M., Schouten, J.C., van den Bleek, C.M., 2001. "CFD Modeling of Gas-Fluidized beds with a Bimodal Particle Mixture". *AIChE Journal*. 47(6), pp. 1292-1302.

[23] Zhang, K., Zhang, J., Zhang, B., 2003."Experimental and numerical study of fluid dynamic parameters in a jetting fluidized bed of a binary mixture". *Powder Technology*. 132, pp. 30– 38.

[24] Gao, J., Chang, J. Lu, C., Xu, C., 2008. "Experimental and computational studies on flow behavior of gas–solids fluidized bed with disparately sized binary particles". *Particuology.* 6, pp. 59-71.

[25] Coroneo, M., Mazzei, L., Lettieri, P., Paglianti, A., Montante, G., 2011. “CFD prediction of segregating fluidized bi-disperse mixtures of particles differing in size and density in gas-solids fluidized beds”. *Chemical Engineering Science.* 66, 2317-2327.

[26] Geldart, D. and Baeyens, J., 1985, “The design of distributors for gas-fluidized beds”, *Powder Technology*, **42(**1): 67–78.

[27] Sasic. S., Johnsson. F., Leckner, B., 2006, “Inlet Boundary Conditions for the simulation of fluid dynamics in gas- solid fluidized beds”, *Chemical Engineering Science*, **61**, 5183-5195.

[28] Paiva, J.M., Pinho. C, Figueiredo, R., 2004, “The influence of Distributor plate on the bottom zone of a fluidized bed approaching the transition from Bubbling to Turbulent Fluidization”. Trans IChemE, Part A, *Chemical Engineering Research and Design*, **82**(A1): 25-33.

[29] Gelderbloom, S.J., Gidaspow, D., Lyczkowski, R.W., 2003, “CFD Simulations of Bubbling/Collapsing Fluidized Beds for Three Geldart Groups”. *AiChE Journal,* Vol **49** No. 4 844-858.

[30] Syamlal, M. and O'Brien, T. J., 1989, “Computer simulation of bubbles in a fluidized bed”. *AIChE Symp*. Ser. 85, 22-31.

[31] Ding,J., and Gidaspow, D., “A bubble fluidisation model using kinetic theory of granular flow”, *AIChE, J.* **36**(4), 523 (1990).

[32] Boehmer, A., QI, H., and RENZ,U., 1997,“Eulerian simulation of bubble formation at a Jet in a two-dimensional fluidized bed”, *Int. J. Multiphase Flow* Vol. **23**, No. 5, pp. 927-944.

[33] Hernandez-Jimenez,F., Sanchez-Delgado,S., Gomez-Garcia, A., Acost-Iborra, A., 2011, “Comparison between two-fluid model simulations and particle image analysis and velocimetry (PIV) results for a two-dimensional gas-solid fluidized bed”, *Chemical Engineering Science*, **66**, 3753-3772.

[34] Utikar, R.P., Ranade, V.V., 2007, “Single jet fluidized beds: Experiments and CFD simulations with glass and polypropylene particles”,*Chemical Engineering Science* **62**, 167-183.

[35] R.Y. Hong, Q.J. Guo, G.H. Luo, J.-Y. Zhang, J. Ding, On the jet penetration height in fluidized beds with two vertical jets, Powder Technology, Volume 133, Issues 1–3, 30 July 2003, Pages 216-227

[36] Seyyed Hossein Hosseini, Goodarz Ahmadi, Rahbar Rahimi, Mortaza Zivdar, Mohsen Nasr Esfahany, CFD studies of solids hold-up distribution and circulation patterns in gas–solid fluidized beds, Powder Technology, Volume 200, Issue 3, 28 June 2010, Pages 202-215

[37] Heping Cui, John R. Grace, Fluidization of biomass particles: A review of experimental multiphase flow aspects, Chemical Engineering Science, Volume 62, Issues 1–2, January 2007, Pages 45-55

[38] Kai Zhang, Bangting Yu, Jian Chang, Guiying Wu, Tengda Wang, Dongsheng Wen, Hydrodynamics of a fluidized bed co-combustor for tobacco waste and coal, Bioresource Technology, Volume 119, September 2012, Pages 339-348

[39] T R. Rao, J.V Ram. Bheemarasetti, Minimum fluidization velocities of mixtures of biomass and sands, Energy, Volume 26, Issue 6, June 2001, Pages 633-644

[40] Papadikis, K., Bridgwater, A., and Gub, S., 2008, CFD modelling of the fast pyrolysis of biomass in fluidised bed reactors, part A: Eulerian computation of momentum transport in bubbling fluidised beds," Chemical Engineering Science, 63, pp. 4218 4227.

[41] Papadikis, K., Gub, S., and Bridgwater, A., 2010, A CFD approach on the effect of particle size on char entrainment in bubbling fluidised bed reactors," Biomass and Bioenergy, 34, pp. 21-29.

[42] Abhishek Sharma, Shaobin Wang, Vishnu Pareek, Hong Yang, Dongke Zhang, CFD modeling of mixing/segregation behavior of biomass and biochar particles in a bubbling fluidized bed, Chemical Engineering Science, Volume 106, 17 March 2014, Pages 264-274

[43] Wei Bai, Norman K.G. Keller, Theodore J. Heindel, Rodney O. Fox, Numerical study of mixing and segregation in a biomass fluidized bed, Powder Technology, Volume 237, March 2013, Pages 355-366

[44] Syamlal, M., Rogers, W., and O'Brien, T., 1993. MFIX Documentation: Theory Guide. Technical Note DOC/METC-95/1013 and NTIS/DE95000031, National Energy Technology Laboratory, Department of Energy.

[45] Xie, N., Battaglia, F., and Pannala, S., 2008, “Effects of Using Two-Versus Three-Dimensional Computational Modeling of Fluidized Beds: Part I—Hydrodynamics,” Powder Technol., 182(1), pp. 1–13.

[46] Abu-Zaid, S., Ahmadi, G., 1993, “A Thermodynamically Consistent Rate-Dependent Model for Turbulent Two-Phase Flows, Part I – Formulation,” MAE Report-281.

[47] Ahmadi, G., 1991. “A Thermodynamically Consistent Rate-Dependent Model for Turbulence, Part I – Formulation”, *Int. J. Non-Linear Mech.* **26**(5), pp. 595-607.

[48] Schaeffer, D.G., 1987, "Instability in the Evolution Equations Describing Incompressible Granular Flow," *J. Diff. Eq*., 66, 19-50.

[49] Wilcox, D.C., Turbulence Modeling for CFD, DCW Industries, California, 1994.

[50] Tannehill, J.C., Anderson, D.A., and Pletcher, R.H., 1997, *Computational Fluid Mechanics and Heat Transfer,* Taylor & Francis, Inc., second edition.

[51] Battaglia, F., England, J. A., Kanholy, S., Deza, M., 2010. “On the modeling of gas-solids fluidization: which physics are most important to capture?”. In Proceedings of ASME International Mechanical Engineering Congress and Exposition 2010.Paper: IMECE2010-40213.

[52] Geldart, D., 1973. “Types of gas fluidization”, *Powder Technology,* 7(5), pp. 285-292.

[53] Delebarre, A., 2002. “Does the Minimum Fluidization Exist?”. *J. Fluids Eng.-Trans. ASME,* 124(3), pp. 595-600

[54] Ergun, S., 1952, “Fluid Flow Through Packed Columns,” Chem. Eng. Prog., 48(2), pp. 89–94.

[55] Chyang, C.-S., Kuo, C.-C., Chen, M.-Y., 1989. “Minimum Fluidization Velocity of Binary Mixtures”. *Canadian Journal of Chemical Engineering.* 67, pp. 344-247.

[56] Deza, M., Franka, N. P., Heindel, T.J., and Battaglia, F., 2009. “CFD modeling and X-ray imaging of biomass in a fluidized bed”. *J. Fluids Eng.-Trans. ASME,* 131 (11), pp. 111303.

[57] McKeen, T., and Pugsley, T., 2003, “Simulation and Experimental Validation of a Freely Bubbling Bed of FCC Catalyst,” Powder Technol., 129(1–3), pp.139–152.

[58] Chandrasekaran, B. K., van der Lee, L., Hulme, I., and Kantzas, A., 2005, “A Simulation and Experimental Study of the Hydrodynamics of a Bubbling Fluidized Bed of Linear Low Density Polyethylene Using BubbleProperties and Pressure Fluctuations,” Macromol. Mater. Eng., 290(6), pp. 592–609.

Appendix A

Tables A1-A4 lists the modeling parameters used for different switchgrass-coal binary mixtures, A5-A8 for different poplar wood-coal binary mixtures, and A9-A12 for different cornstover-coal binary mixtures. Sim-S is the single solids model, and Sim-B the binary mixture model based on the fluidizing mass contributing to the pressure drop. Sim-S model is similar to the Sim-S model mentioned in Chapter 4. Sim-B model is similar to the Sim-B2 model presented in Chapter 4.

Table A1. Modeling parameters used for switchgrass-coal 20:80 mixture

Properties	**Experiments**		**Sim-S**	**Sim -B**	
	Switchgrass	Coal	Mix. Props.	Switchgrass	Coal
d_p(μm)	145	62	*72*	145	62
ψ(-)	-	-	1	1	1
ρ_s (g/cm^3)	1.1	1.38	1.31	1.1	1.38
m(g)	6	24	*23.7*	*4.7*	*18.9*
ρ_b (g/cm^3)	-	-	0.49	0.1	0.4
X_i (-)	0.2	0.8		0.2	0.8
ε_g(-)	-		*0.62*	*0.62*	
h_0(cm)	3		*2.4*	*2.4*	

Table A2. Modeling parameters used for switchgrass-coal 30:70 mixture

Properties	**Experiments**		**Sim-S**	**Sim -B**	
	Switchgrass	Coal	Mix. Props.	Switchgrass	Coal
d_p(μm)	145	62	*78*	145	62
ψ(-)	-	-	1	1	1
ρ_s (g/cm^3)	1.1	1.38	1.28	1.1	1.38
m(g)	9	21	*24.3*	*7.3*	*17*
ρ_b (g/cm^3)	-	-	0.26	0.08	0.18
X_i (-)	0.3	0.7		0.30	0.70
ε_g(-)	-		*0.80*	*0.80*	
h_0(cm)	3		*4.6*	*4.6*	

Table A3. Modeling parameters used for switchgrass-coal 40:60 mixture

Properties	Experiments		Sim-S	Sim -B	
	Switchgrass	Coal	Mix. Props.	Switchgrass	Coal
d_p(μm)	145	62	*85*	145	62
ψ(-)	-	-	1	1	1
ρ_s (g/cm^3)	1.1	1.38	1.25	1.1	1.38
m(g)	12	18	*28.4*	*11.4*	*17.0*
ρ_b (g/cm^3)	-	-	0.25	0.1	0.15
X_i (-)	0.4	0.6		0.4	0.6
ε_g(-)	-		*0.80*	*0.80*	
h_0(cm)	3		*5.7*	*5.7*	

Table A4. Modeling parameters used for switchgrass-coal 50:50 mixture

Properties	Experiments		Sim-S	Sim -B	
	Switchgrass	Coal	Mix. Props.	Switchgrass	Coal
d_p(μm)	145	62	*93*	145	62
ψ(-)	-	-	1	1	1
ρ_s (g/cm^3)	1.1	1.38	1.22	1.1	1.38
m(g)	15	15	*20.3*	*10.1*	*10.1*
ρ_b (g/cm^3)	-	-	0.30	0.15	0.15
X_i (-)	0.5	0.5		0.5	0.5
ε_g(-)	-		*0.75*	*0.75*	
h_0(cm)	3		*3.3*	*3.3*	

Table A5. Modeling parameters used for poplar wood-coal 20:80 mixture

Properties	Experiments		Sim-S	Sim -B	
	Poplar wood	Coal	Mix. Props.	Poplar wood	Coal
d_p(μm)	153	62	*72*	153	62
ψ(-)	-	-	1	1	1
ρ_s (g/cm^3)	1.12	1.38	1.32	1.12	1.38
m(g)	6	24	*29.1*	*5.8*	*23.2*
ρ_b (g/cm^3)	-	-	0.30	0.06	0.24
X_i (-)	0.2	0.8		0.2	0.8
ε_g(-)	-		*0.77*	*0.77*	
h_0(cm)	3		*4.7*	*4.7*	

Table A6. Modeling parameters used for poplar wood-coal 30:70 mixture

Properties	Experiments		Sim-S	Sim -B	
	Poplar wood	Coal	Mix. Props.	Poplar wood	Coal
d_p(μm)	153	62	*78*	153	62
ψ(-)	-	-	1	1	1
ρ_s (g/cm^3)	1.12	1.38	1.29	1.12	1.38
m(g)	9	21	*22.3*	*6.7*	*15.6*
ρ_b (g/cm^3)	-	-	0.32	0.1	0.22
X_i (-)	0.3	0.7		0.3	0.7
ε_g(-)	-		*0.75*	*0.75*	
h_0(cm)	3		*3.5*	*3.5*	

Table A7. Modeling parameters used for poplar wood-coal 40:60 mixture

Properties	Experiments		Sim-S	Sim -B	
	Poplar wood	Coal	Mix. Props.	Poplar wood	Coal
d_p(μm)	153	62	*85*	153	62
ψ(-)	-	-	1	1	1
ρ_s (g/cm^3)	1.12	1.38	1.26	1.12	1.38
m(g)	12	18	*22.3*	*8.9*	*13.4*
ρ_b (g/cm^3)	-	-	0.40	0.16	0.24
X_i (-)	0.4	0.6		0.4	0.6
ε_g(-)	-		*0.68*	*0.68*	
h_0(cm)	3		*2.7*	*2.7*	

Table A8. Modeling parameters used for poplar wood-coal 50:50 mixture

Properties	Experiments		Sim-S	Sim -B	
	Poplar wood	Coal	Mix. Props.	Poplar wood	Coal
d_p(μm)	153	62	*92*	153	62
ψ(-)	-	-	1	1	1
ρ_s (g/cm^3)	1.12	1.38	1.24	1.12	1.38
m(g)	15	15	*16.2*	*8.1*	*8.1*
ρ_b (g/cm^3)	-	-	0.35	0.18	0.18
X_i (-)	0.5	0.5		0.5	0.5
ε_g(-)	-		*0.72*	*0.72*	
h_0(cm)	3		*2.3*	*2.3*	

Table A9. Modeling parameters used for cornstover-coal 20:80 mixture

Properties	Experiments		Sim-S	Sim -B	
	Cornstover	Coal	Mix. Props.	Cornstover	Coal
d_p(μm)	418	62	*76*	418	62
ψ(-)	-	-	1	1.00	1
ρ_s (g/cm^3)	1.21	1.38	1.34	1.21	1.38
m(g)	6	24	*24.3*	*4.9*	*19.5*
ρ_b (g/cm^3)	-	-	0.32	0.06	0.26
X_i (-)	0.2	0.8		0.2	0.8
ε_g(-)	-		*0.76*	*0.76*	
h_0(cm)	3		*3.7*	*3.7*	

Table A10. Modeling parameters used for cornstover-coal 30:70 mixture

Properties	Experiments		Sim-S	Sim -B	
	Cornstover	Coal	Mix. Props.	Cornstover	Coal
d_p(μm)	418	62	*87*	418	62
ψ(-)	-	-	1	1.00	1
ρ_s (g/cm^3)	1.21	1.38	1.32	1.21	1.38
m(g)	9	21	*26.4*	*7.9*	*18.4*
ρ_b (g/cm^3)	-	-	0.37	0.11	0.26
X_i (-)	0.3	0.7		0.3	0.7
ε_g(-)	-		*0.72*	*0.72*	
h_0(cm)	3		*3.5*	*3.5*	

Table A11. Modeling parameters used for cornstover-coal 40:60 mixture

Properties	Experiments		Sim-S	Sim -B	
	Cornstover	Coal	Mix. Props.	Cornstover	Coal
d_p(μm)	418	62	*98*	418	62
ψ(-)	-	-	1	1	1
ρ_s (g/cm^3)	1.21	1.38	1.31	1.21	1.38
m(g)	12	18	*26.4*	*10.5*	*15.8*
ρ_b (g/cm^3)	-	-	0.40	0.16	0.24
X_i (-)	0.4	0.6		0.4	0.6
ε_g(-)	-		*0.70*	*0.70*	
h_0(cm)	3		*3.2*	*3.2*	

Table A12. Modeling parameters used for cornstover-coal 50:50 mixture

Properties	Experiments		Sim-S	Sim -B	
	Cornstover	Coal	Mix. Props.	Cornstover	Coal
d_p(μm)	418	62	*114*	418	62
ψ(-)	-	-	1	1	1
ρ_s (g/cm^3)	1.21	1.38	1.29	1.21	1.38
m(g)	15	15	*24.3*	*12.2*	*12.2*
ρ_b (g/cm^3)	-	-	0.47	0.23	0.23
X_i (-)	0.5	0.5		0.5	0.5
ε_g(-)	-		*0.64*	*0.64*	
h_0(cm)	3		*2.6*	*2.6*	